



Durham E-Theses

V.H.E. Gamma Rays From Microquasars

Latham, Ian James

How to cite:

Latham, Ian James (2006) *V.H.E. Gamma Rays From Microquasars*, Durham theses, Durham University. Available at Durham E-Theses Online: <http://etheses.dur.ac.uk/2946/>

Use policy

The full-text may be used and/or reproduced, and given to third parties in any format or medium, without prior permission or charge, for personal research or study, educational, or not-for-profit purposes provided that:

- a full bibliographic reference is made to the original source
- a [link](#) is made to the metadata record in Durham E-Theses
- the full-text is not changed in any way

The full-text must not be sold in any format or medium without the formal permission of the copyright holders.

Please consult the [full Durham E-Theses policy](#) for further details.

Abstract

This thesis is concerned with the detection of very high energy (VHE) γ -rays from microquasars, a recently discovered subclass of x-ray binaries that display jets of relativistic particles.

A general introduction to ground based γ -ray astronomy is presented, which discusses the production of Cherenkov radiation and how VHE γ -rays are detected via extended air showers in the atmosphere. The important processes involved in the production and absorption of γ -rays are detailed, before the design of The High Energy Stereoscopic System (H.E.S.S.) Phase I telescope array, based in Namibia, is briefly described.

There follows a general section on microquasars, describing x-ray binaries and the morphological analogy between microquasars and active galactic nuclei (AGN). Some important properties of jets are detailed before the spectral states of x-ray binaries and their importance in relation to jets are discussed.

A synchrotron self-Compton (SSC) model designed for AGN is reviewed in some detail and is applied to the blazar 3C 279, showing a good fit to data. This SSC model is then applied to the microquasars GRS 1915+105, V4641 Sgr and GX 339-4 using a scale-invariant method to investigate if the jets from microquasars can be considered simply as scaled down AGN jets. Conclusions are drawn from the results.

Data taken with H.E.S.S. on four microquasars are presented. The techniques used to take and analyse this data are described in some detail using data taken on the Crab nebula as an example of a VHE γ -ray emitter, before the analysis results for observations of GRS 1915+105, Circinus X-1, GX 339-4 and V4641 Sgr are presented.

A novel method for manufacturing aluminium mirrors suitable for use on ground based γ -ray telescopes is described in detail along with the testing techniques used. The next generation telescope, H.E.S.S. Phase II is then described briefly.

The thesis concludes with a brief outline of future work to be conducted, based on the SSC model, as applied to microquasars. A proposal for observations of IGR J19140+0951, which was tentatively detected in the field of GRS 1915+105, is outlined.

V.H.E. Gamma Rays From Microquasars

by

Ian James Latham

The copyright of this thesis rests with the author or the university to which it was submitted. No quotation from it, or information derived from it may be published without the prior written consent of the author or university, and any information derived from it should be acknowledged.



Submitted in conformity with the requirements
for the degree of Doctor of Philosophy

Department of Physics
University of Durham
South Road
Durham. UK.

Copyright © 2006 by Ian James Latham

27 JUL 2006



Contents

1	Introduction	1
1.1	Historical Background	1
1.2	Ground Based γ -Ray Astronomy	2
1.2.1	Cherenkov Radiation	2
1.2.2	Extended Air Showers	4
1.3	Important Radiation Processes	7
1.3.1	Synchrotron Radiation	7
1.3.2	Inverse-Compton Scattering	12
1.3.3	Bremsstrahlung	15
1.3.4	Pion Production	16
1.3.5	Pair Production	17
1.4	Ground Based Cherenkov Astronomy	18
1.5	The High Energy Stereoscopic System - H.E.S.S.	20
1.5.1	Introduction	20
1.5.2	Mount and Dish	20
1.5.3	Mirrors	22
1.5.4	Camera	23
1.6	Microquasars	25
1.6.1	Introduction	25
1.6.2	Active Galactic Nuclei (AGN) Analogy	26
1.6.3	Superluminal Motion	30
1.6.4	Relativistic Doppler Factor	33
1.6.5	Doppler Boosting	34
1.6.6	Spectral States of X-Ray Binaries	34

2	A Synchrotron Self-Compton Model for Microquasars	39
2.1	The Scenario	39
2.1.1	Jet Geometry	40
2.1.2	Parameterisation	41
2.2	Synchrotron Coefficients of Emissivity and Absorption	42
2.2.1	Synchrotron Coefficient of Emissivity	42
2.2.2	Synchrotron Coefficient of Self-Absorption	43
2.3	Maximum Synchrotron Frequency	45
2.4	Synchrotron Self Absorption Frequency	47
2.5	Synchrotron Luminosity	49
2.6	Inverse Compton Luminosity	51
2.6.1	Inverse Compton Frequency Range	53
2.6.2	Inverse Compton Integration Limits	56
2.6.3	Contributing Frequencies to ν_{ic}	60
2.7	Code Test - 3C 279	63
2.8	Application to Microquasars	68
2.8.1	Introduction	68
2.8.2	Scale-Invariant Jets	72
2.8.3	Discussion and Conclusions	77
3	H.E.S.S. Data Analysis	81
3.1	Introduction	81
3.2	Data Selection	82
3.3	H.E.S.S. Analysis Software	85
3.3.1	Introduction	85
3.3.2	Data Taking	85
3.3.3	Gamma-Hadron Separation	86
3.3.4	Background Estimation	89
3.3.5	Flux Measurements and Upper Limits	91
3.3.6	Crab Results	92
3.4	Microquasar Analysis Results	94
3.4.1	GRS 1915+105	94
3.4.2	Circinus X-1	100

3.4.3	GX 339-4	104
3.4.4	V4641Sgr	108
3.5	Results Summary	111
4	Vacuum Formed Aluminium Mirrors	113
4.1	The H.E.S.S. Phase I Telescope Mirrors	113
4.2	Mirror Construction Method	115
4.3	The Mould	116
4.3.1	Fibreglass Resin Moulds	117
4.3.2	Aluminium Moulds	120
4.4	Miro 4270 - The Reflective Surface	123
4.5	Mirror Testing	124
4.6	Summary	128
5	Conclusions and Future Work	130
5.1	Synchrotron Self-Compton Model	130
5.2	LS5039 - First Microquasar detected at VHE Energies?	131
5.3	Further Observations	134
5.3.1	IGR J19140+0951	134
5.3.2	Microquasars	135
5.4	H.E.S.S. Phase II	135
5.4.1	Introduction	135
5.4.2	The H.E.S.S. Phase II Design	136
A	Synchrotron Self-Compton Code	138
A.1	Synchrotron Self-Compton Code	138
B	Definition of Hillas Parameters	171
B.1	Definition of Hillas Parameters	171

Declaration

The material contained within this thesis has not previously been submitted for a degree at the Durham University or any other university. The research reported within this thesis has been conducted by the author unless indicated otherwise.

Copyright Notice

The copyright of this thesis rests with the author. No quotation from it should be published without their prior written consent and information derived from it should be acknowledged.

Dedication

To my wife Gloria, and children Megan and James, without whose unconditional love and support this would not have been possible.

Acknowledgements

There are many people I wish to acknowledge:

First and foremost my supervisor Dr. P.M. Chadwick who has given me her utmost support and understanding during my Ph.D.

Dr. Joy McKenny who has been a close associate and friend while we have worked on improving the mirrors.

I would also like to thank the other members of the γ -ray astronomy group, some of who have since left, but nevertheless provided friendship, guidance and help. In particular I would like to thank;

Aris Noutsos who has been studying for his Ph.D. at the same time and with whom I have had many intellectual, but friendly arguments, and of course the occasional non-intellectual, yet still stimulating conversation.

Dr. Sam Nolan whose expert knowledge of analysis has helped a great deal in producing this work.

Hugh Dickinson whose programming expertise has helped with the mirror testing software and has provided many intellectual conversations about micro-quasars.

Anthony Brown, our resident Aussie, for graciously losing the Ashes and the Rugby World Cup and still remaining a good friend.

Christos Hadjichristidis, who accompanied me on a working trip to Namibia.

Finally I would like to thank PPARC, the University of Durham and Ustinov College for their financial support during this time.

Chapter 1

Introduction

1.1 Historical Background

The birth of γ -ray astronomy began in the early 20th century with balloon experiments designed to find the source of radiation that was interfering with electrical experiments of the day. One such experiment, conducted by Victor Hess (1911), showed that the Earth was being bombarded with high energy radiation, the level of which increased with the altitude of the balloon. This experiment demonstrated that the radiation, later dubbed ‘Cosmic Radiation’, was of an extraterrestrial origin. We now know from high altitude balloon experiments and satellites that the majority of these cosmic rays are subatomic particles, around 90% being protons, 9% alpha-particles and the remainder being heavier nuclei. A small minority of cosmic rays are γ -rays, high energy electromagnetic radiation ranging from around 100 keV up to >20 Tev.

One of the major conundrums surrounding cosmic rays is their origin. Cosmic rays are isotropic; the majority of them are charged particles and so information about their place of origin is lost as they are deflected by the magnetic fields that exist in the galaxy. γ -rays, however, have no charge and their path remains unchanged, allowing us to observe the direction from which they were emitted. Since γ -rays are likely to be produced in the same extreme environments as the majority of cosmic rays, they give us the opportunity to probe these high energy environments; a 100 GeV γ -ray, for example, can only be



produced by particle acceleration, since no known object exists at a sufficiently high temperature to produce them thermally.

γ -rays in the 10 keV - 30 MeV energy regime, low-medium energy γ -rays, and from 30 MeV - 100 GeV, high-energy γ -rays, are observed using space borne satellite detectors such as EGRET and INTEGRAL. Very high energy (VHE) γ -rays, from 100 GeV - 100 TeV and ultra high energy (UHE) γ -rays, >100 TeV, have fluxes that are too low to be detectable by satellites. This is the domain of ground based γ -ray astronomy and, more relevant to this thesis, the Imaging Atmospheric Cherenkov Technique (IACT), discussed in the next section.

1.2 Ground Based γ -Ray Astronomy

1.2.1 Cherenkov Radiation

Cherenkov radiation was first discovered in the early 1900's by Marie and Pierre Curie and later noted by Mallet in 1926, who, although he could produce the emission, could not find the nature of it. Experimental work carried out by P.A. Cherenkov between 1934 - 1937, together with its theoretical interpretation by I.E. Tamm and I.M. Frank in 1937, first described the radiation. When a charged particle travels through a dielectric medium, such as the atmosphere, it disturbs the neutrality of the adjacent molecules inducing a polarisation as it travels. If the particle is moving at a velocity that is less than the speed of light in that medium then the polarisation is symmetric both radially and in the direction of the particle's trajectory, as is shown in the left hand diagram of Fig.(1.1). The overall electromagnetic field is thus zero and there is no detectable radiation. If, however, the particle is travelling faster than the speed of light in that medium, $v_{particle} > \frac{c}{n(\lambda)}$, where $n(\lambda)$ is the refractive index of the medium, then although radial symmetry is maintained, there is a net dipole effect in the direction of the particle's trajectory, as is shown in the right hand diagram of Fig.(1.1). The result of this is the emission of Cherenkov radiation. This radiation is only observed at a certain angle, θ , called the Cherenkov angle. Fig.(1.2) shows the Huygens construction to demonstrate

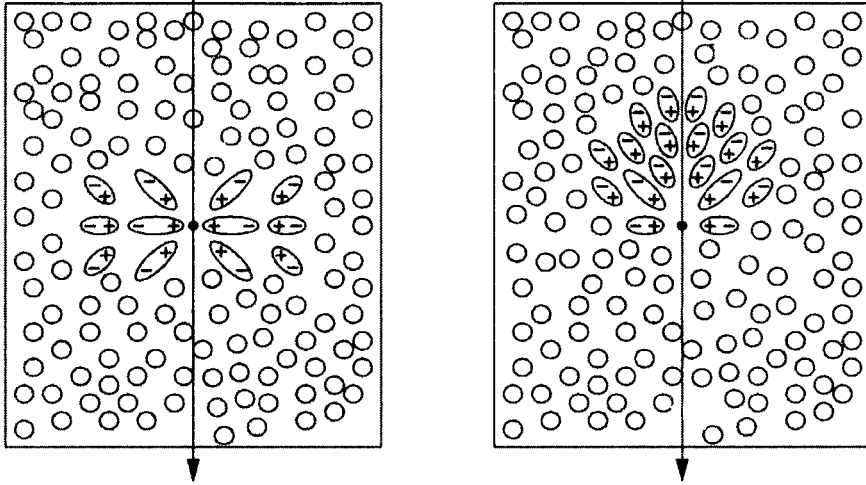


Figure 1.1: The local polarisation of the medium produced by a fast moving charged particle travelling through a dielectric medium with $v < \frac{c}{n}$ (left) and with $v > \frac{c}{n}$ (right)

this. A particle is considered to move from A-B during time δt with velocity $v_{particle}$. Wavelets are emitted at the Cherenkov angle from arbitrary points P_i along the path to form a coherent plane wavefront. During time δt the wavelet emitted from A at time $t = 0$ has travelled with velocity $\frac{c}{n(\lambda)}$ to C. The Cherenkov angle, θ is then given by,

$$\cos \theta = \frac{\frac{c}{n(\lambda)} \delta t}{v_{particle} \delta t} = \frac{1}{\beta n(\lambda)} \quad (1.1)$$

where

$$\beta = \frac{v_{particle}}{c} \quad (1.2)$$

This leads to the following conclusions:

- From Eq.(1.1) it can be seen that for a given medium of refractive index $n(\lambda)$, there is a threshold velocity, given by $\beta_{min} = \frac{1}{n(\lambda)}$, below which there is no Cherenkov emission.
- It can also be seen that for an ultra-relativistic particle where $\beta \sim 1$ there is a maximum angle of emission given by, $\cos \theta_{max} = \frac{1}{n}$

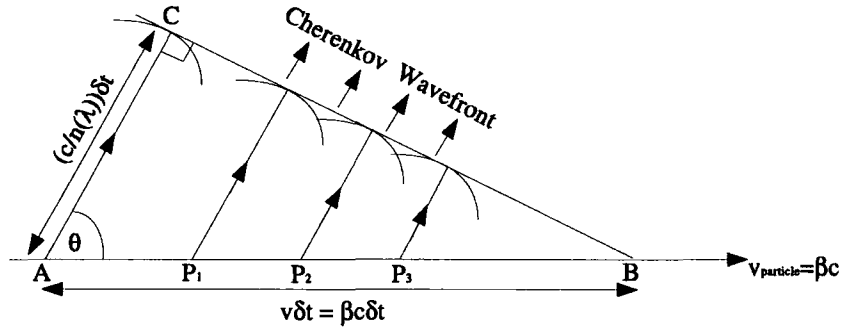


Figure 1.2: Huygens construction to illustrate the Cherenkov angle, θ . A charged particle moving through a medium with refractive index $n > 1$, from A-B in time δt with $v_{particle} > \frac{c}{n}$, emits individual wavefronts along its path, represented by the points P_i . Constructive interference leads to Cherenkov radiation over the surface of a cone with half angle θ .

- Additionally, Cherenkov emission can only occur where $\frac{c}{n(\lambda)} < c$. For typical media such as the atmosphere, $n(\lambda) > 1$ only for longer wavelength photons up to ultra-violet, hence Cherenkov emission in x-rays and γ -rays does not occur.

The original analysis of an electron moving in a dielectric medium was first conducted by Frank and Tamm [34] who showed that the number of photons, N , produced between wavelengths λ_1 and λ_2 by an electron moving along a length l is given by,

$$N = 2\pi l \left(\frac{1}{\lambda_1} - \frac{1}{\lambda_2} \right) \sin^2 \theta \quad (1.3)$$

This means that the peak of the Cherenkov radiation is produced in the ultra-violet range around 330nm (see Fig.(4.7)) as $\frac{dN^2}{d\lambda} \propto \frac{1}{\lambda^2}$.

1.2.2 Extended Air Showers

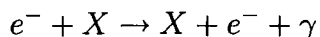
The Cherenkov light observed by γ -ray astronomers is produced when a γ -ray enters our atmosphere initiating a cascade of electron-positron pairs, which share the energy of the primary γ -ray and move in the same forward direction.

It is these sub-atomic particles, moving faster than the speed of light in air, that produce the ~ 10 ns Cherenkov flashes which are observed. After these particles have travelled one radiation length, more lower energy photons are produced via Bremsstrahlung; these, in turn, pair produce. This continues until the photons reach ionisation energies, around 84 MeV, at which point Cherenkov radiation stops. This cascade of electron-positron pairs and photons is known as an Extended Air Shower (EAS). The Cherenkov radiation emitted during the EAS reaches the ground in a pool of light that can cover around 10^5m^2 . The pool of light shows higher intensity at the outer edges, the ‘Cherenkov ring’, due to the Cherenkov angle broadening as the particles lose velocity. The problem for γ -ray astronomers is that cosmic rays also produce EAS’s in much greater numbers. Fortunately there is a significant difference in the way the EAS propagates, which allows discrimination.

Fig.(1.3) shows the development of an EAS initiated by a γ -ray. The first interaction is pair production in the vicinity of a nucleus, X ,



The electron and positron then emit further high energy photons via Bremsstrahlung,



These high energy photons in turn pair produce, and the shower continues in this way until the energies of the photons are too low to pair produce and the energies of the electrons/positrons reach ionisation levels, which then becomes the dominant process. This point is known as shower maximum, as the greatest amount of Cherenkov light is produced here. The γ -ray initiated EAS is a very well ordered development, as there are only two main processes and the overall direction of the propagation is that of the primary γ -ray. An EAS initiated by a proton or cosmic ray is far less ordered and more complex, containing many different processes.

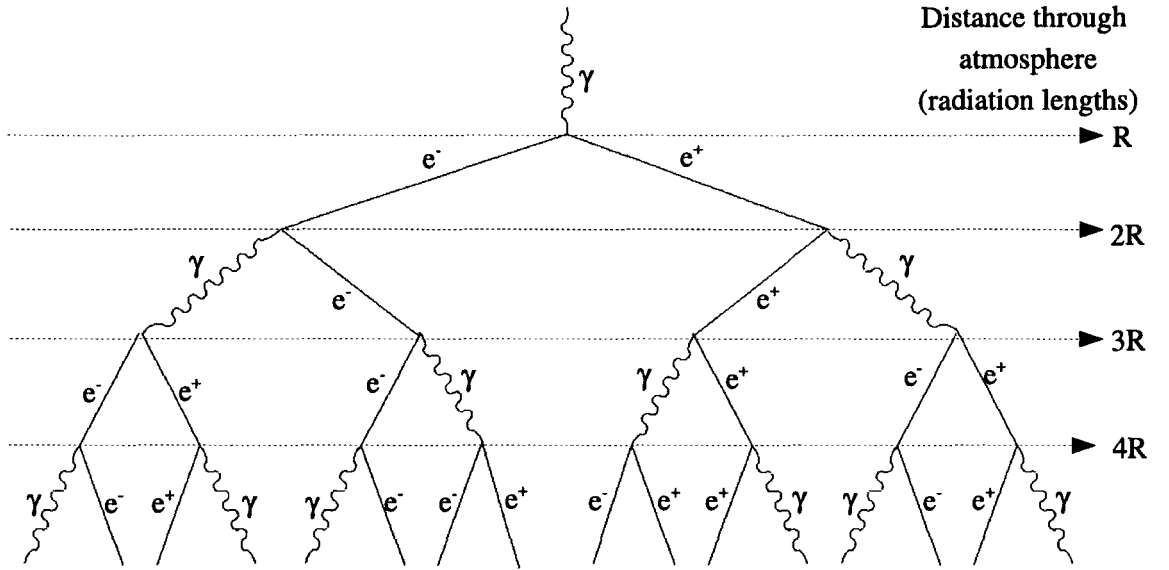


Figure 1.3: Representation of a γ -ray EAS as it progresses through the atmosphere. The transverse angles are exaggerated for clarity, the initial pair production having a direction along the trajectory of the primary γ -ray.

Fig.(1.4) shows the development of an EAS initiated by a proton. The initial interaction with an atmospheric nuclei produces pion triplets with large transverse momentum, and high energy nucleons, for example,

$$p + p \rightarrow \begin{cases} p + n + \pi^+ \\ p + p + \pi^0 \end{cases} \quad \text{and} \quad n + p \rightarrow \begin{cases} n + n + \pi^+ \\ n + p + \pi^0 \\ p + p + \pi^- \end{cases}$$

The pion triplets then decay through such processes as,

$$\begin{aligned} \pi^0 &\rightarrow \gamma + \gamma \\ \pi^+ &\rightarrow \mu^+ + \nu_\mu \\ \pi^- &\rightarrow \mu^- + \bar{\nu}_\mu \end{aligned}$$

The secondary γ -rays and associated electron-positron pairs that are the result of the π^0 quickly attenuate due to ionisation. Lower energy μ^\pm produced in the decay of the charged pions decay to electrons, positrons and neutrinos. Higher

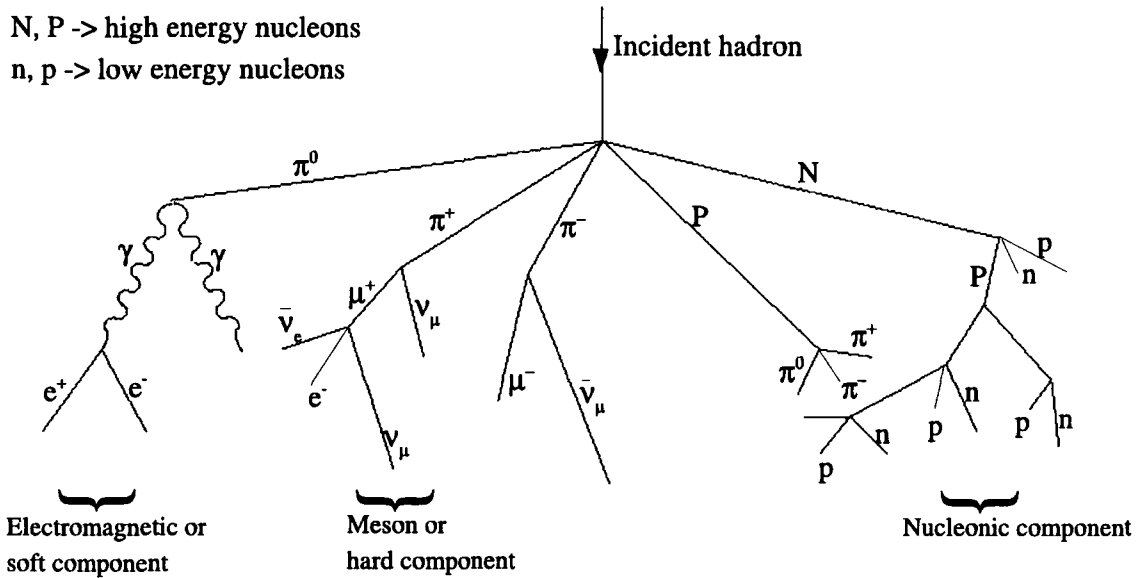


Figure 1.4: Representation of a hadronic initiated EAS as it progresses through the atmosphere. Note the more disordered development and in this case and the larger transverse angles, which are passed through the developing shower.

energy muons may penetrate to ground level producing muon rings in the detector and are a major difference between γ -ray induced EAS and hadronic induced EAS.

Fig.(1.5) shows the Monte Carlo EAS simulation of a 320 GeV γ -ray alongside that of a proton of 1TeV to demonstrate the difference between the two. When the image of the EAS is detected in the camera, the shape of the Cherenkov flash image is parameterised using Hillas parameters [56][29], which are used to discriminate between an hadronic EAS and a γ -ray EAS. The Hillas parameters are covered in detail in Section 3.3.3 and Appendix B.

1.3 Important Radiation Processes

1.3.1 Synchrotron Radiation

Although synchrotron radiation does not produce γ -rays directly, it is nevertheless a very important process. The very existence of synchrotron radiation

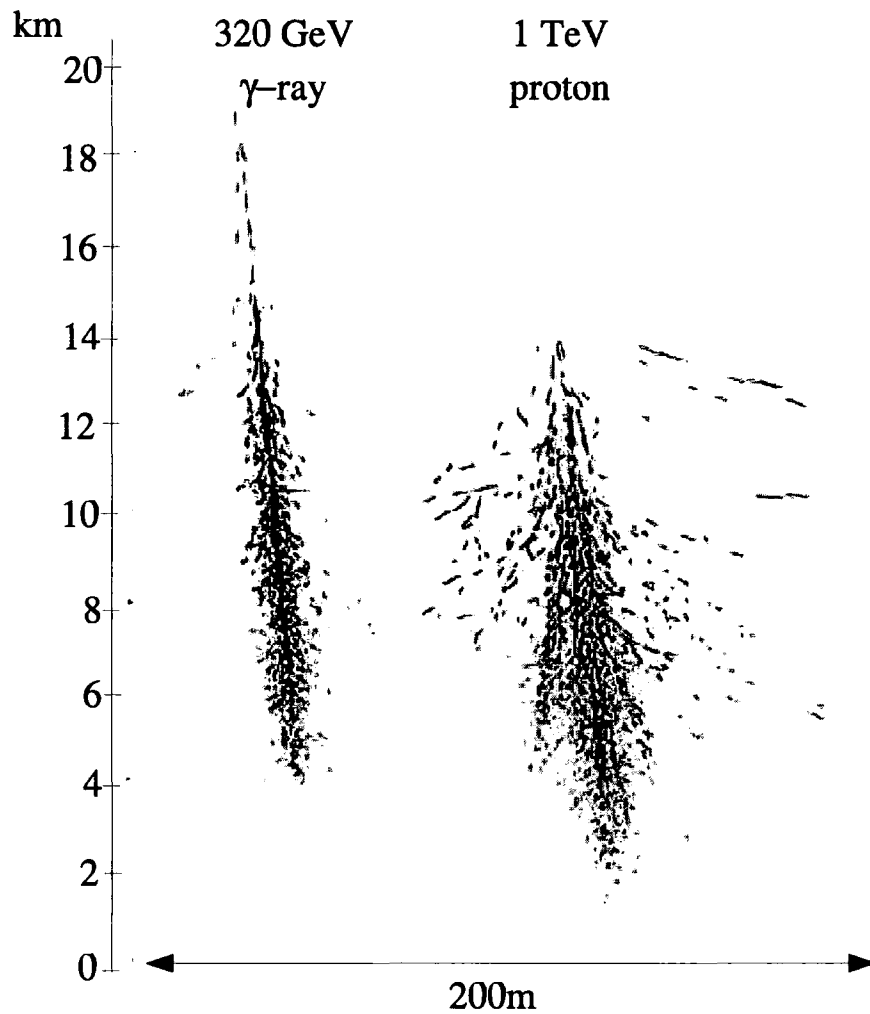


Figure 1.5: Monte Carlo EAS simulations of a 320 GeV γ -ray and a 1 TeV proton. The tracks show the development of the shower through the atmosphere clearly showing the broader, more disordered EAS produced by the proton (adapted from [109])

means that highly relativistic particles are present. Synchrotron radiation is produced by a charged particle spiralling around a magnetic field and was first detected in early particle accelerators, hence its name. When a non-relativistic particle of charge q and rest mass m_0 moves with velocity v through a magnetic field of strength B , the Lorentz force causes it to spiral around the field lines, its circular path of radius R_g , being described by,

$$\frac{Bqv}{c} = \frac{\gamma m_0 v^2}{R_g} \quad (1.4)$$

where γ is the Lorentz factor given by $(1 - v^2/c^2)^{-1/2}$, which leads to an angular velocity of

$$\omega_L = \frac{v}{R_g} = \frac{Bq}{\gamma m_0 c} \quad (1.5)$$

and the radiation, *cyclotron radiation*, is emitted at a frequency $\nu = \frac{\omega_L}{2\pi}$, often

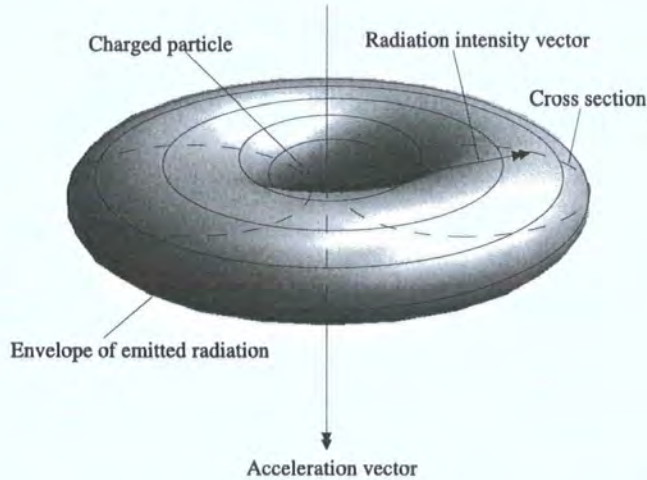


Figure 1.6: Dipole radiation by an accelerated particle (adapted from [64])

called the Larmor frequency, with a dipole pattern around its acceleration vector, Fig.(1.6). The intensity at an angle θ is given by [64],

$$I(\theta) = \frac{q^2}{16\pi^2 c^3 \epsilon_0} a^2 \sin^2 \theta \quad (1.6)$$

where a is the acceleration of the particle and ϵ_0 is the permittivity of free space. When the charged particle is relativistic, the radiation is beamed into a cone directed along the velocity vector of the particle, as in Fig.(1.7), which has a half angle θ given by,

$$\theta = \frac{1}{\gamma} \quad (1.7)$$

and the observer will see it for time Δt_2 where,

$$\Delta t_2 = \frac{2\theta}{2\pi} \cdot 2\pi\Delta t_L \quad (1.8)$$

where $\Delta t_L = \frac{1}{\omega_L}$.

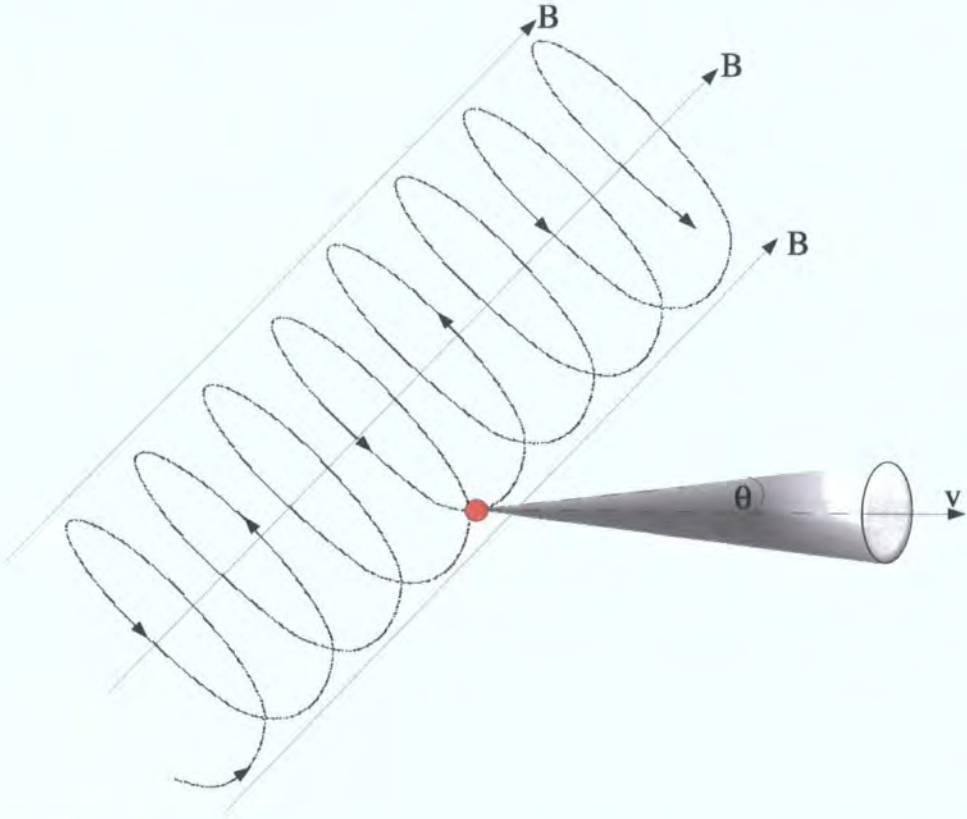


Figure 1.7: Synchrotron radiation emitted from a relativistic charged particle in a magnetic field B . The radiation due to the particle spiralling around the magnetic field lines, B , is beamed into a cone directed along the velocity vector of the particle with a half angle $\theta = \frac{1}{\gamma}$

Substituting for Δt_L using equation Eq.(1.5) and θ using equation Eq.(1.7) then,

$$\Delta t_2 = \frac{2m_0c}{Bq} \quad (1.9)$$

If the particle emits a photon and then travels a distance l during time Δt_2 , the difference between the arrival times of the photons gives the maximum synchrotron frequency that can be emitted. Consider the time delay Δt_0 between the arrival times of the photons,

$$\Delta t_0 = \left(\frac{l}{v} - \frac{l}{c} \right) \quad (1.10)$$

Since $l \sim v\Delta t_2$ then,

$$\Delta t_0 = \left(1 - \frac{v}{c} \right) \Delta t_2 \quad (1.11)$$

Using the approximation,

$$(1 - x) \sim \frac{1}{2}(1 - x^2) \quad \text{for } x \sim 1 \quad (1.12)$$

then

$$\Delta t_0 = \frac{1}{2} \left(1 - \frac{v^2}{c^2} \right) \Delta t_2 = \frac{\Delta t_2}{2\gamma^2} \quad (1.13)$$

Using equation Eq.(1.9) it can be shown that,

$$\Delta t_0 \propto \frac{1}{\gamma^2 B} \quad (1.14)$$

and hence the maximum synchrotron frequency, ν_{max}^s that can be emitted by a distribution of electrons with $\gamma_{min} \leq \gamma \leq \gamma_{max}$ in a magnetic field B follows the relation,

$$\nu_{max}^s \propto \gamma_{max}^2 B \quad (1.15)$$

This is an important relation in the synchrotron self Compton model described in Chapter 2.

1.3.2 Inverse-Compton Scattering

When a photon is scattered by an electron, which is at rest, momentum and energy are exchanged, as shown in Fig.(1.8). The electron, of rest mass m_e , gains energy as it acquires a recoil momentum, the photon losing energy as it scatters. This process is known as Compton scattering. The energy of the

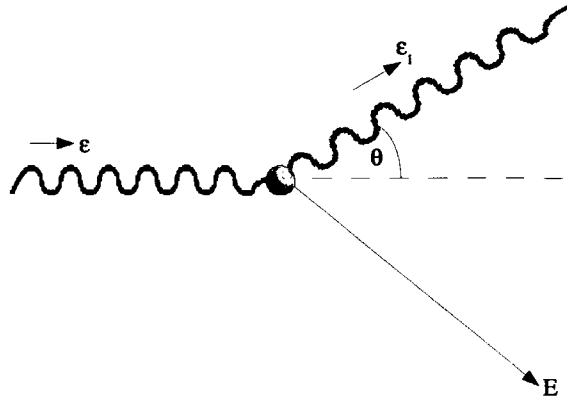


Figure 1.8: Compton scattering. An incident photon of energy ϵ is scattered by an electron at rest at an angle θ with energy ϵ_1 . For $\epsilon \ll m_e c^2$ then $\epsilon_1 \approx \epsilon$.

scattered photon, ϵ_1 , at an angle θ to the path of the incident photon, ϵ , can be described by the equation [63],

$$\epsilon_1 = \frac{\epsilon}{1 + \frac{\epsilon}{m_e c^2} (1 - \cos \theta)} \quad (1.16)$$

If the photon is a low energy photon, $\epsilon \ll m_e c^2$, the energy transferred to the electron is negligible and the photon is scattered an angle θ to its original path with $\epsilon_1 \approx \epsilon$, which is described by Thomson scattering. A higher energy photon will be scattered to a lower energy, the electron recoiling and acquiring the energy difference.

The total cross-section for Compton scattering is given by the Klein-Nishina formula:

$$\sigma_{KN} = \frac{3\sigma_T}{4} \left\{ \frac{1+x}{x^3} \left[\frac{2x(1+x)}{1+2x} - \ln(1+2x) \right] + \frac{\ln(1+2x)}{2x} - \frac{1+3x}{(1+2x)^2} \right\} \quad (1.17)$$

with $x = \frac{E}{m_e c^2}$ and $\sigma_T = \text{Thomson cross-section}$

If the cross-section (normalised to the Thomson cross-section) is plotted against photon energy, Fig.(1.9), it can be seen that at low photon energies $\sigma_{KN} \sim \sigma_T$ and the scattered photon energy will be similar to the incident photon energy - not useful for VHE emission. However, this is where relativity becomes

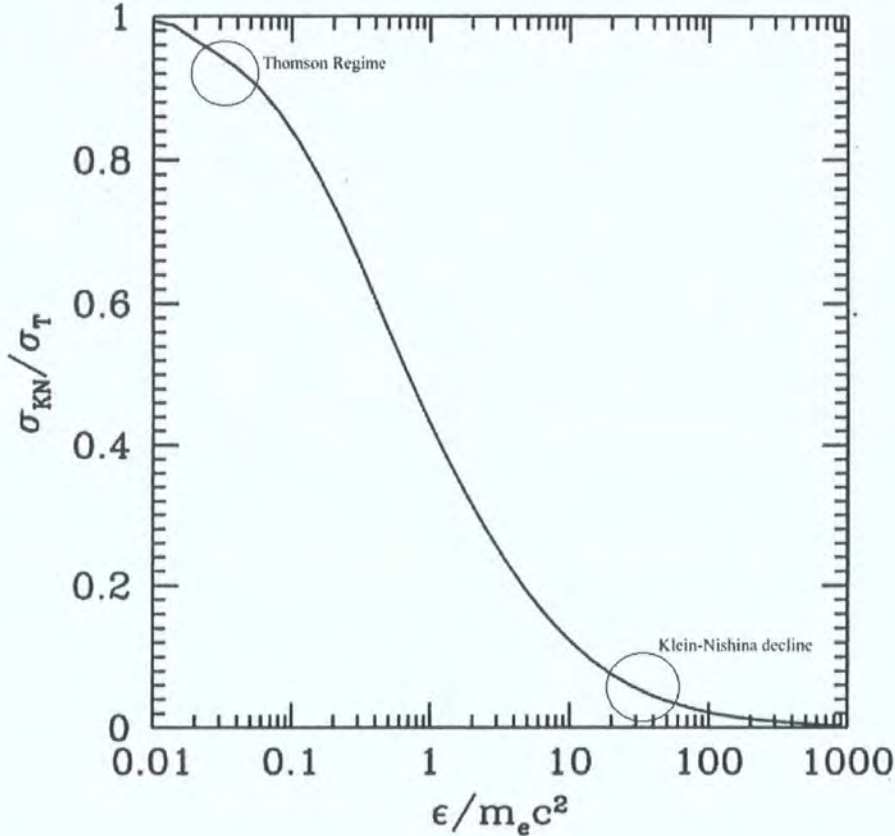


Figure 1.9: The variation of Compton scattering cross-section with photon energy.

important. The above description is true for an electron at rest, not in the observer's frame of reference, but in the rest frame of the electron. It is common for Compton scattering to be described where the observer's frame of reference and the electron's frame of reference coincide. In the jets of microquasars there are electrons moving at relativistic speeds ($> 0.1c$); indeed the fastest jets approach $\sim 0.98c$. In this case, where the electron and photon are both

moving in the observer's frame of reference, energy can pass either way and the photon can be up-scattered to a higher energy. This is called inverse-Compton scattering and is an important process for the production of VHE γ -rays. The energy of a photon, ϵ' , in the rest frame of a relativistic electron, is given by,

$$\epsilon' = \gamma\epsilon(1 - \beta \cos \theta) \quad (1.18)$$

(where ϵ is the energy of the photon in the observer's frame) which means for all but small angles $\epsilon' \sim \gamma\epsilon$. Two scenarios can now be considered.

If $\epsilon' = \gamma\epsilon \ll m_e c^2$ then the scattering is in the Thomson regime and $\epsilon \rightarrow \gamma^2\epsilon$ after inverse Lorentz transformation back to the observer's frame. The photon is upscattered with its energy increased by a factor of γ^2 , which can be very high for highly relativistic electrons. Provided the electrons are of high enough energy and there is a high density, low energy photon field, a large cross section for VHE radiation is possible. Also in this scenario the energy imparted to the photon by the electron is small compared to its relativistic energy, since the original condition that $\epsilon \ll \frac{m_e c^2}{\gamma}$ means that $\frac{\gamma^2\epsilon}{\gamma m_e c^2} \ll 1$. Thus the electron can undergo this process several times. Since the total energy must also be conserved the increase in the photon's energy is limited to $\gamma m_e c^2$.

If $\epsilon' = \gamma\epsilon \gg m_e c^2$ then Thomson scattering no longer applies and the scattering cross-section falls into the Klein-Nishina (K-N) regime. In the electron's rest frame the photon has high energy with $\gamma\epsilon \gg m_e c^2$ for the extreme K-N regime, and thus it loses energy to the electron in that frame. From equation Eq.(1.16) the scattered photon has an energy comparable to $m_e c^2$. In addition, the increase in photon energy is comparable to $\gamma m_e c^2$, so the electron is imparting a large fraction of its relativistic energy to the photon and can undergo the process only once.

The two important types of scattering involving electrons that follow this criteria are

- Synchrotron self-Compton (SSC) and

- External inverse Compton scattering (EIC)

both of which need highly relativistic electrons interacting with a low energy photon field to produce VHE γ -rays. In the case of SSC, the focus of this work, the unscattered photons are produced by the same distribution of electrons that up-scatters them to higher energies. These photons are produced through the synchrotron process, discussed previously, due to the electrons spiralling in the surrounding magnetic field. Conversely, with EIC, the seed field of low energy photons is externally produced. In the case of AGN these may be radiated from surrounding warm dust clouds whereas in microquasars, since the compact object is close to a star, these may be a combination of accretion disk emission and stellar radiation.

1.3.3 Bremsstrahlung

When a charged particle passes close to the electric field of a nucleus it emits radiation called Bremsstrahlung (German for ‘braking’ radiation), Fig.(1.10). The amplitude of the radiation is proportional to the acceleration produced

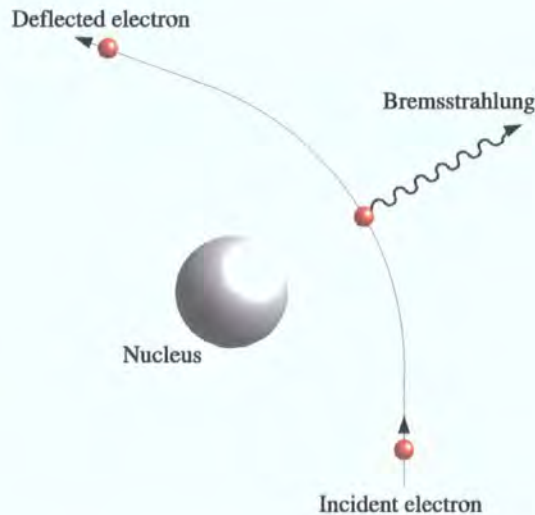


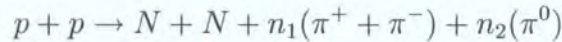
Figure 1.10: Bremsstrahlung produced by the interaction of an electron with the electric field of a nucleus.

by the electric field. This is a particularly important process in astrophysical

cases where there is a large population of relativistic electrons in a region of dense atomic or molecular material as can be found, for example, in supernova remnants. The γ -rays that are emitted have energies of approximately the same order as the incident electrons and if the distribution of electrons is described, for example, by a power law, the Bremsstrahlung spectrum will have a similar characteristic. A complete discussion of Bremsstrahlung from both non-relativistic and relativistic particles can be found in, for example, [71].

1.3.4 Pion Production

γ -rays are also produced in regions of hydrogen gas where there is a population of highly energetic protons, as shown in Fig.(1.11), the threshold energy of the incident proton being 290 MeV [109]. The proton interacts with the hydrogen molecules, the most common interaction being,



where N is either a proton or a neutron and n_1 and n_2 are integers. The π^0 decays to two γ -rays with a half life of 10^{-16} s, which in the rest frame of the pion have energies ~ 70 MeV. This is a useful indication that protons are the

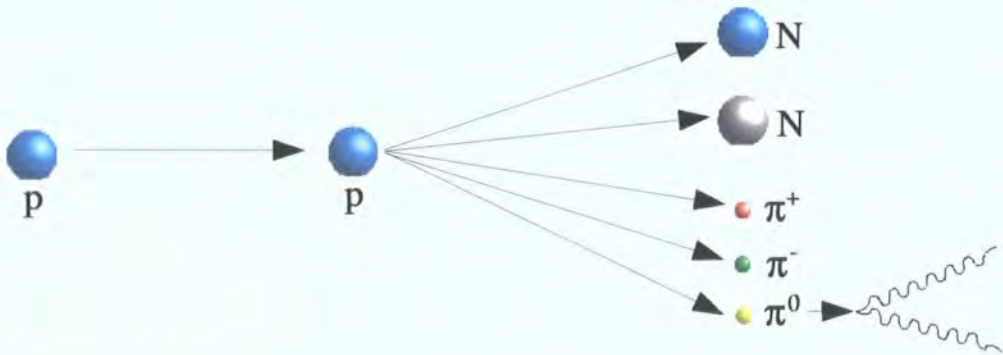


Figure 1.11: Proton-proton interaction producing nucleons (N) and pi mesons. The π^0 decaying to two γ -rays with energy ~ 70 MeV

progenitors of γ -rays in a source, as the γ -ray spectrum will turn over with a

peak at this characteristic energy of 70 MeV. In addition, the spectrum can also indicate if the distribution of protons is thermal or non-thermal [75]. In the case of a thermal distribution of protons there is the characteristic 70 MeV peak with very little low or high energy emission. In the case of non-thermal protons with a power law distribution, Γ_p , there will also be emission at higher energies with an asymptotic spectral slope $\Gamma_\gamma = \Gamma_p$ [28].

1.3.5 Pair Production

Although γ -rays are in general highly penetrating, there are instances where absorption occurs.

- The first of these processes is pair production on matter, Fig.(1.12). As already discussed this interaction is the basis of the imaging technique used to detect γ -rays and also for high energy detectors in satellites. In general the density of matter in interstellar and intergalactic space is too low for absorption of γ -rays to be an important factor. However, close to sources that are surrounded by a high density matter field this is an important factor that should be taken into account.

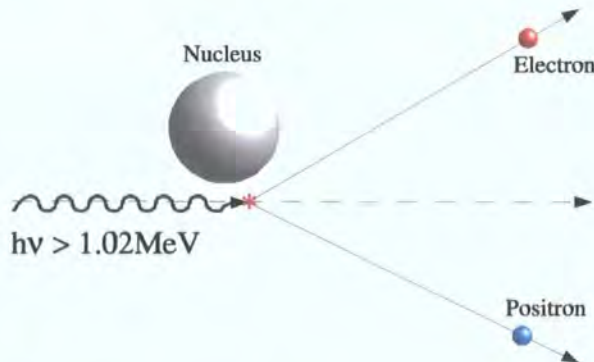


Figure 1.12: Electron-positron pair production through the interaction of a high energy γ -ray ($> 1.02 MeV$) with matter

- The second process is photon-photon pair production. This occurs where a high energy γ -ray interacts with a lower energy photon, producing an electron positron pair. In general this requires a high density, low energy

photon field combined with the high energy γ -rays. The cross section for this process peaks where [109] [71],

$$E_\gamma h\nu(1 - \cos \theta) \sim 2(m_e c^2)^2 = 0.52 \text{MeV}^2 \quad (1.19)$$

where E_γ is the γ -ray energy, $h\nu$ is the energy of the low energy photon and θ is the angle of collision. For head on collisions this occurs for $E_\gamma = 100 \text{ MeV}$ and $h\nu = 5 \text{ keV}$. Interstellar densities of 5 keV x-rays, are too low for this process to significantly absorb 100 MeV γ -rays. However, for a VHE 1 TeV photon, the cross section for head on collisions peaks for low energy photons in the infrared, energies around 0.5 eV, so this effect may no longer be negligible, particularly for distant sources such as AGN.

1.4 Ground Based Cherenkov Astronomy

In 1948, Blackett suggested that Cherenkov emission from muons would be produced in the atmosphere and contribute to the night sky background light. Subsequently in 1953, W. Galbraith and J.V. Jelley [37] detected pulses of radiation from the night sky using the early precursor to modern day Cherenkov telescopes, which consisted of a parabolic reflector and a single PMT. In 1957 P. Morrison published what is considered a seminal paper [86] on γ -ray astronomy. This laid the foundation for a new branch of high energy astronomy.

The first generation of ground based Cherenkov telescopes started with an array of 12 small detectors situated in the Crimea by a group from the Lebedev Institute. Between 1960-1964 they conducted extensive observations of sources suggested by Cocconi, a high energy theorist at CERN. No detections were made by the group. Many other ground based experiments followed, including the Whipple telescope, a 10m optical reflector specifically built for γ -ray astronomy, which, after many modifications and upgrades, is still in use today. In 1985 the Durham group reported the detection of TeV γ -rays from Cygnus X-3 [23] from data collected using Cherenkov telescopes based in Dugway, U.S.A., a claim also substantiated by other groups, see for example [21]

[107].

The upsurge in activity in the field following this led to the subsequent development of the imaging atmospheric Cherenkov technique, a more rigorous γ /hadron discrimination technique, and more sensitive apparatus with lower energy thresholds. In 1989 the Whipple telescope reported the first significant detection of the Crab nebula at TeV energies [108]. One of the challenges now facing γ -ray astronomers, and one of the incentives for new bigger experiments, was to reduce the energy threshold of the ground based experiments in order to close the energy gap to the $\sim 10\text{GeV}$ γ -rays, detectable by satellite-based experiments such as EGRET. This resulted in a new generation of ground based experiments.

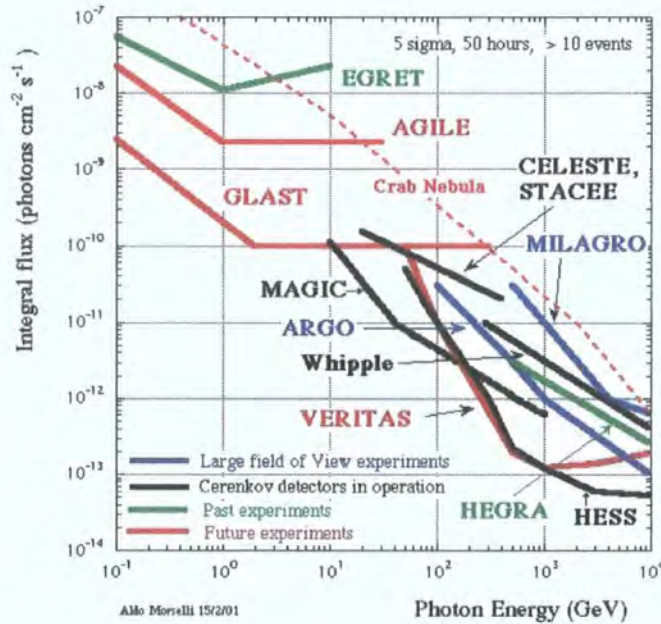


Figure 1.13: Energy flux sensitivities of the various satellite and ground based γ -ray astronomy experiments (image courtesy of A. Morselli [85]).

CANGAROO (1994), an Australia-Japan collaboration located in Woomera Australia, a single 7m dish, which has now been upgraded to 10m and increased to an array of 4 telescopes [66].

MAGIC, a 17m single dish located at La Palma. The mirror surface is $\sim 230\text{m}^2$, reflecting Cherenkov light onto a 577 pixel camera. The target

for this telescope is an energy threshold of only 30 GeV. One of the major benefits of this telescope is its low weight, allowing it to respond quickly to gamma-ray burst alerts [9].

VERITAS will be an array of four 12m telescopes, the first of which saw first light in February 2005 [110].

H.E.S.S., the High Energy Stereoscopic System, is one of the most successful new γ -ray experiments. Phase I of the experiment, which saw first light in December 2003, consists of four Cherenkov telescopes, designed for the investigation of cosmic γ -rays in the 100 GeV range [14]. The data analysed in Chapter 3 were taken using this experiment, hence H.E.S.S. is discussed in more detail in the next section.

1.5 The High Energy Stereoscopic System - H.E.S.S.

1.5.1 Introduction

The H.E.S.S. imaging atmospheric Cherenkov telescope (IACT) array is situated in the Khomas highlands of Namibia, latitude $23^{\circ}16'18''$ south and longitude $16^{\circ}30'00''$ east, at an altitude of 1.8 km [53]. Currently at the completed phase I stage, H.E.S.S. consists of four 13m diameter (flat to flat) telescopes, as shown in Fig.(1.14) placed in a square formation with side length 120m, a distance optimised for maximum sensitivity at a 100 GeV energy threshold.

1.5.2 Mount and Dish

Each telescope consists of a steel construction designed for high mechanical rigidity. The altitude and azimuth are driven by friction drives, which are capable of tracking an object from 0.0° to 89.9° zenith angle and achieve a slew rate of 100° per minute around a 15m auxiliary rail. Both axes have a positional resolution of around $4''$. The dish, hexagonal in shape, is based on the Davies-Cotton design [27] and contains 382 individual, circular mirrors of 600mm diameter. The Davies-Cotton design, a large spherical dish covered in

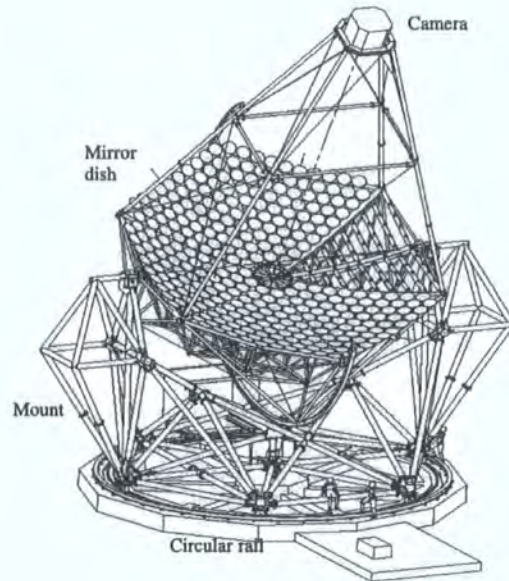


Figure 1.14: H.E.S.S. Phase I Telescope (courtesy of the H.E.S.S. Collaboration).

smaller mirror segments that have the same focal length of the telescope as a whole [15], incorporates the advantages of both a large single spherical mirror and a parabolic mirror, while being neither. A large single spherical mirror has extremely good off axis performance; unfortunately this is spoilt by the fact that light rays reflected towards the focus from the edge of the mirror have to travel a different distance to those reflected from the centre. This means that measuring the arrival time of an event is difficult as it becomes smeared. Since the events are typically only a few nanoseconds in duration, this is a problem. The parabolic dish addresses this problem very well since all the light rays reflected from all points on the mirror have to travel the same distance to the focus, providing excellent timing performance. However, unlike a spherical mirror, the off axis performance is very poor and the field of view is severely limited. The Davies-Cotton design combines the excellent off-axis performance of the spherical mirror with the excellent timing properties of the parabolic dish. Whilst excelling at neither, the compromise provided by this design makes it the most obvious choice for this field. A full description of the

optical components can be found in [15]

1.5.3 Mirrors

Each telescope dish contains 382 individual 600mm diameter circular mirrors that are made from low expansion glass, which is ground to a spherical profile, aluminised and then quartz coated for protection. They have a focal length of

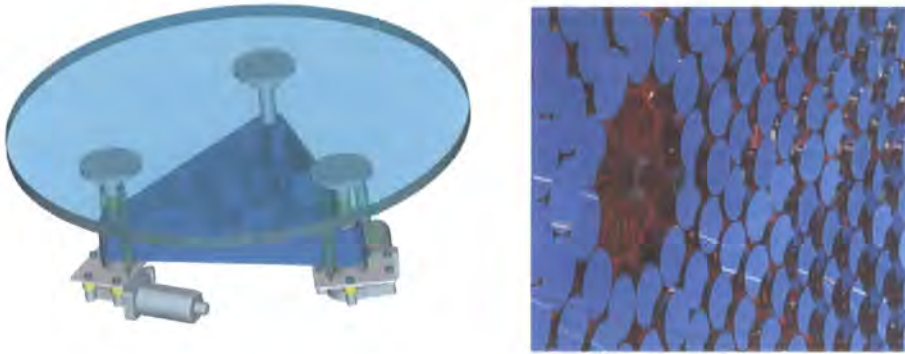


Figure 1.15: Schematic of a H.E.S.S. phase I telescope mirror showing the alignment motors attached at the rear surface (courtesy of the H.E.S.S. Collaboration).

$15 \pm 0.25\text{m}$, reflectivity in the 80-90% range and in total cover an area of 107 m^2 . To ensure that the mirrors are aligned with each other and to provide an easy means of adjustment, each individual mirror is mounted to the dish via two alignment motors that are attached to the rear surface of the mirror, Fig.(1.15). The mirrors are remotely aligned using a bright star imaged on the lid of the camera [26], the pointing being guided by a CCD mounted off-axis in the dish. A second CCD mounted at the centre of the dish views the image and the individual images from each mirror are aligned, using the motors to form one image, the spot of which is contained within a single photomultiplier tube, Fig(1.16). Full details of mirror alignment and point spread functions of the telescopes can be found in [26].

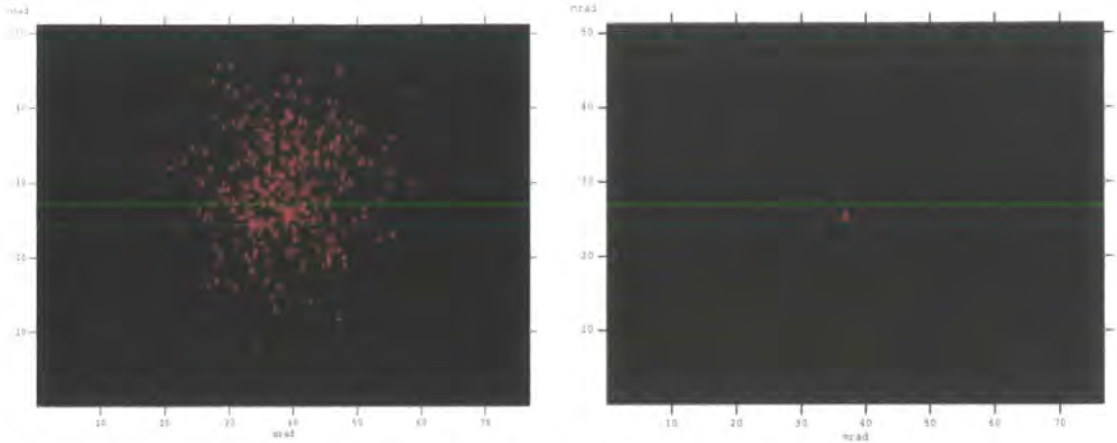


Figure 1.16: An example of a camera lid CCD image of a star before mirror alignment (left) and after alignment (right) (Image courtesy of the H.E.S.S. collaboration)

1.5.4 Camera

Each of the H.E.S.S. cameras consists of 960 Photonis XP2960 photomultiplier tubes (PMT) [3]. PMTs are used for several reasons;

- The Cherenkov flash is very faint and lasts typically only a few nanoseconds. PMTs are the only detector able to respond on this kind of timescale with any usable efficiency.
- The dead time of the detector during read out is much shorter than for example a CCD detector.
- PMTs are more sensitive than a CCD - a larger reflector would be required for a CCD to achieve the same system sensitivity.
- Blue light sensitive PMTs are available, which are particularly suited to the Cherenkov spectrum.
- PMTs are relatively inexpensive in comparison to CCDs.

Each PMT subtends an area of 0.16° diameter on the sky giving a total 5° field of view, and each is equipped with a Winston cone designed to minimise the amount of background light entering the PMT and also to capture reflected

Cherenkov light that would otherwise fall between the tubes. To make construction and maintenance as simple as possible, the PMTs are mounted in the camera body in sets of drawers, Fig.(1.17). There is a total of 60 draw-

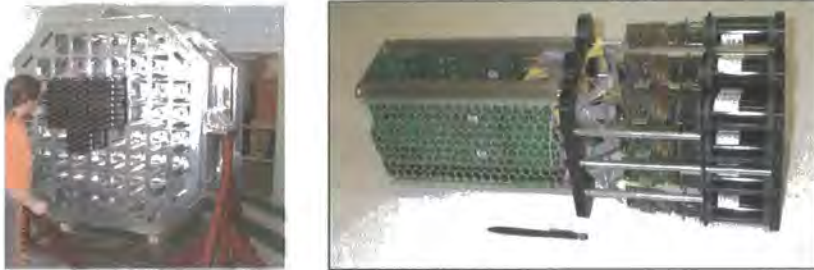


Figure 1.17: The complete H.E.S.S. camera (shown partly built left) consists of 960 photomultiplier tubes (PMT). It is a modular design consisting of 60 drawers, each drawer (right) containing 16 PMT's with their associated acquisition and control/interface cards (courtesy of the H.E.S.S. Collaboration).

ers, each drawer containing 16 PMTs, two acquisition cards, each reading the data from 8 PMTs, and the control/interface card. The analogue signal from the PMTs is digitised in the drawers and sent to the acquisition electronics, which are mounted in the rear of the crate. For each PMT there are three channels; the high-gain (HG), which is used to detect signal charges up to 200 photo-electrons, the low-gain (LG) for signal charges in the range 15 to 1600 photo-electrons (each using an analog ring sampler to store the signal) and the trigger channel. The triggering system is performed in three steps.

- A single pixel must have the equivalent of 4 photo-electrons at the PMT cathode within an interval of 1.5ns.
- A coincidence of 3 triggered pixels, satisfying the first condition, is required within a sector (A sector being a square group of 64 pixels. For the current camera configuration there are 38 overlapping sectors).
- In stereo mode two telescopes must trigger within 80ns of each other

A full description of the cameras can be found in [1] and of the trigger system in [36].

1.6 Microquasars

1.6.1 Introduction

By definition a microquasar is an x-ray binary that displays relativistic jets. An x-ray binary, the first of which was detected in 1962 with the Aerobee rocket, contains a compact object, a neutron star or black hole, accreting matter from a companion star. X-ray binaries are split into two categories, the high-mass x-ray binaries (HMXB) and the low-mass x-ray binaries (LMXB). They are classified depending on the nature of the companion star, which inevitably leads to differing accretion processes and spectral properties.

- **Low-mass x-ray binaries**, contain a later than type A companion star or in very evolved systems, a white dwarf, with $M \leq 1M_{\odot}$. Accretion onto the compact object is by Roche-Lobe overflow through the L1 Lagrangian point. The optical spectrum is dominated by the accretion disk through reprocessing of x-rays produced in the disk via viscous heating. Optical emission from the companion contributes $\leq 1\%$ of the total output.
- **High-mass x-ray binaries** can fall into two groups. The first group contains young more massive companion stars in the form of an O or a B class star. The compact object is well within the supersonic wind of the companion star that can remove up to $10^{-6}M_{\odot}$ per year. Accretion of this matter through capture as it passes the compact object dominates over Roche-Lobe overflow, the companion star underfilling its Roche-Lobe the majority of the time in all except the brightest systems. The second group contains a Be type star as the companion. Be stars rotate extremely fast producing a circumstellar disk. As the compact object, which is usually in a fairly wide orbit, passes through the disk, x-rays are emitted. Unlike the more evolved stars in LMXB's, the optical and ultraviolet emission of the companion is comparable to that of the x-ray emission, produced as matter is captured by the compact object.

Fig.(1.18) shows the distribution of the 280 catalogued x-ray binaries of which 130 are HMXB's [69] and 150 are LMXB's [70]. It clearly shows the large

concentration of LMXB's around the galactic centre, whereas the HMXB's are distributed in the spiral arms of the galaxy where there are much younger and more massive stars.

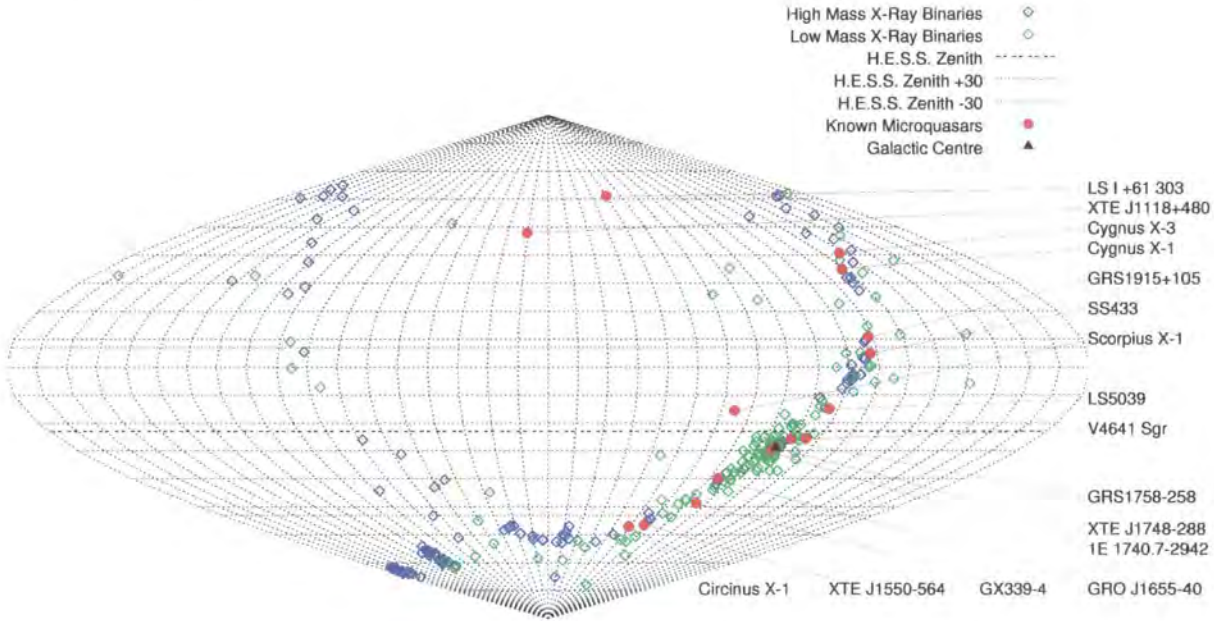


Figure 1.18: Sanson-Flamsteed projection showing the distribution of high-mass x-ray binaries, HMXB's, low-mass x-ray binaries, LMXB's and microquasars in the Galaxy. The Magellanic clouds can be clearly seen in bottom left hand section populated by HMXB's.

1.6.2 Active Galactic Nuclei (AGN) Analogy

Out of the 280 catalogued x-ray binaries only a handful are classified as being microquasars [90]. Table 1.1 summarises those microquasars known to date. The term microquasar stems from their similarity with their larger scale counterpart, quasars, a sub-group of radio-loud active galactic nuclei (RLAGN), and is by definition an x-ray binary displaying relativistic radio jets, in effect an RLAGN with much smaller mass, length and time scales. One of the important aspects of microquasars is the chance to observe and study mechanisms in RLAGN, which normally occur over millenia, within a human timescale.

Name & Position (J2000)	System	D (kpc)	P_{orb} (days)	M_{com} M_{\odot}	Jet velocity β_{app} β_{int}		θ ($^{\circ}$)	Jet Size (AU)
High Mass X-ray Binaries								
V4641 Sgr. 18 ^h 19 ^m 21 ^s .63 −25°24′25″.9	BH	10	2.8	9.6	≥ 9.5	-	-	-
LS5039 18 ^h 26 ^m 15 ^s .06 −14°50′54″.3	NS?	2.9	4.4	1-3	≥ 0.15	≥ 0.15	< 81	10-1000
SS 433 19 ^h 11 ^m 49 ^s .57 +4°58′57″.8	BH?	4.8	13.1	11±5?	0.26	0.26	79	10 ⁴ – 10 ⁶
Cygnus X-1 19 ^h 58 ^m 21 ^s .68 +35°12′05″.8	BH	2.5	5.6	10.1		> 0.6	40	40
Cygnus X-3 20 ^h 32 ^m 25 ^s .77 +40°57′28″.0	BH?	9	0.2	-	0.69	0.43	73	10 ⁴
LS I +61 303 02 ^h 40 ^m 31 ^s .67 +61°13′45″.6	NS?	2	26.5	-	≥ 0.4	-	-	-
Low Mass X-ray Binaries								
XTE J1118+480 11 ^h 18 ^m 10 ^s .79 +48°02′12″.3	BH	1.9	0.17	6.9	-	-	-	≤ 0.03
Circinus X-1 15 ^h 20 ^m 40 ^s .84 −57°10′00″.5	NS	5.5	16.6	-	≥ 0.1	≥ 0.1	> 70	> 10 ⁴
XTE J1550-564 15 ^h 50 ^m 58 ^s .67 −56°28′35″.3	BH	5.3	1.5	9.4	≥ 2	-		10 ³
Scorpius X-1 16 ^h 19 ^m 55 ^s .09 −15°38′24″.9	NS	2.8	0.79	1.4	0.68	0.45	44	40
GRO J1655-40 16 ^h 54 ^m 00 ^s .16 −39°50′44″.7	BH	3.2	2.6	7.02	1.1	0.92	72-85	8000
GX 339-4 17 ^h 02 ^m 49 ^s .40 −48°47′23″.3	BH	> 6	1.76	5.8 ± 0.5	-	0.9 [38]	26 [38]	< 4000
1E 1740.7-2942 17 ^h 43 ^m 54 ^s .82 −29°44′42″.8	BH?	8.5?	12.5?	-	-	-	-	> 10 ⁶
XTE J1748-288 17 ^h 48 ^m 05 ^s .06 −28°28′25″.8	BH?	≥ 8	-	> 4.5?	1.3	> 0.9	-	> 10 ⁴
GRS 1758-258 18 ^h 01 ^m 12 ^s .40 −25°44′36″.1	BH?	8.5?	18.5?	-	-	-	-	10 ⁶
GRS 1915+105 19 ^h 15 ^m 11 ^s .55 +10°56′44″.8	BH	12.5	33.5	14	1.2-1.7	0.92-0.98	66-70	10-10 ⁴

Table 1.1: List of currently known microquasars and their properties. [90][91]

Indeed some of the outbursts so far observed in a microquasar have been too fast and too short for some telescopes to respond, necessitating the need for some means of predicting activity. Of course this would only be applicable if the morphological similarities between RLAGN and microquasars extends to the physical processes within them. It is therefore worth noting the properties, which are common to both.

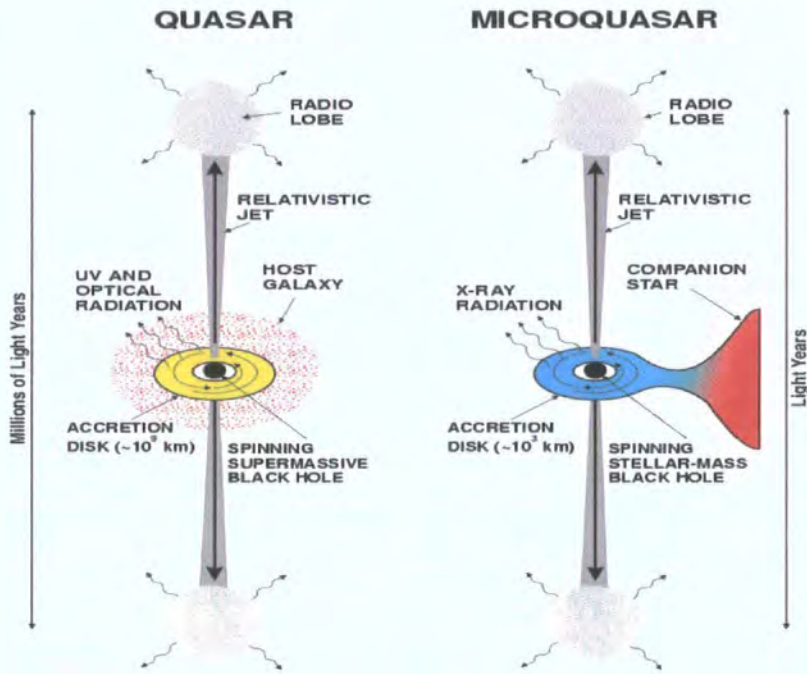


Figure 1.19: Analogy of Quasars and Microquasars. [82]

- Both objects contain a compact object, a supermassive black hole in the case of RLAGN and solar mass black hole or neutron star in the case of a microquasar. In the case of the RLAGN this object has mass of the order $10^8 M_{\odot}$ in comparison to a few M_{\odot} for a microquasar. While some binary star systems that have a neutron star as the compact object do display relativistic jets, morphologically one could argue that they differ from RLAGN, and the jet forming mechanisms may not be analogous to those with a black hole.

- The second property is an accretion disk. In the case of an RLAGN, this is believed to be formed from surrounding stellar matter and interstellar dust and gas and is around 10^9 km [82] across, with thermal emission in the UV and optical part of the spectrum. The black hole in a microquasar accretes matter from its companion star. This disk is around 10^6 times smaller than the former and emits thermal radiation in the x-ray part of the spectrum. The scaling factor here is again directly related to the mass of the black hole where

$$T_{col} \propto \left(\frac{10M_{\odot}}{M} \right)^{1/4} \quad (1.20)$$

with T_{col} is the colour temperature of the disk and M is the mass of the disk [76].

- The third property is the existence of collimated jets of relativistic particles. These have been known to exist in RLAGN for some time but have only relatively recently been seen from objects within our own galaxy [81]. It is also known that some RLAGN emit in the VHE γ -ray region, suggesting some microquasars may also be detectable in this region. It is in these jets that particles are accelerated to high enough energies to produce VHE γ -ray radiation.

One class of RLAGN, blazars, are known to emit VHE γ -rays, see for example [2]. Blazars, a sub-class of RLAGN that represent less than 1% of all AGN, emit jets of relativistic particles close to the line of sight of the observer and often display the illusion of jet velocities greater than the speed of light. In addition, the extreme velocities lead to Doppler enhanced frequencies and fluxes. It is an interesting fact that only one non-blazar AGN, M87 [10], has ever been detected at VHE energies. If microquasars have more than a morphological similarity with these objects, then, with the flux sensitivities of current experiments, ‘microblazars’ may have a higher probability of detection in the VHE spectrum, although the recent detection of LS5039 [5] may serve to refute this point. Microblazars may be few in number, assuming the angle of microquasar jets is homogeneously distributed then only $\sim 0.5\%$ can be expected to have

their jets within 5° of the observer's line of sight. The relativistic effects are discussed in the following sections.

1.6.3 Superluminal Motion

Superluminal motion was first observed in AGN as expansion of matter that appeared to move faster than the speed of light (see for example [111]). This caused great concern when first observed, as it appeared to violate the theory of relativity. However, it was soon realised that this was nothing more than an optical illusion created by the intrinsic relativistic motion of the jets together with the angle of the line of sight to the observer [94].

Superluminal motion can be explained by considering a photon emitted from a blob of matter ejected from a central body at point O e.g. a black hole, at time $t = 0$ as shown in Fig.(1.20). A blob ejected at an angle θ to the line of sight in the direction of the observer is considered first. At a later time, $t = t$ the blob has travelled to point B with velocity v and emits a second photon. At this time the original photon has reached point C. The time difference between seeing the photon emitted at O at time $t = 0$ and that emitted from B at time t is approximately,

$$\Delta t = \frac{OC - OA}{c} = \frac{ct - vt \cos \theta}{c} \quad (1.21)$$

This is the apparent time for the blob to travel from A to B in the sky. Hence the apparent velocity is given by,

$$v_{app} = \frac{AB}{\Delta t} = \frac{vt \sin \theta}{ct - vt \cos \theta} \cdot c = \frac{c\beta \sin \theta}{1 - \beta \cos \theta} \quad (1.22)$$

where $\beta = v/c$. Now the apparent proper motion can be considered.

$$AB \sim d\phi \quad \text{where } \phi \text{ is small} \quad (1.23)$$

and hence μ_a , the proper motion of the approaching jet, given in radians per second is given by,

$$\mu_a = \frac{v_{app}}{d} \quad (1.24)$$

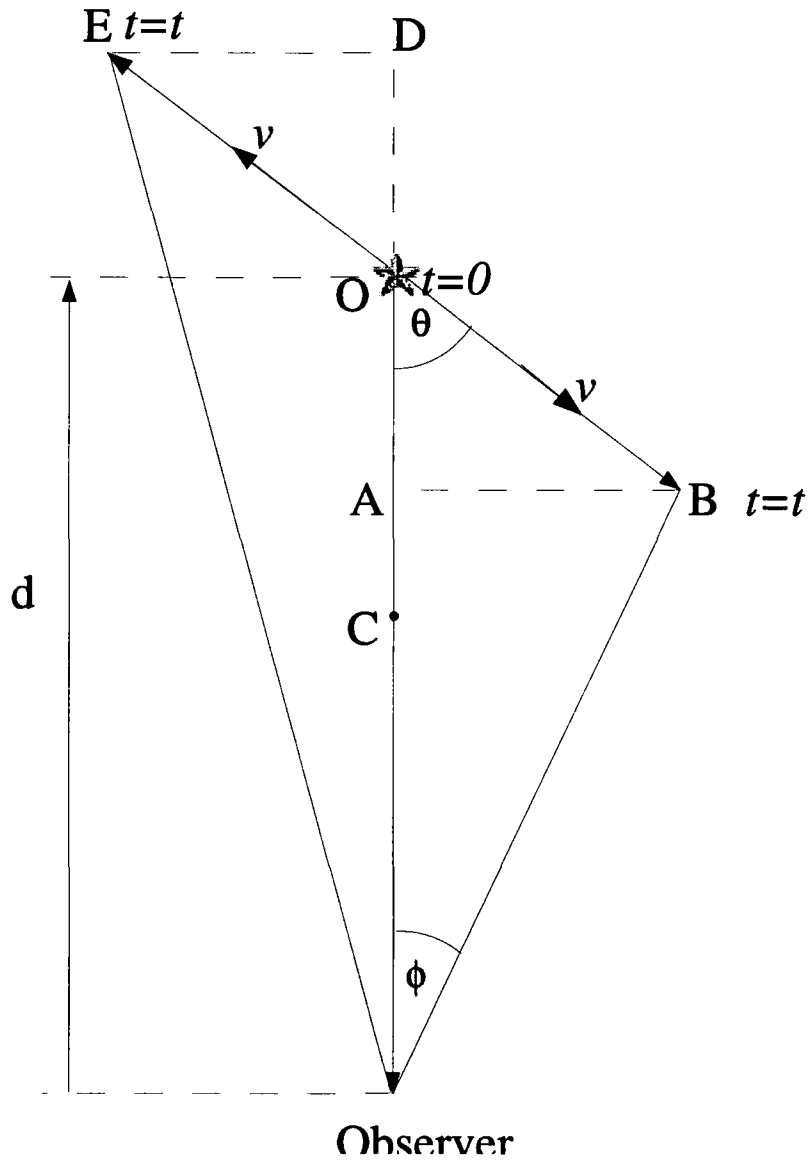


Figure 1.20: Geometry of superluminal motion.

Substituting Eq(1.22) gives,

$$\mu_a = \frac{\beta \sin \theta}{1 - \beta \cos \theta} \cdot \frac{c}{d} \quad (1.25)$$

In a similar fashion the receding jet can be given the same treatment. The time difference between seeing the photon emitted at O at time $t = 0$ and that emitted from E at time t in this case is approximately,

$$\Delta t = \frac{OC + OD}{c} = \frac{ct + vt \cos \theta}{c} \quad (1.26)$$

Thus the apparent velocity for the receding jet is given by,

$$v_{rec} = \frac{DE}{\Delta t} = \frac{vt \sin \theta}{ct + vt \cos \theta} \cdot c = \frac{c\beta \sin \theta}{1 + \beta \cos \theta} \quad (1.27)$$

and in a similar fashion the proper motion of the receding jet, μ_r is given by,

$$\mu_r = \frac{\beta \sin \theta}{1 + \beta \cos \theta} \cdot \frac{c}{d} \quad (1.28)$$

Dividing Eq.(1.25) by Eq.(1.28) gives,

$$\beta \cos \theta = \frac{(\mu_a - \mu_r)}{(\mu_a + \mu_r)} \quad (1.29)$$

and substituting for $\beta \cos \theta$ from Eq.(1.29) in Eq.(1.25) gives,

$$d = \frac{c \tan \theta}{2} \cdot \frac{(\mu_a - \mu_r)}{\mu_a \mu_r} \quad (1.30)$$

By squaring Eq.'s (1.29) and (1.30), setting $\beta = 1$ (its maximum value) using $\tan \theta = (\sec^2 \theta - 1)$ and applying the difference of two squares gives an equation for the maximum distance to the source,

$$d_{max} = \frac{c}{\sqrt{\mu_a \mu_r}} \quad (1.31)$$

1.6.4 Relativistic Doppler Factor

In the classical Doppler effect for sound waves the observed frequency depends differently on the velocities of the source and the observer, the reason being that there is an absolute frame of reference; the medium through which the sound waves travel. Special relativity does not allow for such an absolute frame and so the relativistic Doppler effect has to be treated differently, depending only on the relative velocities of the observer and source. Consider Fig.(1.21). When O' in frame S' coincides with O in frame S a flash is emitted with a period

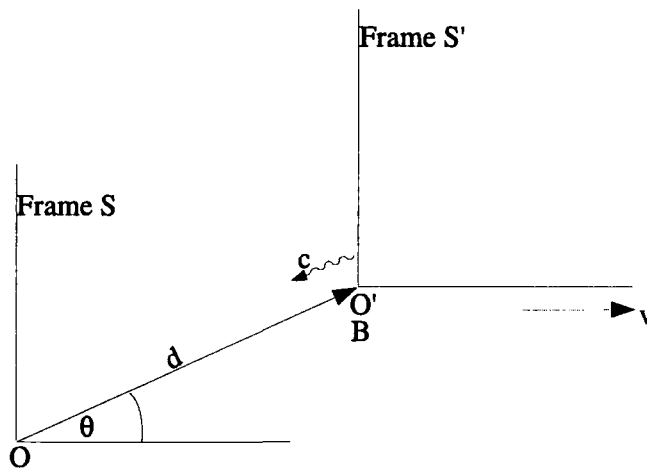


Figure 1.21: A source of origin in frame S' emits a photon toward the observer in frame S

$\Delta t' = T_0$. The source then moves with velocity $v \cos(\theta)$, relative to frame S . If another flash is emitted after one period, an observer B , who coincides with O' will see a dilated time interval between flashes given by,

$$\Delta t = \gamma \Delta t' = \gamma T_0 \quad (1.32)$$

In the time interval between flashes O' has moved a distance, $d = v \cos(\theta) \Delta t$, so the second flash takes a time $\frac{d}{c}$ to arrive at O . Hence the time of arrival at

O is given by,

$$T = \Delta t + \frac{d}{c} = \Delta t + \frac{v \cos(\theta) \Delta t}{c} = \gamma T_0 \left(1 + \frac{v \cos(\theta)}{c} \right) \quad (1.33)$$

Hence for photons emitted from a relativistically moving source, such as a jet, the frequencies observed become,

$$\nu_a = \nu_0 \cdot \frac{1}{\gamma \left(1 - \frac{v_a \cos(\theta)}{c} \right)} \quad \text{and} \quad \nu_r = \nu_0 \cdot \frac{1}{\gamma \left(1 + \frac{v_r \cos(\theta)}{c} \right)} \quad (1.34)$$

where the subscripts a and r refer to the approaching and receding jets respectively, the Doppler factors being given by,

$$\delta_a = \frac{\nu_a}{\nu_0} \quad \text{and} \quad \delta_r = \frac{\nu_r}{\nu_0} \quad (1.35)$$

1.6.5 Doppler Boosting

In addition to the frequency modifications caused by the Doppler effect, the flux of radiation received by the observer is also modified. This effect is known as Doppler boosting or ‘beaming’. The resultant flux seen by the observer from the approaching and receding jets is effectively increased or decreased respectively, and is given by [83],

$$S_a = S_0 \cdot \delta_a^{k-\alpha} \quad \text{and} \quad S_r = S_0 \cdot \delta_r^{k-\alpha} \quad (1.36)$$

where α is the spectral index of the emission, for $S_\nu \propto \nu^\alpha$, and k represents the geometry of the ejection. For a steady jet $k = 2$ and for discrete ejections $k = 3$. For very distant objects such as quasars, this beaming effect implies that flux of the receding jet is greatly diminished to the observer, making it undetectable, which can give the impression of a one-sided jet.

1.6.6 Spectral States of X-Ray Binaries

The spectrum and associated physical behaviour of x-ray binaries is generally described by the ‘state’ in which they currently exist. The states are

described here in terms of the model presented by [31] and [11], who use the ‘canonical’ terminology, and who also draw comparisons to the alternative, revised description suggested by [72]. An exception to these canonical states is GRS1915+105, the behaviour of which is not classified using the same terminology. This is discussed further in Section 2.8.1.

- **The Quiescent State.** This is the state occupied most of the time, sometimes called the ‘off’ state, and is associated with the lowest accretion rates. Sources are in a state of low luminosity with a low density in the inner accretion disk. The spectrum is well fitted by a hard, non-thermal, single power law [72].
- **Low/Hard State (LS).** This state is again associated with relatively low values of accretion, compared to other states. It is characterised by a hard x-ray spectrum, which can be modelled with a single power law. The thermal spectrum is very weak and a flat radio spectrum is observed, which is associated with a steady self-absorbed, low power jet [31]. The accretion disk is believed to truncate at a large radius and densities in the inner region are low. This state is generally associated with low luminosity, hence the term low/hard, [72] however, suggests this may not always be the case and classifies this state simply as the ‘hard’ state.
- **Intermediate State.** This state is described by [31] and [11] as consisting of two separate states, the hard intermediate state (HIMS) and the soft intermediate state (SIMS).
 In the HIMS the energy spectrum is softer than in the LS, with a weak thermal disk component and a steepening radio spectrum.
 In the SIMS the energy spectrum is again softer than in the HIMS with the disk component dominating. Radio emission is no longer detectable. [31] suggests that the sharp transition that occurs between the HIMS and the SIMS produces a rapid increase in the velocity of the jet producing shock fronts, which are detectable as powerful outbursts.
- **High/Soft State (HS).** This state is dominated by a strong soft ther-

mal disk component (classified by [72] as the ‘thermal dominated’ state). No radio emission is detected and only a weak power law component is present. This state is associated with the accretion disk having a small inner radius approaching the innermost stable circular orbit.

Fig.(1.22) show sample spectra for GX339-4 in both the LS and HS. McClintock and Remillard [72] conclude that there are no constraints placed on the order of which state transitions can occur, which if true, is unfortunate since using a series of observations to predict when a jet is launched could be an invaluable tool in triggering VHE γ -ray observations of microquasars. The model of Fender, Belloni and Gallo [31], on the other hand, presents a schematic for the order in which the transitions between states occur, at what point jet emission is likely to be seen and the points when the most energetic ejections are likely to take place. The 2002/2003 outburst of GX339-4 seem to corroborate this scheme [12]. According to this scheme, illustrated in Fig.(1.23), whilst in the LS, there is a steady jet with low bulk Lorentz factors, $\Gamma < 2$. As the spectrum softens and transits the HIMS-SIMS boundary there is the sudden increase in the bulk Lorentz factor with $\Gamma > 2$ with short, powerful outbursts produced by internal shocks.

This scheme suggests that if microquasars are to be detected in the LS from steady jets at VHE γ -ray energies, beaming will be more important than for the higher energy transitory events, where higher bulk Lorentz factors may allow detection at larger jet angles. In addition, monitoring of the spectral states will give an indication of when the short lived, high energy, transitory events might occur.

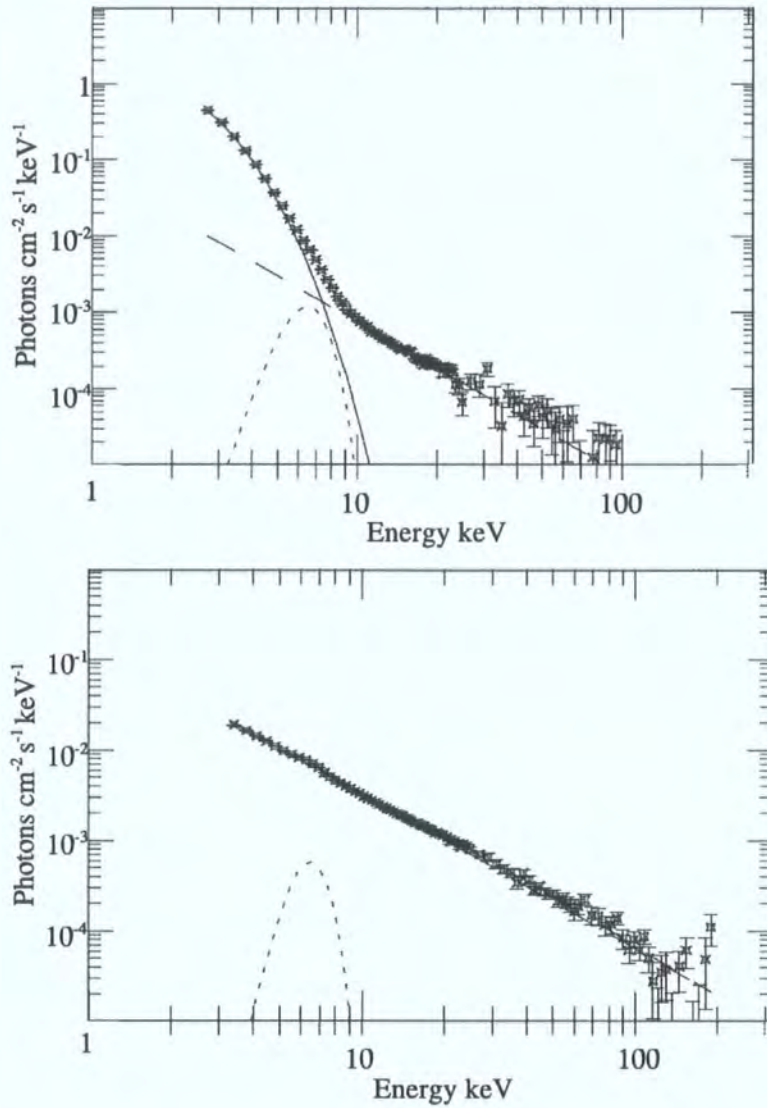


Figure 1.22: Sample spectra for GX339-4 from the Rossi X-Ray Timing Explorer (RXTE) data, showing an example of the difference in spectrum detected during the HS (top) and LS (bottom) of the source. In the HS, the spectrum is dominated by the thermal component from the accretion disk (solid line) below ~ 10 keV with a power law component at higher energies (dashed line). The dotted line in the HS plot represents an Fe line, which is included in the model. In contrast, in the LS, the spectrum is dominated by a power law (adapted from [72]).

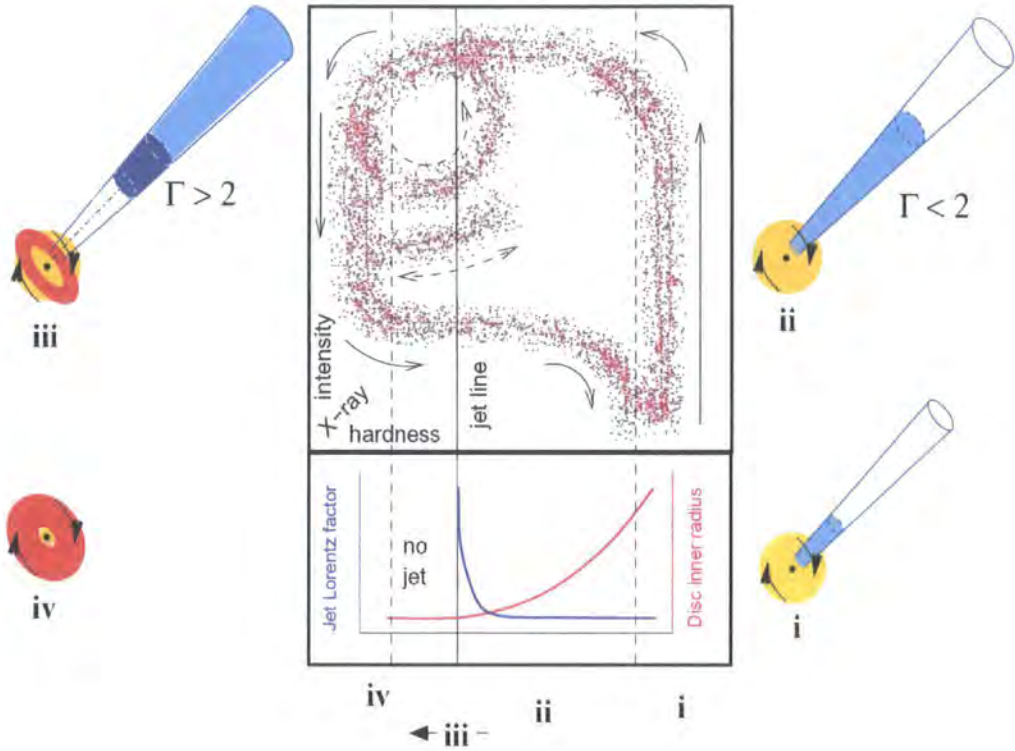


Figure 1.23: A schematic of the model for state transitions suggested by [31]. The upper box represents the x-ray hardness diagram, hardening from left to right, with the evolution from quiescence(i)→LS(ii)→(HIMS-SIMS)(iii)→HS(iv) starting in the lower right corner and moving in an anti-clockwise direction. The lower box represents the variation of (a) the bulk Lorentz factor, Γ , and (b) the inner accretion disk radius, with x-ray hardness. A steady jet with $\Gamma < 2$ is present in the LS. As the source crosses the ‘jet line’ between the HIMS and the SIMS short powerful outbursts are observed with $\Gamma > 2$. This only occurs in the one direction and not at SIMS-HIMS transition. The jet/disc sketches represent the relative contributions from the jet (blue), the corona (yellow) and accretion disc (red) during the different states.

Chapter 2

A Synchrotron Self-Compton Model for Microquasars

2.1 The Scenario

In order to predict possible γ -ray emission from microquasar jets maintaining the AGN-microquasar analogy, a code has been produced based on an existing synchrotron self-Compton model for AGN jets [39][40]. The parameterisation of the jet follows the AGN model closely, although some of the functions contained within the emissivity and absorption coefficients vary at an insignificant level. The basic outline of the model is contained within [39][40] but here a complete description is provided for two reasons

- a more in depth look is taken at some of the geometry and parameterisation and restraints placed on them to keep the model physical. Some of the equations used in [39][40], where factors and coefficients are used but not explicitly derived, are expanded upon e.g. coefficients of emissivity and absorption. This is done for greater clarity and for numerical coding purposes.
- the code produced varies in some respects from the description in [39][40], in particular the synchrotron frequencies which contribute to the inverse Compton process. Justification for these differences is made.

When applying the model to microquasars, only LMXBs are considered since the primary accretion process in HMXBs arises from the strong stellar wind of the massive companion star. As a result the photon field from the companion star will be a significant component of the inverse Compton process and this field is not included in this model.

2.1.1 Jet Geometry

The geometry of the jet is described by the relation between the distance along the jet, R , and the radius of a surface orthogonal to that axis, r , represented in Figure 2.1 and given by Eq.(2.1).

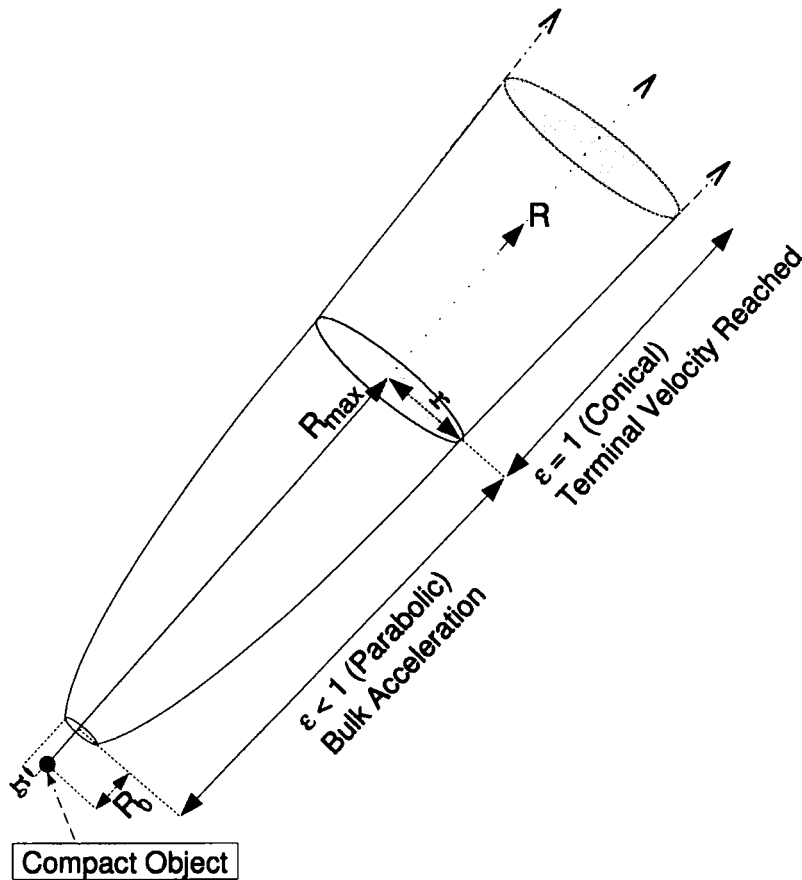


Figure 2.1: Schematic of Jet Model

$$r = r_0 \left(\frac{R}{R_0} \right)^\epsilon = r_0 x^\epsilon \quad (2.1)$$

For the purposes of predicting gamma ray emission from microquasars, only processes in the inner part of the jet are considered as this is where the highest electron energies are assumed to exist. The parameters in Eq.(2.1) have to be chosen with great care to maintain a physical representation of a jet i.e. a small opening angle, $\phi < 15^\circ$ [83] and a suitable shape. Assuming bulk acceleration throughout this region, $\epsilon < 1$ defines a parabolic shape [96]. Careless choice of these parameters would result in either ϕ or r_0 being unphysically large or small. This can be checked by rewriting Eq.(2.1) in a more recognisable form as the equation for a parabola;

$$R = \left(\frac{R_0}{r_0^{1/\epsilon}} \right) \cdot r^{1/\epsilon} \quad (2.2)$$

In Eq.(2.2) as ϵ gets smaller, the smaller ϕ becomes. Likewise, as $\left(\frac{R_0}{r_0^{1/\epsilon}} \right)$ gets larger, the smaller ϕ becomes, but to a lesser effect. Assuming a value for ϵ , R_{max} (the maximum extent of the jet often inferred from radio observations) and R_0 , simple calculus can give a relation between ϕ and r_0 , allowing suitable values to be chosen.

2.1.2 Parameterisation

As in [39][40] all physical parameters are constant on a plane orthogonal to the axis of the jet and vary along the jet according to simple power laws. The electron distribution $N(\gamma)$ is given by,

$$N(\gamma) = K\gamma^{-p} \quad (2.3)$$

where K is the electron density parameter and is given by,

$$K = K_0 x^{-\epsilon n} \quad \text{for } n > 0 \quad (2.4)$$

2. 2.2. Synchrotron Coefficients of Emissivity and Absorption

and γ is the local Lorentz factor of the electrons which varies between 1 and $\gamma = \gamma_{max}$ with,

$$\gamma_{max} = \gamma_{max}(R_0)x^{-\epsilon e} \quad \text{for } e > 0 \quad (2.5)$$

and p is the spectral index of the electron distribution and is related to the synchrotron spectral index, α_0 , by $p = 2\alpha_0 + 1$.

The bulk Lorentz factor describes acceleration throughout the jet and also follows a power law,

$$\Gamma = \Gamma_0 x^g \quad \text{for } g > 0 \quad (2.6)$$

The magnetic field B is described by,

$$B = B_0 x^{-\epsilon m} \quad \text{for } m > 0 \quad (2.7)$$

The optical depth τ is given by,

$$\tau = \sigma_T K r = \sigma_T K_0 x^{-\epsilon n} r_0 x^\epsilon = \sigma_T K_0 r_0 x^{-\epsilon(n-1)} = \tau_0 x^{-\epsilon(n-1)} \quad (2.8)$$

2.2 Synchrotron Coefficients of Emissivity and Absorption

2.2.1 Synchrotron Coefficient of Emissivity

The equation for the local volume emissivity coefficient for synchrotron radiation is given in [40] (bar a typographical error) by,

$$\epsilon_\nu^s(\nu, x) = \frac{c_1(\alpha_0)}{4\pi} K_0 B_0^{1+\alpha_0} \nu^{-\alpha_0} x^{-\epsilon(n+m(1+\alpha_0))} \quad (2.9)$$

A table giving values of $c_1(\alpha_0)$ is shown in [39] for specific values of α_0 without giving an explicit formula. Since the code produced, based on this model, is numerical and holds for a continuous range of α_0 , the origin of $c_1(\alpha_0)$ is laid out below and is always calculated explicitly in the code. The basis of the

2. 2.2. Synchrotron Coefficients of Emissivity and Absorption

derivation is the results obtained by [16] and defines the energy emitted per unit volume, per unit frequency, per unit time and is given by,

$$\frac{dW}{d\nu dt} = \left(\frac{4\pi e^3}{mc^2} \right) K B^{(p+1)/2} \left(\frac{3e}{4\pi mc} \right)^{(p-1)/2} a(p) \nu^{-(p-1)/2} \quad (2.10)$$

where

$$a(p) = \frac{2^{(p-1)/2} \sqrt{3} \Gamma[(3p-1)/12] \Gamma[(3p+19)/12] \Gamma[(p+5)/4]}{8\pi^{1/2} (p+1) \Gamma[(p+7)/4]} \quad (2.11)$$

Using Eqs.(2.4) and (2.7) with,

$$\epsilon_\nu^s(\nu, x) = \frac{1}{4\pi} \frac{dW}{d\nu dt} \quad \text{and} \quad \alpha_0 = \frac{p-1}{2}$$

Eq.(2.10) gives

$$\epsilon_\nu^s(\nu, x) = \frac{c_1(\alpha_0)}{4\pi} K_0 B_0^{\alpha_0+1} \nu^{-\alpha_0} x^{-\epsilon(n+m(\alpha_0+1))} \quad (2.12)$$

where

$$c_1(\alpha_0) = \left(\frac{4\pi e^3}{mc^2} \right) \left(\frac{3e}{4\pi mc} \right)^{\alpha_0} a(p) \quad (2.13)$$

Using Eq.(2.13), for $\alpha_0 = 0.5$, $c_1(\alpha_0) = 3.5899 \times 10^{-19}$, which is in agreement with [40]

2.2.2 Synchrotron Coefficient of Self-Absorption

Since the relativistic electrons occupy a relatively large volume, re-absorption of the synchrotron photons by the same electron distribution will occur. The derivation of the self absorption coefficient follows the same method as shown by [43]. Taking $N(p)$ as the electron distribution function in momentum space and $P(\nu, \gamma)$ as the spectral distribution of the power of the radiation from a single electron, then the coefficient for synchrotron self-absorption, K_ν^s , is given by,

$$K_\nu^s = \frac{c}{2\nu^2} \int \frac{dN(p)}{dp} P(\nu, \gamma) p^2 dp \quad (2.14)$$

2. 2.2. Synchrotron Coefficients of Emissivity and Absorption

Using the relations,

$$E = cp \quad p = \gamma mc \quad dp = mcd\gamma$$

and

$$N(p)4\pi p^2 dp = N(\gamma)d\gamma$$

Eq.(2.14) becomes,

$$K_\nu^s = \frac{1}{8\pi m\nu^2} \int \gamma^2 \frac{d}{d\gamma} \left(\frac{N(\gamma)}{\gamma^2} \right) P(\nu, \gamma) d\gamma \quad (2.15)$$

Substituting Eq.(2.3) and the definition for $P(\nu, \gamma)$ [43] below,

$$P(\nu, \gamma) = \frac{\sqrt{3}e^3 B}{mc^2} \frac{\nu}{\nu_c} \int_{\frac{\nu}{\nu_c}}^{\infty} K_{\frac{5}{3}}(\eta) d\eta \quad (2.16)$$

Eq.(2.15) becomes,

$$K_\nu^s = \frac{1}{8\pi m\nu^2} \int \gamma^2 \frac{d}{d\gamma} (K\gamma^{-(p+2)}) d\gamma \frac{\sqrt{3}e^3 B}{mc^2} \int_{\frac{\nu}{\nu_c}}^{\infty} K_{\frac{5}{3}}(\eta) d\eta \quad (2.17)$$

which simplifies to,

$$K_\nu^s = \frac{\sqrt{3}e^3 KB}{8\pi m^2 c^2 \nu^2} (-(p+2)) \int \gamma^{-(p+1)} d\gamma \frac{\nu}{\nu_c} \int_{\frac{\nu}{\nu_c}}^{\infty} K_{\frac{5}{3}}(\eta) d\eta \quad (2.18)$$

Using the identity,

$$\begin{aligned} & \int_0^\infty dE E^{-\beta} \frac{\nu}{\nu_c} \int_{\frac{\nu}{\nu_c}}^{\infty} K_{\frac{5}{3}}(\eta) d\eta \\ &= \frac{1}{4} \left(\frac{\beta + 7/3}{\beta + 1} \right) \Gamma \left(\frac{3\beta - 1}{12} \right) \Gamma \left(\frac{3\beta + 7}{12} \right) \left[\frac{3eB}{2\pi m^3 c^5} \right]^{\frac{(\beta-1)}{2}} \end{aligned} \quad (2.19)$$

valid for $\beta > \frac{1}{3}$, which with $E = \gamma mc^2$ and $\beta = p + 1$, can be rewritten,

$$\int_0^\infty d\gamma \gamma^{-(p+1)} \frac{\nu}{\nu_c} \int_{\frac{\nu}{\nu_c}}^\infty K_{\frac{5}{3}}(\eta) d\eta = \frac{1}{(mc^2)^{-p}} \frac{1}{4} \left(\frac{3p+10}{3(p+2)} \right) \Gamma\left(\frac{3p+2}{12}\right) \Gamma\left(\frac{3p+10}{12}\right) \left[\frac{3eB}{2\pi m^3 c^5} \right]^{\frac{p}{2}} \quad (2.20)$$

and with $x\Gamma(x) = \Gamma(x+1)$, Eq.(2.18) becomes,

$$K_\nu^s = \frac{\sqrt{3}e^3}{8\pi m^2 c^2} K B^{\frac{p}{2}+1} \nu^{-\frac{p}{2}+2} \frac{3e}{2\pi mc} \Gamma\left(\frac{3p+2}{12}\right) \Gamma\left(\frac{3p+22}{12}\right) \quad (2.21)$$

Defining,

$$g(p) = \frac{\sqrt{3}}{4} \Gamma\left(\frac{3p+2}{12}\right) \Gamma\left(\frac{3p+22}{12}\right) \quad (2.22)$$

and

$$d_1 = g(p) \left(\frac{e^3}{2\pi m^2 c^2} \right) \left(\frac{3e}{2\pi mc} \right)^{p/2} \quad (2.23)$$

with $\alpha_0 = \frac{p-1}{2}$, then Eq.(2.21) can be rewritten as,

$$K_\nu^s = d_1(\alpha_0) K B^{1.5+\alpha_0} \nu^{-\alpha_0-\frac{5}{2}} \quad (2.24)$$

Substituting Eqs.(2.4) and (2.7) gives the final form for the coefficient of emissivity,

$$K_\nu^s = d_1(\alpha_0) K_0 B_0^{1.5+\alpha_0} \nu^{-\alpha_0-\frac{5}{2}} x^{-\epsilon[n+m(1.5+\alpha_0)]} \quad (2.25)$$

2.3 Maximum Synchrotron Frequency

Synchrotron radiation is emitted when a charged particle, in this case an electron, interacts with a magnetic field. To obtain an equation for the maximum synchrotron frequency as used in the code, the Lorentz force is equated to the centrifugal force felt by the electron.

$$\frac{Bev_\perp}{c} = \frac{\gamma m_0 v^2}{r_s} \quad (2.26)$$

where r_s is the radius of revolution of the electron around the magnetic field. Rearranging Eq.(2.26) and substituting $\omega = \frac{v_{\perp}}{r_s}$ gives the angular frequency of revolution,

$$\omega_B = \frac{Be}{\gamma m_0 c} \quad (2.27)$$

giving an angular period,

$$\Delta t = \frac{\gamma m_0 c}{Be} \quad (2.28)$$

For highly relativistic electrons, the radiation appears to the observer in a beam whose half angle $d\vartheta \approx \frac{1}{\gamma}$, and the observer will see it for a time Δt_2 given by,

$$\Delta t_2 = 2d\vartheta \Delta t \quad (2.29)$$

Substituting for $d\vartheta$ and Δt gives,

$$\Delta t_2 = \frac{2m_0 c}{Be} \quad (2.30)$$

Hence if an electron emits a photon, then travels a distance l during time Δt_2 and emits another photon, the difference between the arrival times of the photons will be,

$$\Delta t_0 = \left(\frac{l}{v_{\parallel}} - \frac{l}{c} \right) \quad (2.31)$$

Since $l \approx v_{\parallel} \Delta t_2$

$$\Delta t_0 = \left(1 - \frac{v_{\parallel}}{c} \right) \Delta t_2 \quad (2.32)$$

Using the approximation $\left(1 + \frac{v_{\parallel}}{c} \right) \approx 2$,

$$\left(1 - \frac{v_{\parallel}}{c} \right) \approx \frac{1}{2} \left(1 - \frac{v_{\parallel}^2}{c^2} \right) = \frac{1}{2\gamma^2} \quad (2.33)$$

and Eq.(2.32) becomes,

$$\Delta t_0 = \frac{m_0 c}{Be\gamma^2} \quad (2.34)$$

Hence the frequency of the synchrotron radiation, ν^s , for an electron with Lorentz factor γ in a magnetic field B is,

$$\nu^s = \frac{1}{2\pi \Delta t_0} \quad (2.35)$$

$$\nu^s = \left(\frac{e}{2\pi m_0 c} \right) \gamma^2 B \quad (2.36)$$

and the maximum synchrotron frequencies produced by those electrons in the distribution $N(\gamma)$ with the maximum Lorentz factor γ_{max} ,

$$\nu_{max}^s = \left(\frac{e}{2\pi m_0 c} \right) \gamma_{max}^2 B \quad (2.37)$$

As a consequence of the power law properties along the jet of B and γ_{max} , the maximum synchrotron frequency also depends on the position in the jet, x . Substituting for B and γ_{max} from Eqs.(2.7) and (2.5) respectively, Eq.(2.37) becomes,

$$\nu_{max}^s = \nu_{max}^s(R_0) x^{-\eta} \quad (2.38)$$

where,

$$\nu_{max}^s(R_0) = \left(\frac{e}{2\pi m_0 c} \right) \gamma_{max}^2(R_0) B_0 \quad (2.39)$$

and

$$\eta = \epsilon(2e + m) \quad (2.40)$$

2.4 Synchrotron Self Absorption Frequency

In Section 2.1.2 the synchrotron spectrum, P_ν , for a power law distribution of electrons, as used in this model and given by Eq.(2.3), was defined as having a spectral index α_0 and can be described by $P_\nu \propto \nu^{-\alpha_0}$. In the absence of self-absorption this power law relationship would extend to low frequencies. However, at these lower frequencies the synchrotron emission is reabsorbed by the distribution of electrons and the source becomes optically thick. To be consistent with the model defined in [39], the frequency at which there is a maximum in the synchrotron spectrum, after which the frequencies are just becoming self-absorbed, is taken as the self-absorption frequency, ν_{abs}^s . Emission below this frequency, where $P_\nu \propto \nu^{\frac{5}{2}}$ is neglected [40]. This corresponds to an optical depth, τ_m , which defined in terms of the coefficient of absorption

for the synchrotron process, K_ν^s , is given by,

$$K_\nu^s \chi = \tau_m \quad (2.41)$$

where $\chi = \frac{2r}{\sin\theta}$ is the path length (see for example [43]) with θ the angle of the jet to the observers line of sight. τ_m is the optical depth corresponding to this frequency and for a homogeneous slab approximation [89] is given by,

$$e^{\tau_m} = 1 + \tau_m \frac{2\alpha_0 + 5}{5} \quad (2.42)$$

which is solved for numerically in the code. Substituting for K_ν^s (Eq.(2.25)) and χ in Eq.(2.41) and rearranging for ν gives an equation for the self absorption frequency at the base of the jet,

$$\nu_{abs}^s(R_0) = \left[\frac{2d_1(\alpha_0)K_0B_0^{(1.5+\alpha_0)}r_0}{\sin\theta\tau_m(\alpha_0)} \right]^{\frac{2}{5+2\alpha_0}} \quad (2.43)$$

This equation is strictly only valid for $\theta = \frac{\pi}{2}$ as Eq.(2.42) is for a homogeneous slab where all parameters remain constant on that surface. As θ decreases and the direction of the path length becomes more parallel to the jet axis, the more the parameters such as B and K change in accordance to the defined power laws along that path, and the slab approximation worsens. It is worth noting that [39] use an alternative equation for when $\theta \leq \phi$. Such cases would be blazars where the observer's line of sight is very close to the jet axis. However, in a study of 3C 279 where $\theta = 3^\circ$, seen in section (2.7), there is negligible difference between the synchrotron spectrum results obtained in [78] and that produced by this code. Hence this approximation for the self-absorption frequency will be used for all angles, θ . A more complete approximation suitable to a continuous change in θ will be addressed at a later date.

The self-absorption frequency also varies along the jet and is obtained by substituting Eqs.(2.1) (2.4), (2.7) for r_0 , K_0 and B_0 respectively in Eq.(2.43) giving,

$$\nu_{abs}^s(R) = \nu_{abs}^s(R_0)x^{-k_m} \quad (2.44)$$

where,

$$k_m = \frac{2\epsilon}{5 + 2\alpha_0} [n + m(1.5 + \alpha_0) - 1] \quad (2.45)$$

2.5 Synchrotron Luminosity

The synchrotron luminosity is calculated for a given frequency by considering a small cross section of the jet, dR at a distance R from the compact object (Fig.(2.2)) The volume of this cross section is thus,

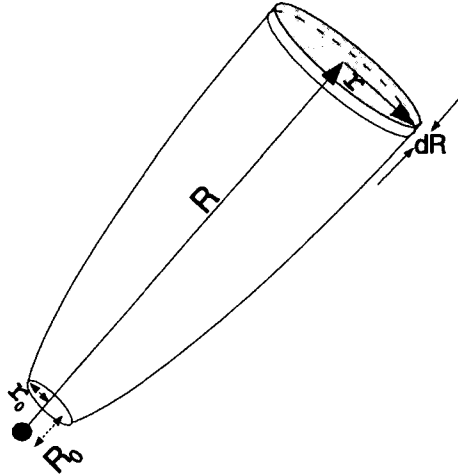


Figure 2.2: Geometry of a Cross Section of the Jet

$$V = \pi r^2 dR \quad (2.46)$$

Substituting Eq.(2.1) in the above equation, and setting $dx = \frac{dR}{R_0}$, the synchrotron luminosity for this cross section is given by,

$$dL_s(\nu) = 4\pi\epsilon_\nu^s(\nu, x)\pi r_0^2 \left(\frac{R}{R_0}\right)^{2\epsilon} R_0[\delta(x, \theta)]^{2+\alpha_0} dx \quad (2.47)$$

where $[\delta(x, \theta)]^{2+\alpha_0}$ is the Doppler boosting factor for a jet with continuous injection of particles [83] and $\delta(x, \theta)$ is the usual Doppler factor given by,

$$\delta(x, \theta) = \frac{1}{(\Gamma(x) - [\Gamma^2(x) - 1]^{\frac{1}{2}} \cos\theta)} \quad (2.48)$$

where Γ is given by equation Eq.(2.6).

Eq.(2.47) reduces to,

$$dL_s(\nu) = 4\pi^2 \epsilon_\nu^s(\nu, x) r_0^2 R_0 x^{2\epsilon} [\delta(x, \theta)]^{2+\alpha_0} dx \quad (2.49)$$

which is equivalent to that in [40] for $r_0 = R_0$. Since from equation Eq.(2.12),

$$\epsilon_\nu^s(\nu, 1) = \frac{c_1(\alpha_0)}{4\pi} K_0 B_0^{\alpha_0+1} \nu^{-\alpha_0} \quad (2.50)$$

and combining the powers on x , Eq.(2.49) can be rewritten,

$$dL_s(\nu) = 4\pi^2 \epsilon_\nu^s(\nu, 1) r_0^2 R_0 x^{\xi-1} [\delta(x, \theta)]^{2+\alpha_0} dx \quad (2.51)$$

where,

$$\xi - 1 = \epsilon(2 - n - m[1 + \alpha_0]) \quad (2.52)$$

The value of ξ dictates which part of the jet dominates the observed luminosity. For $\xi < 1$, the luminosity in the inner part of the jet dominates (since $x^{\xi-1} \rightarrow 0$ as $x \rightarrow \infty$). Likewise the opposite is true for $\xi > 1$, when the outer part of the jet dominates the luminosity.

The synchrotron spectrum for the entire jet is calculated by integrating equation Eq.(2.51) for each frequency between $\min(\nu_{abs}^s)$ and $\max(\nu_{max}^s)$, giving,

$$L_s(\nu) = 4\pi^2 \epsilon_\nu^s(\nu, 1) r_0^2 R_0 \int_{x_1(\nu)}^{x_2(\nu)} x^{\xi-1} [\delta(x, \theta)]^{2+\alpha_0} dx \quad (2.53)$$

For a given frequency, ν , the lower limit of the integration, x_1 , is set to 1 if $\nu \geq \nu_{abs}^s(R_0)\delta(1, \theta)$. If $\nu < \nu_{abs}^s(R_0)\delta(1, \theta)$, x_1 is set to the point along the axis of the jet, x , where $\nu = \nu_{abs}^s(x)\delta(x, \theta)$. To illustrate this, Figure (2.3) shows how the synchrotron self absorption frequency, $\nu_{abs}^s(x)\delta(x, \theta)$ varies with θ , as a function

of the self absorption frequency at the base of the jet, $\nu_{abs}^s(R_0)\delta(1, \theta)$. For all values of $\frac{\nu}{\nu_{abs}^s(R_0)\delta(1, \theta)} < 1$, a root finding routine calculates $\nu = \nu_{abs}^s(x_1)\delta(x_1, \theta)$. An example can be seen for $\frac{\nu}{\nu_{abs}^s(R_0)\delta(1, \theta)} = 0.8$ with $\theta = 30^\circ$. The intersection near $x = 8$ is the value calculated and used for x_1 . One point to note is the case where $\frac{\nu}{\nu_{abs}^s(R_0)\delta(1, \theta)} > 1$ and θ is small, an example of which can be seen when $\frac{\nu}{\nu_{abs}^s(R_0)\delta(1, \theta)} = 1.2$ and $\theta = 15^\circ$. Between approximately $x = 1.5$ and $x = 3$, the self absorption frequency rises above the frequency in question and as such there will be negligible emission in this region. However, the code includes this region and sets $x_1 = 1$, because the frequency is above $\nu_{abs}^s(R_0)\delta(1, \theta)$. This increase in the synchrotron self absorption frequency occurs simply due to Doppler boosting and, as can be seen, if $\delta = 1$ the self absorption frequency never goes above $\nu_{abs}^s(R_0)$. One of the future options for the code would be to include routines which calculate the values of x where the self absorption frequency behaves in this manner so that these regions can be omitted. To date this has not been necessary as the contribution from these regions has not contributed significantly to the output. This is only seen as a problem when k_m is unusually small, together with small θ and Γ_0 close to 1, which results in a large non-emitting region.

In an analogous way, the upper limit of the integration, x_2 , is set to x_{max} if $\nu \leq \nu_{max}^s\delta(x_{max}, \theta)$. If $\nu_{max}^s(R_0)\delta(1, \theta) > \nu > \nu_{max}^s(x_{max})\delta(x_{max}, \theta)$ then again a routine calculates the position, x , along the jet where $\nu = \nu_{max}^s(x)\delta(x, \theta)$ and sets this value to x_2 .

2.6 Inverse Compton Luminosity

The calculation for the inverse Compton luminosity assumes that all the contributing photons originate only in the synchrotron emissivity and any external seed field is not included. The equation to calculate the inverse Compton luminosity is adopted from [39] and is given by,

$$L_c(\nu) = \frac{3}{8}\pi A(\alpha_0)c_1(\alpha_0)\tau_0 K_0 B_0^{1+\alpha_0} r_0^2 R_0 \nu^{-\alpha_0} \times \int_{x_1(\nu)}^{x_2(\nu)} x^{l-1} [\delta(x, \theta)]^{2+\alpha_0} \ln \left[\frac{\nu_2(x)}{\nu_1(x)} \right] dx \quad (2.54)$$

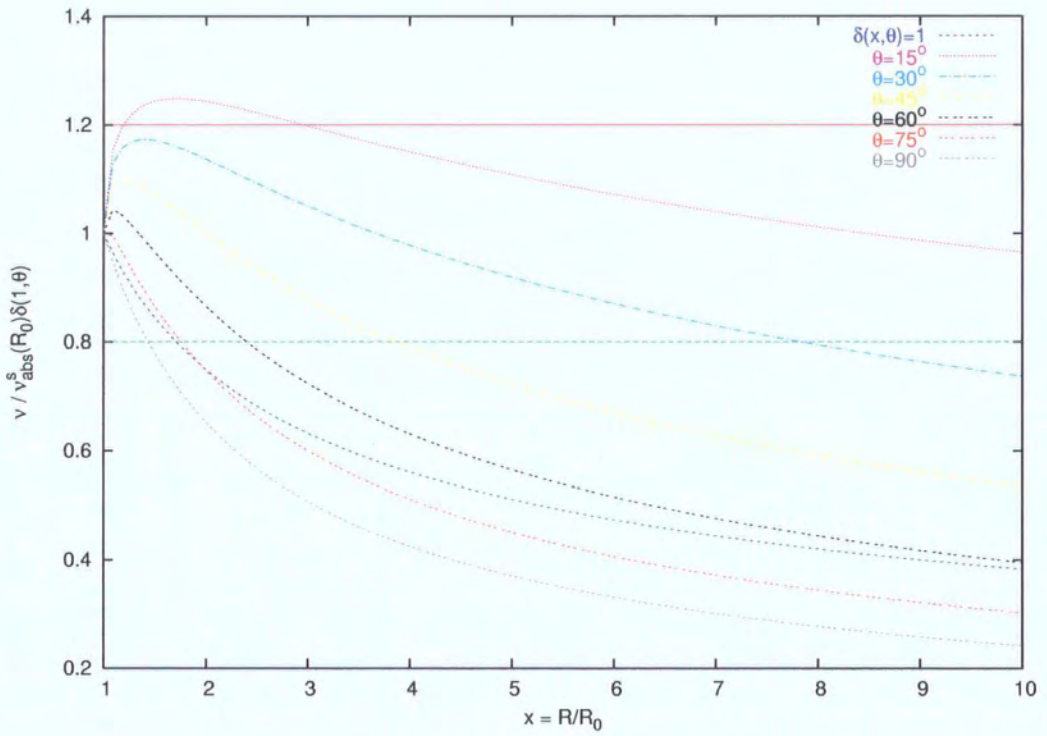


Figure 2.3: Variation of ν_{abs}^S due to Doppler boosting for various angles of the jet to the observer's line of sight, θ .

where $A(\alpha_0)$ is given in [16] and is defined as,

$$A(\alpha_0) = 2^{p+3} \frac{p^2 + 4p + 11}{(p+1)(p+3)^2(p+5)} \quad (2.55)$$

and

$$l - 1 = \epsilon(3 - 2n - m(1 + \alpha_0)) \quad (2.56)$$

As with ξ in the synchrotron luminosity function, l determines which part of the jet produces the highest luminosity. For $l > 1$, emission from the outer part of the jet dominates. Likewise if $l < 1$ the inner part dominates.

2.6.1 Inverse Compton Frequency Range

The range of inverse Compton frequencies emitted is governed by the frequencies that can contribute to the scattering process. In the case of the synchrotron calculation this was simply governed by the self absorption frequency at the lower limit and the maximum synchrotron frequency at the upper limit. For the inverse Compton process the Klein-Nishina cross section must also be considered. At the base of the jet the synchrotron frequencies range from $\nu_{max}^s(R_0)$, the maximum synchrotron frequency, to $\nu_{abs}^s(R_0)$, the self absorption frequency. Since the maximum synchrotron frequency produced here is the largest synchrotron frequency produced anywhere in the jet and the base of the jet has the largest local Lorentz factors, then the maximum inverse Compton frequency produced, ignoring the Klein-Nishina cross-section and assuming Thomson scattering, is given by,

$$\nu_{ic}(max) = \nu_{max}^s(R_0)\gamma_{max}^2(R_0) \quad (2.57)$$

However, the Klein-Nishina cross-section is going to have a considerable effect on this, producing a cut off at a lower frequency and lower fluxes at higher inverse Compton frequencies than dictated by Eq.(2.57). The Klein Nishina scattering cross section has already been discussed in Section 1.3.2. To apply this definition throughout the jet, complete with changing Lorentz factors, electron densities and Doppler boosting would be very complicated and unjusti-

fiably time consuming. The Klein-Nishina cross section defines the probability of interaction for an electron of a given energy with different photon energies. The model uses a distribution of electrons with a further distribution of energies dictated by the local Lorentz factor. In order to apply the Klein-Nishina cross section implicitly it would be necessary to know the energy of each electron in the distribution and what energy photon it was interacting with. This would have to be applied to each electron in the distribution and would require simulation rather than the numerical model described here. Hence, to include Klein-Nishina effects an approximation is used for the cross section. It is assumed therefore that the Klein-Nishina cross section is approximated by a step function at $\gamma_{max}(R_0)h\nu/m_e c^2 = 1$. The step function is used firstly for

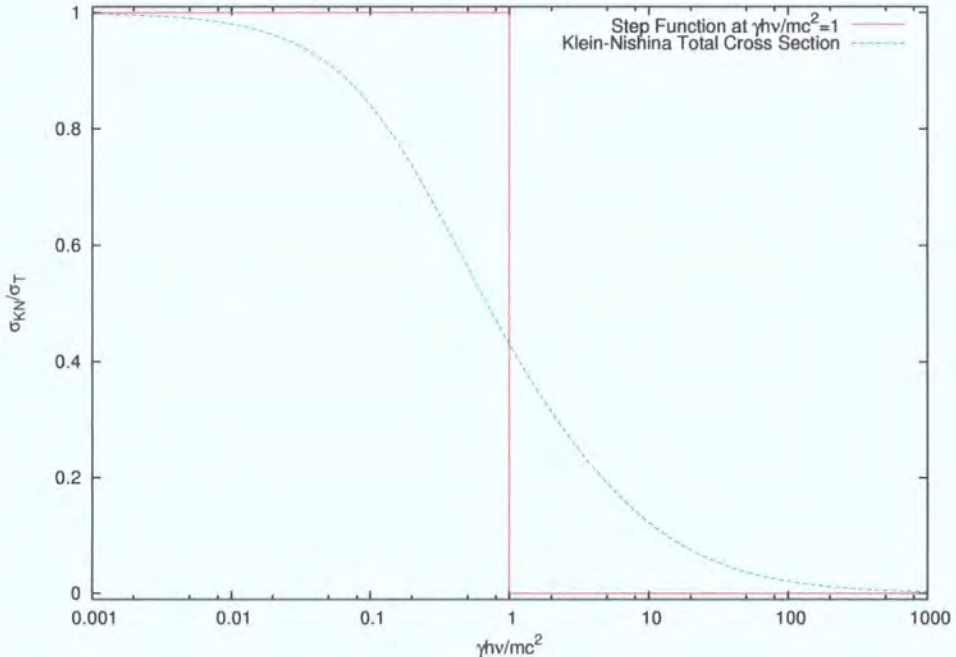


Figure 2.4: Approximation used for the Klein-Nishina cross section.

its simplicity in the code and secondly because it is consistent with the step function used by [39][40]. This does of course exclude interactions between electrons and very high energy incident photons but as previously discussed these photons can only be upscattered by a maximum factor of γ as opposed to γ^2 for lower energy photons and so their exclusion has negligible consequences.

The approximation is represented in Fig(2.4), giving rise to a Klein-Nishina cut-off frequency, ν_k given by,

$$\nu_k = \frac{m_e c^2}{h \gamma_{max}(R_0)} \delta(1, \theta) \quad (2.58)$$

All photons below this frequency, i.e. $\gamma_{max}(R_0)h\nu/m_e c^2 < 1$, undergo Thomson scattering, the final energy of the scattered photon of energy E being $\gamma^2 E$. All those above remain unscattered and do not contribute to the inverse Compton spectrum. Additionally, since the emphasis of this study is the high energy range, ν_k is calculated using $\gamma_{max}(R_0)$ providing better accuracy from this approximation at the higher frequencies at the expense of less accurate fluxes at longer wavelengths.

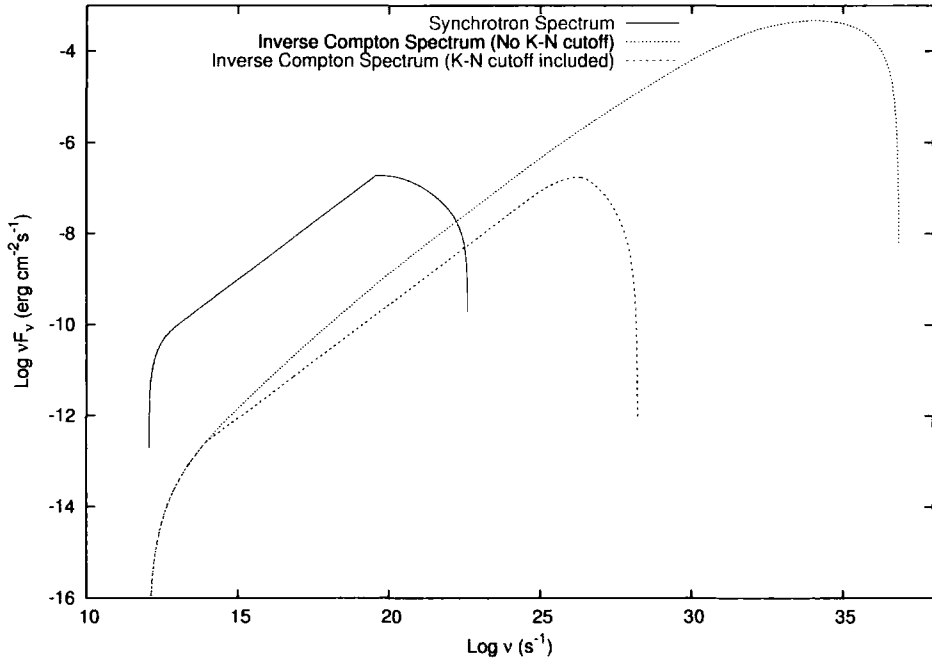


Figure 2.5: Effect on the inverse Compton spectrum using a Klein-Nishina cut-off frequency described by Eq.(2.58)

As a result of this approximation Eq(2.57) can be rewritten,

$$\nu_{ic}(max) = \min\{\nu_{max}^s(R_0)\gamma_{max}^2(R_0), \nu_k\gamma_{max}^2(R_0)\} \quad (2.59)$$

Likewise the smallest synchrotron frequencies are produced at the end of the jet, $\nu_{abs}^s(R_{max})\delta(x_{max}, \theta)$, and so the smallest inverse Compton frequency produced is given by,

$$\nu_{ic}(min) = \nu_{abs}^s(R_{max})\delta(x_{max}, \theta) \quad (2.60)$$

Klein-Nishina effects will not change this unless the local Lorentz factors are unphysically large. Hence the inverse Compton luminosity is calculated between the frequencies $\nu_{ic}(min)$ and $\nu_{ic}(max)$. The graph in Fig.(2.5) is the output of the SSC code showing the effect on the inverse Compton spectrum of including the Klein-Nishina cut off. The parameters used are those for 3C 279 as given in Table(2.1) with the exception that the local Lorentz factor is increased to 10^7 (unphysically large) to make the effect very apparent.

2.6.2 Inverse Compton Integration Limits

The integration in the inverse Compton luminosity is more complicated than for the synchrotron case. Not only do the spatial limits of the jet, which contribute to a given inverse Compton frequency, ν_{ic} , have to be defined, $x_1(\nu)$ and $x_2(\nu)$ respectively, dealt with in this section, but also the extreme frequencies of the synchrotron spectrum which can contribute in that region, $\nu_1(R)$ and $\nu_2(R)$, dealt with in the next section. In the case of [39] the integration limits are set to the minimum and maximum size of the jet. However, a better definition can be obtained by considering the relation between the inverse Compton frequency in question, the frequencies that can contribute, given an approximation for the Klein-Nishina cross section, and the synchrotron frequencies produced in that part of the jet.

For the lower integration limit $x_1(\nu)$ this is trivial. Using Eq.(2.59) to define $\nu_{ic}(max)$ and Eq.(2.60) to define $\nu_{ic}(min)$, if,

$$\nu_{ic}(max) \geq \nu_{ic} \geq \nu_{abs}^s(R_0)\delta(1, \theta) \quad \text{then} \quad x_1(\nu) = 1 \quad (2.61)$$

At lower ν_{ic} frequencies where,

$$\nu_{abs}^s(R_0)\delta(1, \theta) > \nu_{ic} \geq \nu_{ic}(min) \quad (2.62)$$

then,

$$x_1(\nu) = \text{the position in the jet, } x, \text{ where } \nu_{ic} = \nu_{abs}^s(x)\delta(x, \theta) \quad (2.63)$$

The upper limit of the integration however is not as trivial since we are now seeking to find the point in the jet where the lowest synchrotron frequencies that can contribute to a given ν_{ic} lie. Probably the easiest way to explore this is to first look at the conditions needed for the upper limit, $x_2(\nu)$, to be at the end of the jet i.e. x_{max} . Initially ignoring the Klein-Nishina cut-off frequency, if,

$$\frac{\nu_{ic}}{\gamma_{max}^2(x_{max})} \leq \nu_{max}^s(x_{max})\delta(x_{max}, \theta) \quad \text{then} \quad x_2(\nu) = x_{max} \quad (2.64)$$

This can be illustrated by a line diagram representing the frequencies existing along the jet, Fig.(2.6). This kind of diagram is useful for explaining how the

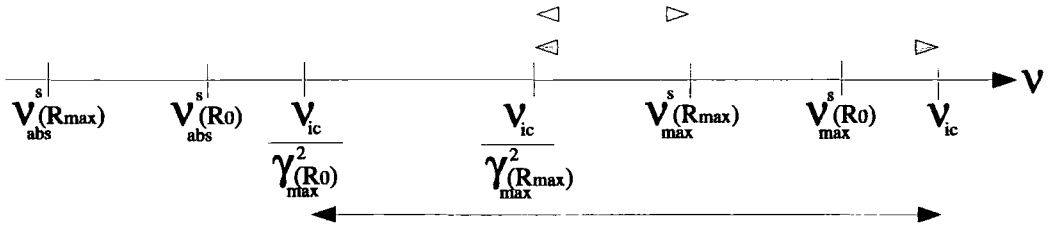


Figure 2.6: Frequency Line Diagram

integration limits change depending on the ν_{ic} being considered and will be repeated for various scenarios henceforth. In Fig.(2.6) the red arrow shows the frequencies that could contribute to ν_{ic} at the end of the jet, the blue arrows representing those that can contribute at the base of the jet. In fact since not all these frequencies are produced by the synchrotron process, only those frequencies up to $\nu_{max}^s(R_{max})$, represented by the green arrow, contribute and in this case since there is some contribution at the end of the jet, the upper limit is x_{max} .

We now have to consider how this is affected by the inclusion of ν_k . There are

three regimes that need to be explored,

- $\frac{\nu_{ic}}{\gamma_{max}^2(xmax)} \leq \nu_{max}^s(xmax)\delta(xmax, \theta) \leq \nu_k$

This has no effect on the original scenario depicted in Fig.(2.6) - $x_2(\nu)$ is still $xmax$ and the contributing frequencies remain the same.

- $\frac{\nu_{ic}}{\gamma_{max}^2(xmax)} \leq \nu_k \leq \nu_{max}^s(xmax)\delta(xmax, \theta)$

This scenario is represented in Fig.(2.7). There is still a small range of frequencies at the end of the jet that can contribute to ν_{ic} , so $x_2(\nu)$ is still $xmax$ but now the contributing frequencies have changed as indicated by the green arrows

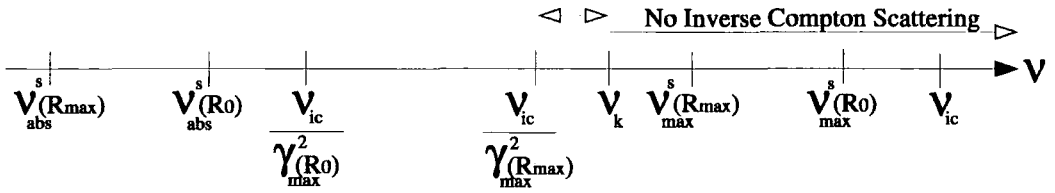


Figure 2.7: Figure 2.6 with $\frac{\nu_{ic}}{\gamma_{max}^2(xmax)} \leq \nu_k \leq \nu_{max}^s(xmax)\delta(xmax, \theta)$

- $\nu_k < \frac{\nu_{ic}}{\gamma_{max}^2(Rmax)}$

In this case the Klein-Nishina cut-off frequency is less than $\frac{\nu_{ic}}{\gamma_{max}^2(Rmax)}$ as represented in Fig.(2.8). Now the synchrotron frequencies at the end of the jet, represented by the green arrows in Fig.(2.6), can no longer contribute to ν_{ic} since they are all above the Klein-Nishina cut-off frequency and are not scattered. The upper limit, $x_2(\nu)$, in this case therefore is

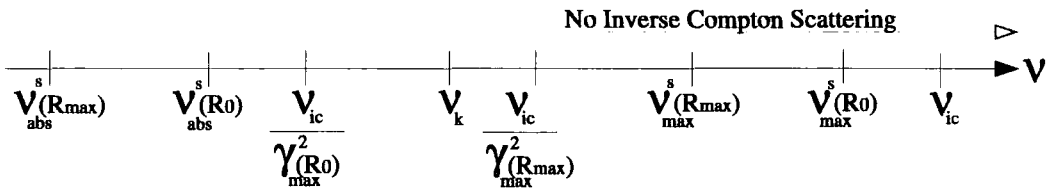


Figure 2.8: Figure 2.6 with $\nu_k < \frac{\nu_{ic}}{\gamma_{max}^2(Rmax)}$

no longer x_{max} but the value of x where,

$$\frac{\nu_{ic}}{\gamma_{max}^2(x)} = \nu_k \quad (2.65)$$

This can be solved analytically using Eq.(2.5) giving,

$$x_2(\nu) = \left[\frac{\nu_k \gamma_{max}^2(R_0)}{\nu_{ic}} \right]^{\frac{1}{2ee}} \quad (2.66)$$

and the contributing frequencies change accordingly.

So far only the case where $\frac{\nu_{ic}}{\gamma_{max}^2(x_{max})} \leq \nu_{max}^s(x_{max})\delta(x_{max}, \theta)$ has been discussed. At higher values of ν_{ic} this condition no longer holds and $x_2(\nu)$ has to be redefined. As before we initially ignore ν_k to define a value of $x_2(\nu)$ and then reintroduce it and reassess. Again looking at the frequency line diagram to represent the case where $\frac{\nu_{ic}}{\gamma_{max}^2(x_{max})} > \nu_{max}^s(x_{max})\delta(x_{max}, \theta)$, Fig.(2.9), it

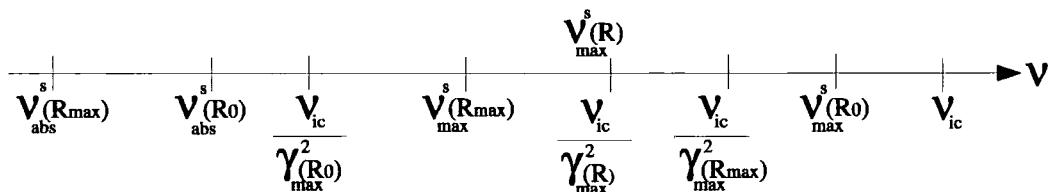


Figure 2.9: Frequency Line Diagram for $\frac{\nu_{ic}}{\gamma_{max}^2(x_{max})} > \nu_{max}^s(x_{max})\delta(x_{max}, \theta)$

is obvious that there are now no synchrotron frequencies at the end of the jet that can contribute to ν_{ic} . Hence $x_2(\nu)$ can no longer be x_{max} . The red ellipse contains two frequencies. The top frequency is $\nu_{max}^s\delta(x, \theta)$, which is the maximum synchrotron frequency at some point x between $x = 1$ and $x = x_{max}$ along the jet. Where this frequency coincides with $\frac{\nu_{ic}}{\gamma_{max}^2(x)}$, the lower frequency in the red ellipse, is the upper limit $x_2(\nu)$ i.e. where,

$$\frac{\nu_{ic}}{\gamma_{max}^2(x)} = \nu_{max}^s(x)\delta(x, \theta) \quad \text{then} \quad x = x_2(\nu) \quad (2.67)$$

Once $x_2(\nu)$ has been calculated then $\nu_{max}^s(x_2)\delta(x_2, \theta)$ can be calculated, using Eqs.(2.38) and (2.48). We now need to look at how the introduction of ν_k will

affect this upper limit. There are two scenarios.

- The first is simple and is the case where $\nu_k \geq \nu_{max}^s(x_2)\delta(x_2, \theta)$. This has no effect on the original calculations and $x_2(\nu)$ remains as given by Eq.(2.67)
- The second scenario is less simple and is the case where $\nu_k < \nu_{max}^s(x_2)\delta(x_2, \theta)$. The position x_2 is no longer valid as all the frequencies produced at that part of the jet are not scattered at all as in Fig.(2.10). A new value for

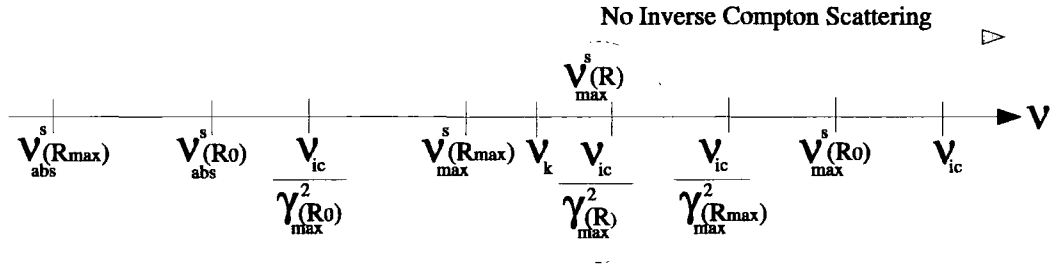


Figure 2.10: Frequency Line Diagram for $\frac{\nu_{ic}}{\gamma_{max}^2(x_{max})} > \nu_{max}^s(x_{max})\delta(x_{max}, \theta)$

$x_2(\nu)$ now has to be calculated using Eq.(2.65), which will be closer to the base of the jet than first calculated.

2.6.3 Contributing Frequencies to ν_{ic}

Now that the integration limits for a given ν_{ic} are defined, the upper and lower frequencies, $\nu_1(R)$ and $\nu_2(R)$, that contribute over that range also have to be defined. This is made somewhat easier by the method of numerical integration. As with the integration for the synchrotron luminosity function, the code uses a Romberg integration method. This involves calculating the value of the integrand at specific values of x . As a result, the upper and lower contributing frequencies to ν_{ic} from the synchrotron spectrum never have to be calculated for a continuous region, which would be inherently difficult. In the case of [39] the contributing frequencies are approximated by the minimum and maximum synchrotron frequencies for that particular value of x i.e. $\nu_{abs}^s(R)\delta(x, \theta)$ and

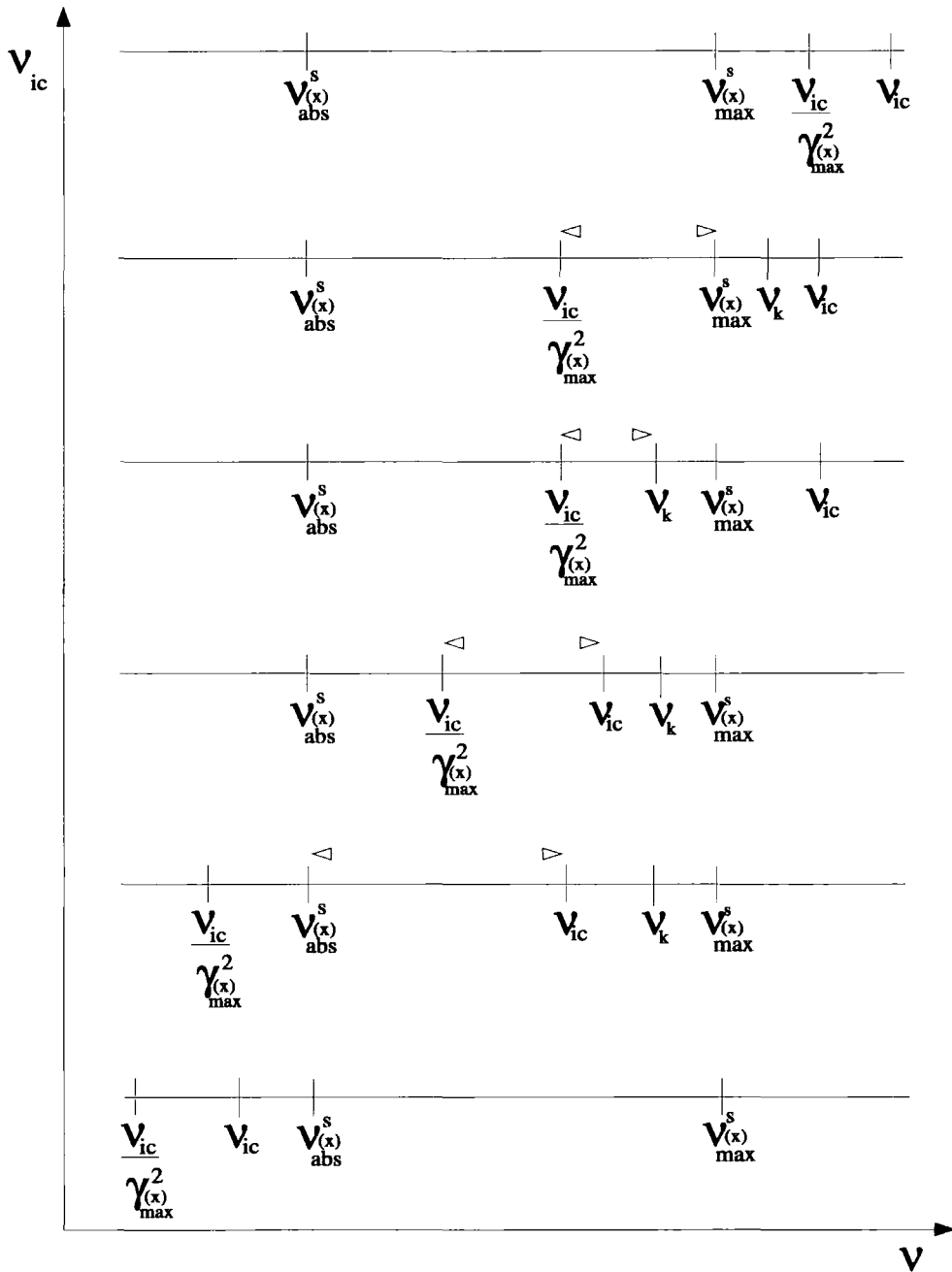
$\nu_{max}^s(R)\delta(x, \theta)$. This is not always the case and if used would include frequencies that were unable to contribute either because they lie above ν_k or below $\frac{\nu_{ic}}{\gamma_{max}^2(x)}$. $\nu_1(R)$ can therefore be defined as,

$$\nu_1(R) = \max\{\nu_{abs}^s(x)\delta(x, \theta), \frac{\nu_{ic}}{\gamma_{max}^2(x)}\} \quad (2.68)$$

and $\nu_2(R)$ can be defined as,

$$\nu_2(R) = \min\{\nu_{max}^s(x)\delta(x, \theta), \nu_k, \nu_{ic}\} \quad (2.69)$$

The method of choosing the contributing frequencies for a given position, x , in the jet is illustrated in Fig.(2.11), showing some frequency configuration examples, with the contributing range of frequencies being represented by the green arrows. Where there are no green arrows there are no photons that can be scattered from that part of the jet and that position would not be contained within the integration limits.

Figure 2.11: Selection of $\nu_1(R)$ and $\nu_2(R)$.

2.7 Code Test - 3C 279

3C 279 is a well studied blazar, an AGN whose jets are aligned with the observer's line of sight, which lies in the constellation Virgo at a distance $z = 0.538$. It was the first quasar in which apparent superluminal motion was observed [111]. It has proved to be a violently variable object and has been detected by EGRET aboard the Compton Gamma Ray Observatory in the energy range 30MeV to 5GeV ([51] and references therein). 3C 279 is the object

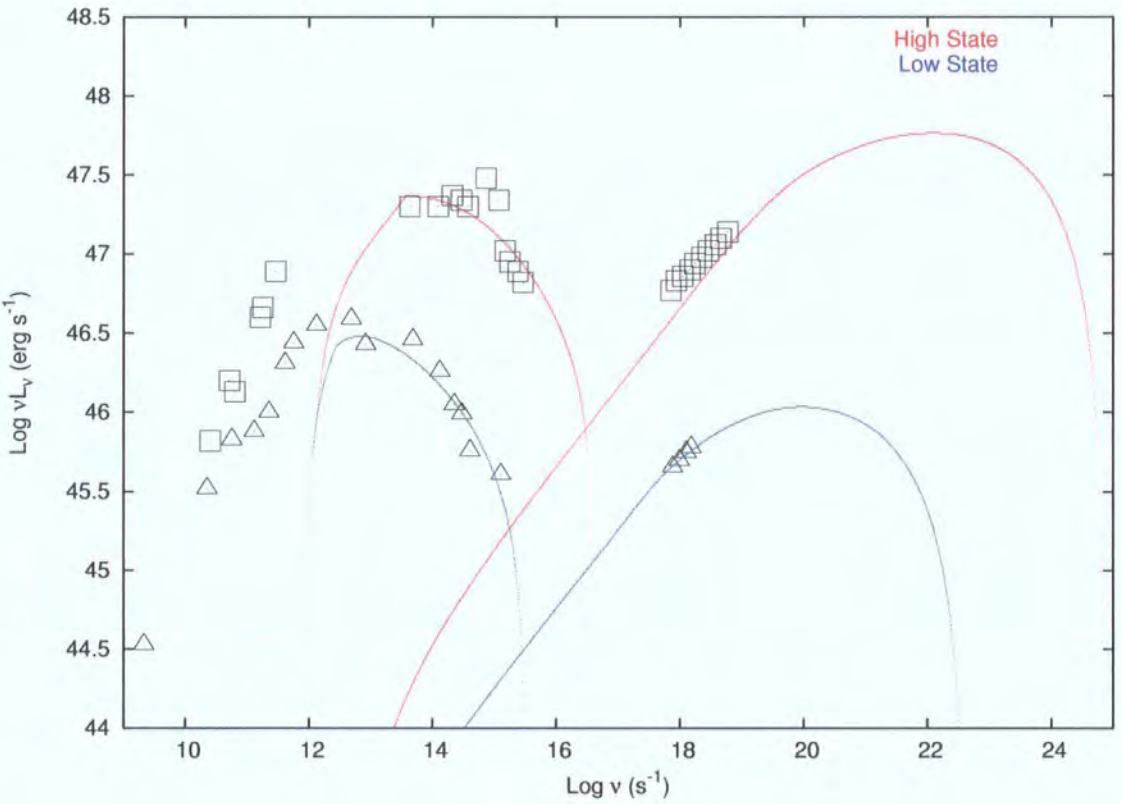


Figure 2.12: Synchrotron Self-Compton Model Applied to AGN 3C 279:- The parameters used for the high and low state spectrum are the same as in [78] and are given at the end of this section. Again this is done to provide a direct comparison between two independent codes describing the same model.

selected to test the code, since the model was originally designed for AGN jets, and 3C 279 is such a well studied blazar. More importantly, 3C 279 is one of the objects for which there is published use of this particular model [78] and so

is useful for direct comparison of the output of two independent codes. Figure Fig.(2.12) shows the synchrotron spectrum obtained for 3C 279 using this code. The data points are adapted directly from [78], and Fig.(2.13) is that obtained by [78]. Direct comparison of the two spectra shows the synchrotron element

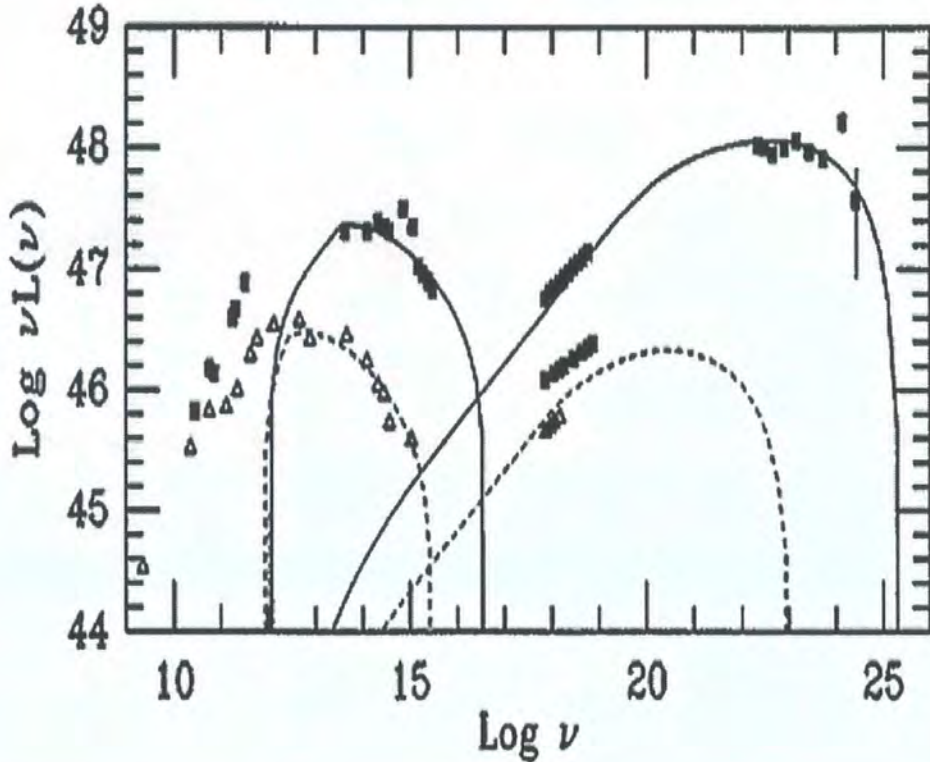


Figure 2.13: Spectrum of 3C 279 taken from [78]:- The solid lines represent the high state spectrum and the dotted lines the low state spectrum

to be almost identical. There is an equally good fit to both the high and low data sets using both codes and the overall shape and frequency range match very closely. However, the inverse Compton spectrum does differ somewhat and this was to be expected, since the contributing synchrotron frequencies to the inverse Compton process differ between this work and [40]. This difference will be addressed in a later section. The parameters used for this test are those given in [78] and are laid out in Table(2.1).

Parameter	Common to High State and Low State	
ϵ	0.5	
R_0	2×10^{15} cm	
R_{max}	4×10^{18} cm	
r_0	2×10^{15} cm	
B_0	8G	
m	1	
n	1.5	
e	0.5	
η	1	
Γ	5.5 at R_0 to ~ 25 at R_{max} ($g = 0.2$)	
$d = \frac{cz}{H_0}$	3225Mpc with $H_0 = 50\text{km s}^{-1}\text{Mpc}^{-1}$	
	High State	Low State
$\nu_{max}^s(R_0)$	4×10^{15} Hz	3×10^{14} Hz
$\gamma_{max}(R_0)$	1.3365×10^4	3.66×10^3
τ_0	2×10^3	1×10^3
K_0	1.5×10^6	7.5×10^5

Table 2.1: Parameters Used in the Code as Applied to 3C 279. Values for $\gamma_{max}(R_0)$ are calculated using equation Eq.(2.37). Values for K_0 are calculated using equation Eq.(2.8). The local synchrotron spectrum is assumed to have a power law of 0.5 and is the same throughout the jet. The integrated spectrum from the whole jet varying due only to the difference in the local values of ν_{abs}^s and ν_{max}^s .

The code produced for this work seems to give a better fit to the low state inverse Compton data than [78]. The fits to the high state data appear equally good in both works. It is worth noting that [78] also attempts to fit the high state inverse Compton spectrum to EGRET data points, whereas this work does not. The EGRET data are not contemporaneous with the other data sets, and there are no simultaneous data at lower frequencies to support the EGRET data, to allow the fit at other wavelengths. A second point worth noting is the lack of any fit to data at the frequencies lower than 10^{12} Hz. This again is to be expected, as this work is concerned with predicting gamma ray emission and only takes into account the inner part of the jet where electron energies are at the highest. To fit the low frequency data points would require extra code which includes the outer part of the jet where acceleration is no

longer present and where the jet shape becomes a truncated cone with $\epsilon = 1$. Here the electrons have much lower energies than at the base of the jet and would be responsible for the radio synchrotron emission. To upscatter these photons to gamma ray frequencies would require unphysically large electron local Lorentz factors at the source of production and so they are not relevant to this discussion.

An interesting point to note is how sensitive the spectrum is to each free parameter in the fit of the model to 3C 279. To examine this the parameters K_0 , $\gamma_{max}(R_0)$ and B_0 are all decreased individually by a factor of 2 (the values of $\nu_{max}^s(R_0)$ and τ_0 are directly affected by changing the values of K_0 and $\gamma_{max}(R_0)$ respectively so are not changed independently. Also, strictly speaking, B_0 is not a free parameter in this case, nevertheless its affects are interesting). Figure 2.14 shows the results. It can be seen that the most dom-

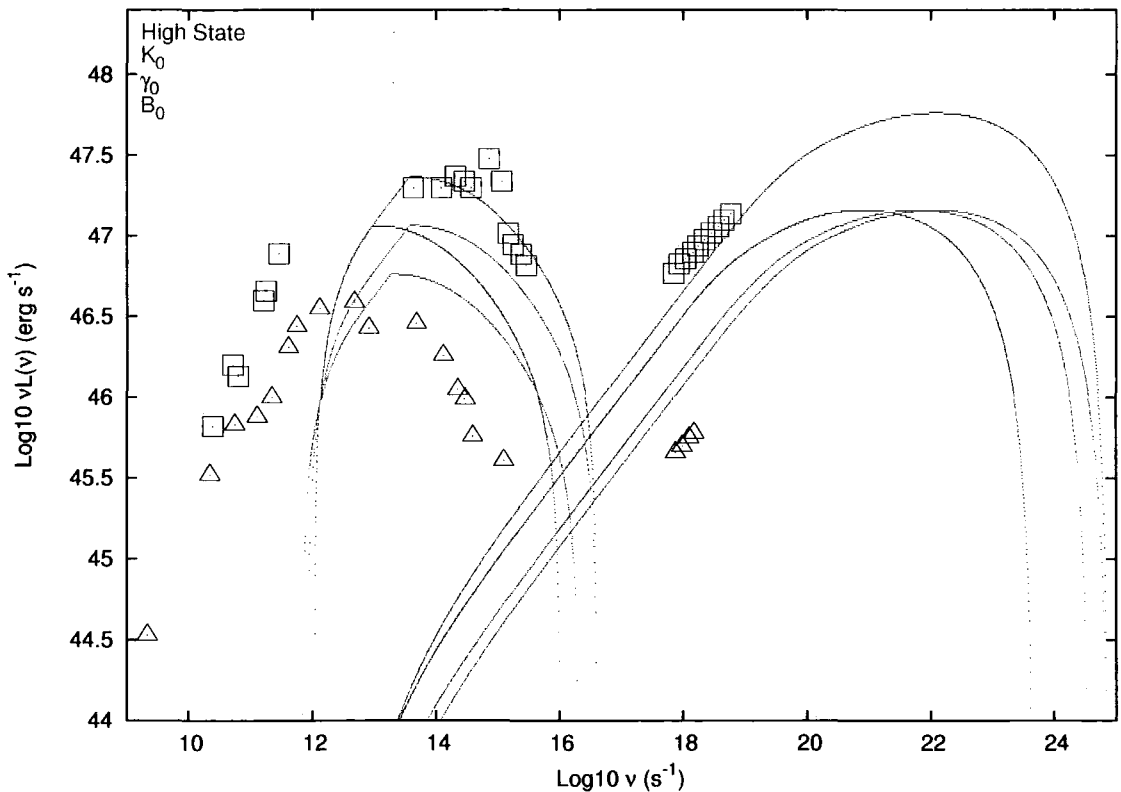


Figure 2.14: Effect on SSC spectrum of varying model parameters individually by a factor of 2

inant parameter affecting the upper energy cut-off and position of the peak inverse Compton energy, is the local lorentz factor, $\gamma_{max}(R_0)$. The particle density, K_0 , and the associated electron optical depth, τ_0 , seem to have little affect here. This is to be expected as the maximum inverse Compton frequency is related to the maximum synchrotron frequency, which in turn is governed by $\gamma_{max}^2(R_0)$. In contrast, in the UV part of the spectrum the dominant factors are the particle density, K_0 and the magnetic field, B_0 with the local lorentz factor being less sensitive. At lower frequencies the position of the peak energy in the synchrotron spectrum is affected very little by K_0 , there is simply less flux. The major energy peak shift is again due the sensitivity of $\gamma_{max}(R_0)$ and to some degree B_0 . However the flux is most sensitive here to B_0 . We can see therefore what factors are going to affect the production of detectable VHE γ -rays. The synchrotron flux is highly dependant on K_0 , $\gamma_{max}(R_0)$ and B_0 , whereas at the high energy cut-off of the inverse Compton spectrum, the local lorentz factor is the dominant variable. To push the high energy cut-off in the inverse Compton spectrum to TeV energies will require a large local lorentz factor coupled with a high density particle field and large magnetic field. The problem will arise if the peak energy of the synchrotron emission approaches the energy of the electrons since Klein-Nishina effects will quench the high energy emission and the flux will be too low for detection.

2.8 Application to Microquasars

2.8.1 Introduction

The code is applied to three black hole x-ray binaries; GRS 1915+105, V4641 Sgr and GX 339-4, which are detailed in the following sections. These microquasars were observed with the H.E.S.S. array, the results of which are presented in Chapter 3, together with the results of data taken on the microquasar Circinus X-1.

Circinus X-1 is not included in this section, since the method of parameterisation described here depends primarily on the scaling of black hole masses. Since Circinus X-1 has a neutron star as the compact object, although still displaying relativistic jets, a direct comparison with AGN, on scaling arguments, cannot be made and so are not relevant in this thesis. This of course does not preclude the use of the SSC code to neutron star microquasars. The code can of course be applied to any source displaying collimated jets of relativistic particles and possessing a magnetic field, but the parameters would be chosen by some other means, such as observational data. This will be investigated in the future.

GRS 1915+105

GRS 1915+105 was discovered on August 15 1992 by the WATCH all sky monitor instrument aboard the Russian x-ray satellite, GRANAT [20]. It was the first galactic source where superluminal motions were observed by Mirabel and Rodríguez [81], who derived a distance of 12.5 ± 1.5 kpc, based on the absorption of 21cm atomic Hydrogen. This distance was later confirmed with millimeter observations [25] and again later revised to an upper limit of 11.2kpc using radio observations [32]. Mirabel and Rodríguez [81] also derived a jet alignment of $70 \pm 2^\circ$ using equation Eq.(1.30) with a true jet speed of $0.92 \pm 0.08c$ using equation Eq.(1.29). In 2001 the companion star was identified as a K-M III giant using infrared spectroscopic analysis [47], classifying GRS 1915+105 as a low mass x-ray binary. The mass of the black hole was determined to be $14 \pm 4M_\odot$ [46] from an orbital period of 33.5 days

and mass function measurements [46].

GRS 1915+105 is a highly variable object, the complex patterns of which seem unique among microquasars. The complete classification of the light curves from the first two years observation with the Rossi X-ray Timing Explorer (RXTE) was presented by [13], who divided them into twelve separate classes on the basis of timing and hardness. These classes later increased to thirteen [65] and then possibly fourteen [50] demonstrating the complexity of the object. However, it was found by [13] that the flux and spectral variability could be interpreted as the transition between three separate states defined separately from the canonical spectral states discussed in section 1.6.6 [33].

- State A: in this state the spectrum is soft and is dominated by a thermal disc component with $kT_{in} > 1$ keV, where T_{in} is the temperature in the inner accretion disk. There is little time variability.
- State B: this state has a softer spectrum dominated by the thermal disc component with a larger temperature than in state A.
- State C: this state is dominated by a harder spectrum with a power law, $\Gamma = 1.8 - 2.5$.

Variability on timescales > 1 sec are seen in both state B and state C. Observations show that transitions occur between all states except from state C to state B. In terms of the canonical x-ray binary spectral states, discussed in section 1.6.6, state C (sometimes called the ‘plateau’ state) is comparable to the LS with prolonged hard x-ray emission and steady, low power, self-absorbed jets. States A and B are comparable to the soft x-ray states, HS and SIMS. The transition from state C to state A produces the high power, optically thin ejection events that are seen in the transition from HIMS to SIMS. A comprehensive review of the observational properties of GRS 1915+105 can be found in [33].

GX 339-4

GX 339-4 is a low mass x-ray binary discovered by the OSO-7 satellite in 1973 [79] and was classified as a black hole binary mainly because it followed the

emission pattern of a canonical black hole system, and undergoes rapid x-ray and optical variability, see e.g. [77]. The basic system parameters remained in dispute for some time because, even in quiescence, the x-ray luminosity is too bright to detect the companion star. In 2003 an alternative to spectroscopic and photometric techniques was used to derive a mass function of $5.8 \pm 0.5 M_{\odot}$ with an orbital period of ~ 1.7 days, confirming its black hole status [59]. Although the distance to the object is not known, observations place it at > 6 kpc [60] and [112].

GX 339-4 was the first black hole x-ray binary to show a positive correlation between radio and x-ray emission in the LS [48], making it an important object in the understanding of the relation between jets and accretion. Between 1999 and 2002 GX 339-4 remained in a state of quiescence before rebrightening in the x-rays and displaying a large scale relativistic radio jet that seems to follow the state transition model, described in section 1.6.6, closely [12].

V4641 Sgr.

V4641 Sgr, a high-mass x-ray binary, is probably one of the most attractive objects for γ -ray observations because of its massive outburst of over 12 crab in x-rays in September 1999, and its possible classification as a microblazar. It was first discovered¹ using Beppo Sax [61] and designated SAX J1819.3-2525, peaking to 80 mcrab in the 2-10 keV range over a 1 hour 40 min observation on February 20 1999. It subsequently faded to less than the Beppo Sax upper limit of 10 mcrab thereafter. At this time, and for short time after, the variable star GM Sgr was mistakenly proposed as the optical counterpart.

No further outbursts of this object were recorded until August 1999 when very bright optical outbursts were reported [104]. The visual magnitude increased from 12.3 to 8.8 over a period of 4 days and showed strong variability [104]

¹In 1978 Goranskij [44] discovered the outburst of a star in the same region of sky as the long period variable star, GM Sgr, at about two magnitudes brighter than normal. The accurate position for this star was given as $18^{\text{h}}16^{\text{s}}16^{\text{s}}.2, -25^{\circ}25'43''$, 1950.0. GM Sgr was discovered and classified in 1927 by Luyten [68] at position $18^{\text{h}}16^{\text{s}}17^{\text{s}}, -25^{\circ}26'48''$, 1950.0. Despite distinct differences between the classifications, descriptions and positions, the star was misidentified, by Kholopov [45], with GM Sgr. It is quite likely that this was the first discovery of V4641 Sgr.

and [84]. In a response to this report, the object, still being associated with GM Sgr, was monitored with the All Sky Monitor (ASM) aboard RXTE [102]. On September 15 1999 UT, ASM recorded an intensity of 1.55 ± 0.04 crab in the 2-12 keV energy range. Monitoring showed a rapid increase in x-ray flux up to 12.2 crab in less than 7 hours, with a spectrum harder than the crab. Other observations using the Burst And Transient Source Experiment (BATSE) recorded fluxes up to 8 crab in the 20-100 keV band [87] and the RXTE PCA recording a photon index of 0.9 during the flare [80]. Measurements with the Gemini telescope showed properties characteristic of a low-mass x-ray binary [24]. In October 1999 the misidentification of the object as GM Sgr. was announced and the object was designated V4641 Sgr. [100], both objects evidently being visible on the 1897 photographic plate of the region, that was used by Luyten.

Further outbursts occurred in July 2000 when radio emission was detected [55]. In August 2003 an outburst was again detected at radio [98] [99], optical [18], and x-rays [8], observations showing high variability and a hard spectrum of 0.6 [99] and again in July 2004, e.g. [103]. In neither case was the outburst anywhere near as strong as in September 1999.

2.8.2 Scale-Invariant Jets

In order to test the hypothesis that microquasar jets are scaled down versions of AGN jets, the jet parameters used in each example are based on simple scaling rules defined in [52]. All distances relating to the jet are scaled according to the fundamental length scale of a black hole, the Schwarzschild radius, $r_s \propto M_{BH}$. For the parameters used in the fit to 3C 279 discussed in section 2.7, the distance to the base of the jet, $R_0 = 2 \times 10^{15}$ cm, is assumed to be the last stable orbit, r_{LSO} of a supermassive black hole. Using,

$$r_{LSO} = 3r_s = \frac{6GM}{c^2} \quad (2.70)$$

where G is the gravitational constant and M_{BH} is the mass of the black hole, gives the M_{BH} for 3C 279 as $2.25 \times 10^9 M_\odot$, which is within the the distribution of central black hole masses in γ -ray blazars [113]. The distances to the microquasars in question are taken from Table 1.1 as are the angles of the jet to the line of sight, θ .

The magnetic field at the base of the jet, B_0 , is assumed to be some fraction of the Eddington magnetic field strength B_{Edd} , given by [63],

$$B_{Edd} = \left(\frac{2L_{Edd}}{r_s^2} \right)^{-\frac{1}{2}} \simeq 6 \times 10^4 \left(\frac{M_{BH}}{10^8 M_\odot} \right)^{-\frac{1}{2}} \text{ G} \quad (2.71)$$

In the case of 3C 279 $B_0 = 6.32 \times 10^{-4} \cdot B_{Edd}$. For the case of microquasars the same fraction of the Eddington magnetic field strength is used. This is equivalent to the scaling of the magnetic field detailed in [52] and references therein, where,

$$B_0 \propto M_{BH}^{-\frac{1}{2}} \quad (2.72)$$

In addition the particle density at the base of the jet, K_0 , also follows the relation given in [52],

$$K_0 \propto M_{BH}^{-1} \quad (2.73)$$

Table 2.2 lists the the parameters used to produce the spectral energy distributions (SEDs) based on these scalings. The SEDs are produced by applying

the scaling rules to the parameters used to fit the model to 3C 279 (section 2.7), unless otherwise stated. The bulk Lorentz factor Γ , is not scaled with M_{BH} but is set to 1 at the base of the jet and to a maximum value at the end of the jet calculated using the intrinsic velocity of the jet given in Table 1.1. The power laws for the magnetic field and electron density along the jet are set to $n = 2$ and $m = 1$. The distance to the object and the angle of the jet to the line of sight, θ , are also taken from Table 1.1.

Figures 2.15, 2.16 and 2.17 show the results of applying the code to GRS 1915+105, V4641 Sgr and GX 339-4, using these scale-invariant parameters. Also shown are the H.E.S.S. upper limits derived from the analysis on these objects, detailed in Chapter 3.

Parameter	GRS 1915+105	V4641 Sgr	GX 339-4
M_{BH}	14	9.6	5.8
$R_0(\text{cm})$	1.24×10^7	8.5×10^6	5.15×10^6
$R_{max}(\text{cm})$	2.48×10^{10}	1.7×10^{10}	1.03×10^{10}
$d(\text{kpc})$	12.5	10.0	6.0
$B_0(\text{G})$	101×10^3	122×10^3	158×10^3
$K_0(\text{cm}^{-3})$	2.41×10^{14}	3.52×10^{14}	5.82×10^{14}
Γ_{max}	2.5	10	2.3
$\theta(\text{deg})$	70	5	26
g	0.126	0.303	0.11

Table 2.2: Scale-invariant parameters for GRS 1915+105, V4641 Sgr and GX 339-4. The parameters are based on the scaling rules presented in the text, applied to the parameters used to fit the model to 3C 279 (section 2.7). Assuming equipartition of energy, the power laws governing the magnetic field and particle density along the jet are set at $m = 1$ and $n = 2$. The bulk Lorentz factor Γ , is set to 1 at the base of the jet and to a maximum value at the end of the jet calculated using the intrinsic velocity of the jet given in Table 1.1.

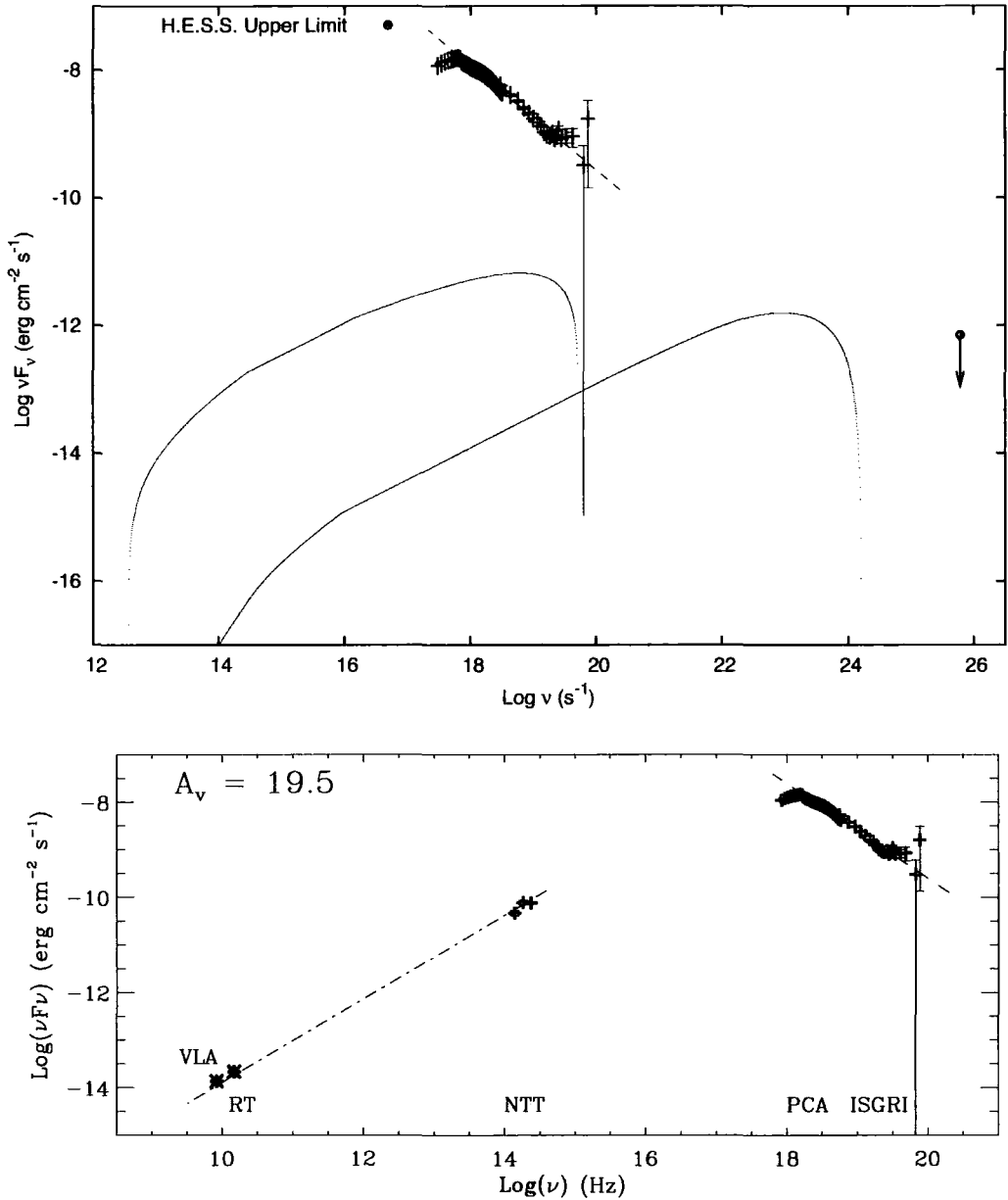


Figure 2.15: Top: results of the SSC model applied to GRS 1915+105 (X-ray data overlaid from below) using scale-invariant parameters listed in Table 1.1, the red and blue lines representing the Synchrotron and Synchrotron Self-Compton spectral energy distributions respectively. The H.E.S.S. upper limit above the average energy threshold of the telescopes, derived from observations described in Chapter 3, is also shown. Bottom: the SED produced by [35] from a multiwavelength campaign during April 2003, during the LS of GRS 1915+105.

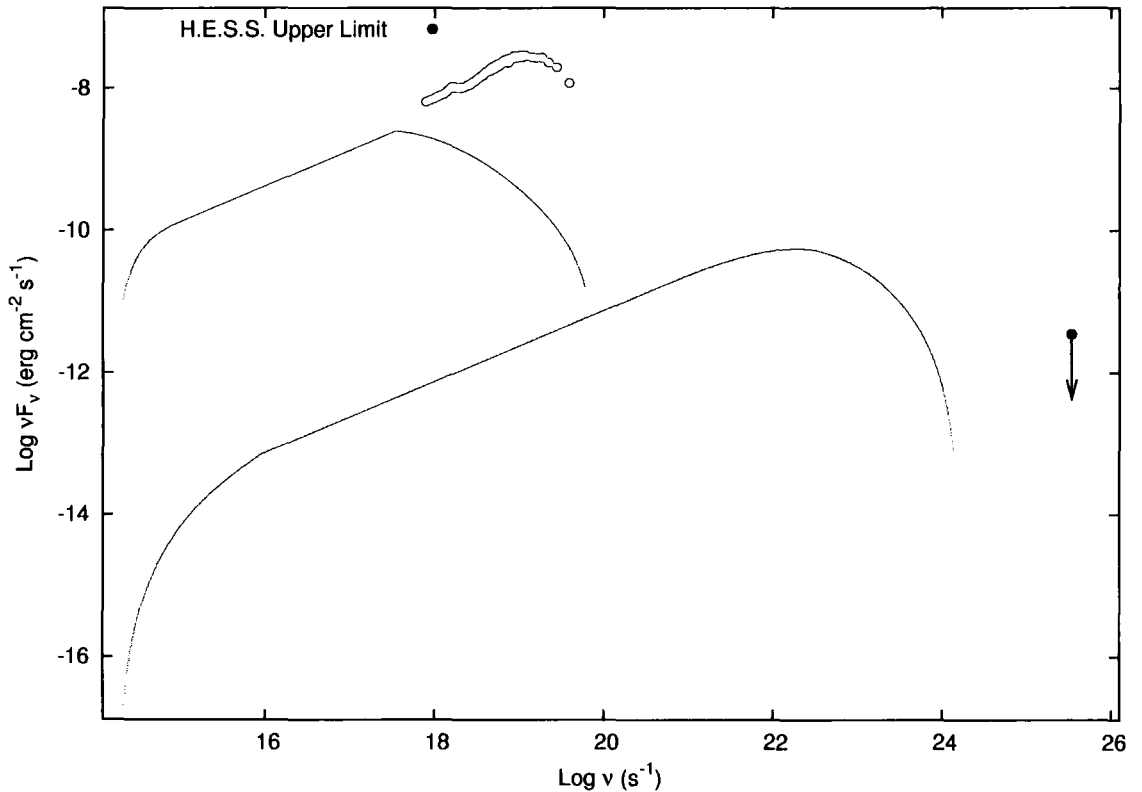


Figure 2.16: Results of the SSC model applied to V4641 Sgr using scale-invariant parameters listed in Table 1.1. The red and blue lines represent the Synchrotron and Synchrotron Self-Compton spectral energy distributions respectively. The H.E.S.S. upper limit above the average energy threshold of the telescopes, derived from observations described in Chapter 3, is shown along with data adapted from [95], taken at the peak of the observed light curve during September 1999 (grey points).

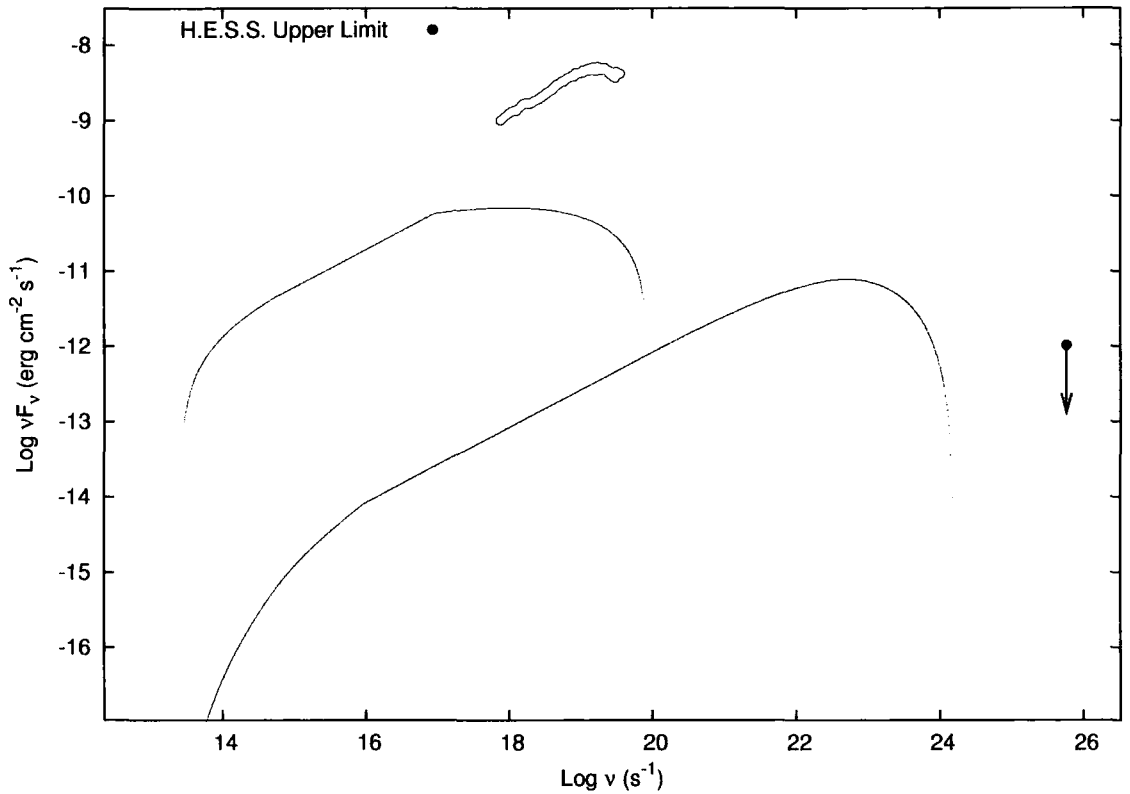


Figure 2.17: Results of the SSC model applied to GX 339-4 using scale-invariant parameters listed in Table 1.1. Again the red and blue lines represent the Synchrotron and Synchrotron Self-Compton spectral energy distributions respectively. The H.E.S.S. upper limit above the average energy threshold of the telescopes, derived from observations described in Chapter 3, is shown along with data adapted from [58] of GX 339-4 in the low, hard state (grey points).

2.8.3 Discussion and Conclusions

It is easy to see from Figs. 2.15, 2.16 and 2.17, that there is a very poor fit between data and the output of the SSC model using the scale-invariant jet approach. There may be several reasons for this;

- Firstly, microquasars are only morphologically similar to AGN and the physics applied to one cannot simply be scaled to fit the other.
- Secondly, as well as being morphologically similar, the physics in microquasars are the same as for AGN, but the methods of scaling outlined here may either simply not apply over such a vast range of black hole masses, or, as is more likely, the scaling is far more involved and may need to include other factors such as black hole spin [52].
- Thirdly, the combination of parameters used to fit 3C 279 are not unique, and there exist other parameters, which may ultimately scale more accurately.
- Finally, synchrotron self-Compton may be the dominant emission process in AGN, hence the good fit of the model to 3C 279. The case may be very different for microquasars where, especially for HMXBs the jets interact more with the external photon field and hence external Comptonisation may be the dominant emission from the jet. Emission from the disk may also be more dominant in microquasars.

As with 3C 279 it is interesting to look at how the parameters of the model need to be changed to achieve a trend that matches the data for microquasars as opposed to AGN. Simply varying all the parameters in an attempt to match the data provides too many permutations as there are many degrees of freedom. Therefore as with 3C 279 the most influential parameters are varied to find the best fit. This process is carried out for GX 339-4 and V4641 Sgr, the results of which can be seen in Figs. 2.18 and 2.19. In the case of GRS 1915+105 it is not considered to be worthwhile to attempt this since the angle of the jet to the observers line of sight is large in comparison to GX 339-4 and V4641 Sgr and so Doppler boosting will have less effect. Also the likely

dominant emission is from the disk and surrounding regions.

It can be seen from Figs. 2.16 and 2.17 that the synchrotron emission in the SSC model is both at too low a flux and peaks at too low a frequency to match the data. From the variation of parameters carried out on 3C 279 it can be seen that the factors that affect this are the magnetic field, B_0 and the local Lorentz factor γ_0 . Varying these two factors and maintaining the other parameters as per the scale-invariant scenario allows the synchrotron output of the model to fit the peak and flux of the data. Unfortunately this is only possible by using unphysical values for the magnetic field, in excess of 10^4 in both cases. In addition to this, to achieve the upper frequency turnover seen in the data for both V4641 Sgr and GX 339-4, one has to impose a very small jet region, of the order of $< 10^2$, again unphysical as the electrons would have to cool or the magnetic field decay inexplicably fast after the end of the jet. It is interesting to note that in both cases the fluorescent iron K_α line at 6.4 keV (equivalent to a frequency of 1.55×10^{18} Hz) is clearly visible in the data, commonly associated with reflection from neutral matter.

The inverse Compton frequency never reaches the H.E.S.S. upper limit as this would require very high local Lorentz factors. The result of increasing the local Lorentz factor too far, however, means that Klein-Nishina effects quench the inverse Compton emission before the upper limit is reached.

In conclusion, the SSC model by itself is a poor fit to the microquasars considered here. This is likely due to the fact that there are probably more dominant emission regions such as the accretion disk, which emits in the X-rays, the corona and in the case of HMXB's the UV emission from the companion star. To improve the model would require the inclusion of emission mechanisms from these regions also. For the inverse-Compton spectrum due to the jet, the contribution of external photon fields is also necessary.

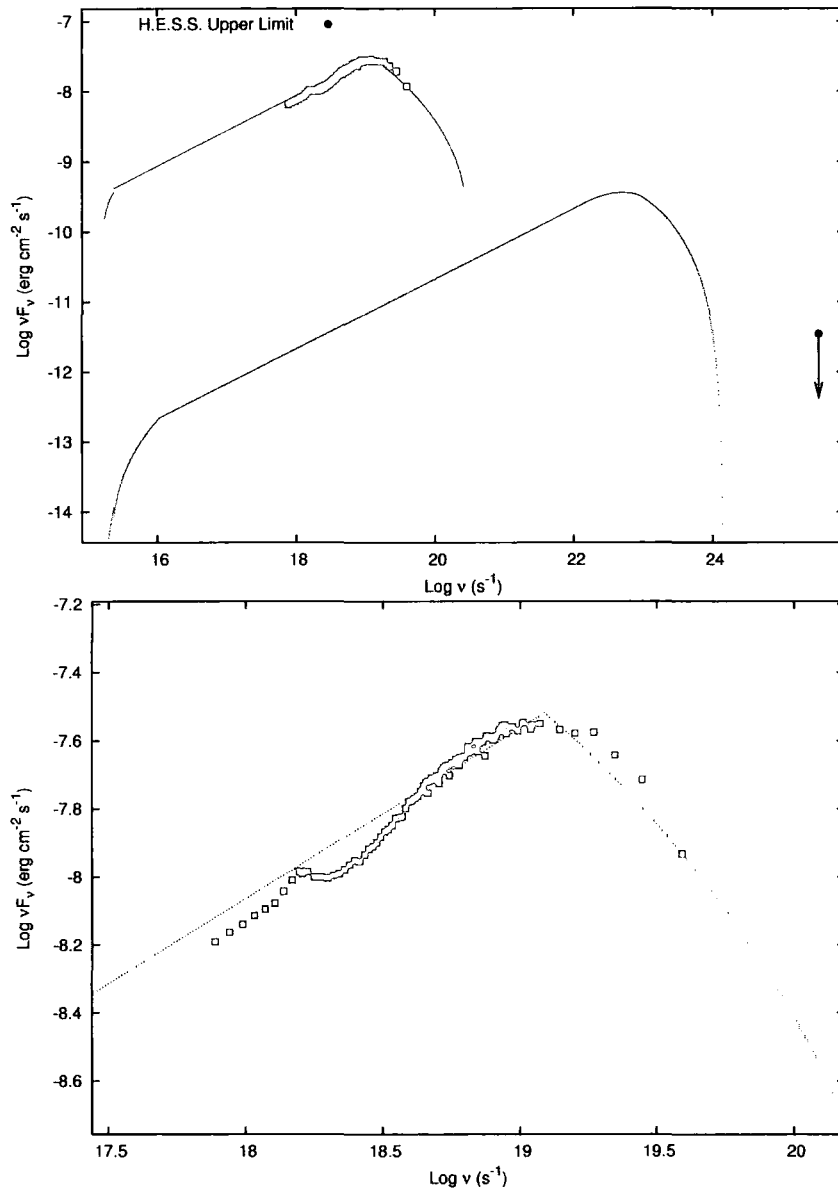


Figure 2.18: Results of the SSC model applied to the V4641 Sgr with different parameters in order to fit the data adapted from [95]. The red and blue lines represent the Synchrotron and Synchrotron Self-Compton spectral energy distributions respectively. A physically unrealistic magnetic field of 70×10^4 G and a short jet of only $170 r_{LSO}$ is necessary to reach the flux levels and turnover seen in the data.

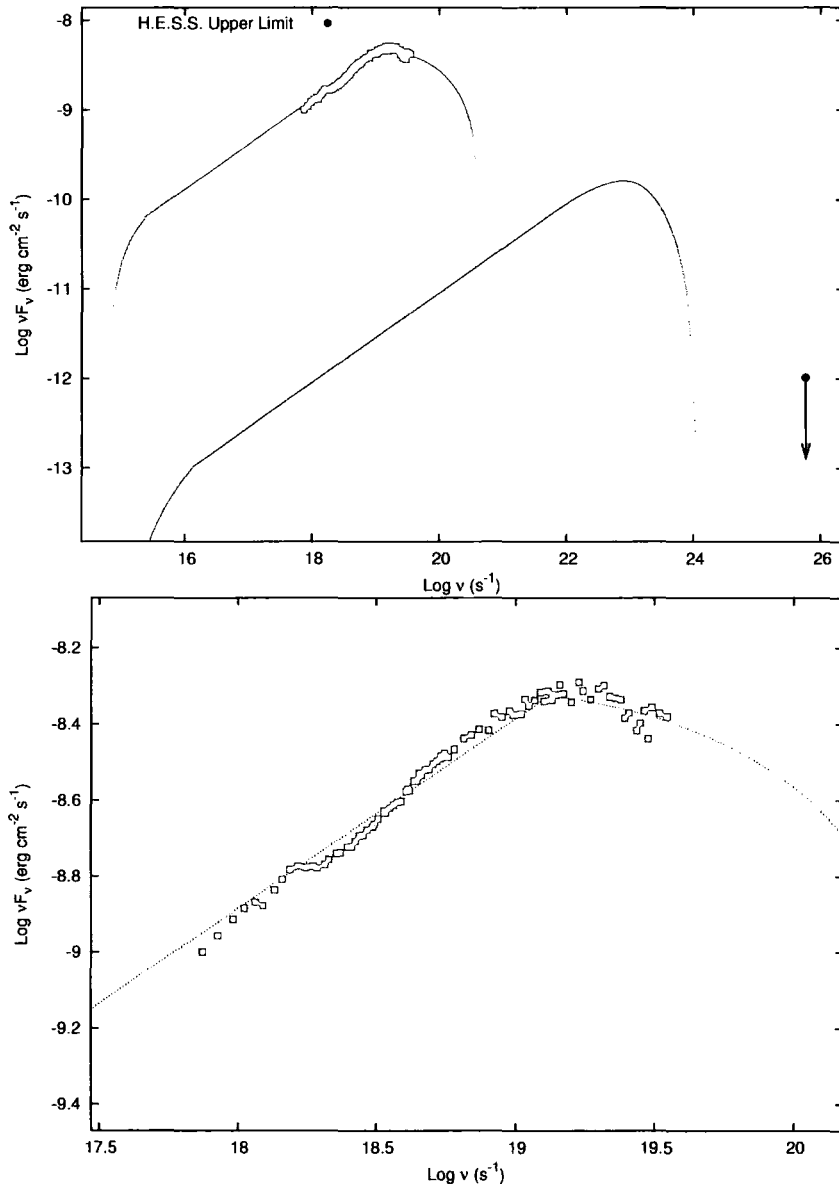


Figure 2.19: Results of the SSC model applied to the GX 339-4 with different parameters in order to fit the data adapted from [58]. The red and blue lines represent the Synchrotron and Synchrotron Self-Compton spectral energy distributions respectively. A physically unrealistic magnetic field of 160×10^4 G and a short jet of only $60r_{LSO}$ is necessary to reach the flux levels and turnover seen in the data.

Chapter 3

H.E.S.S. Data Analysis

3.1 Introduction

Data taken using the completed four telescope array of H.E.S.S. Phase I have been analysed using the H.E.S.S. standard analysis software provided by the Max-Planck-Institut für Kernphysik, Heidelberg, Germany. The H.E.S.S. analysis software suite is constantly being improved and the data presented in this work have been analysed using the latest available software at the time of writing, which uses more refined atmospheric models, provides upper limits, spectra and light curves, unavailable using earlier software versions. Four microquasars were observed by H.E.S.S.: Circinus X-1, GX 339-4, GRS 1915+105 and V4641 Sgr. XRB H1743-322 was also observed during three consecutive nights but all the data were unacceptable for various reasons (bright meteors, bad trigger rates etc.) and so is not included in this discussion. In the following sections the methods for data selection will be described before some important techniques and definitions used for the analysis are outlined. Results from the Crab Nebula are shown as an example of a strong γ -ray source before results for the microquasars are presented. Descriptions of the microquasars are given in Section 2.8 and are not discussed in this chapter. There is no evidence for VHE γ -ray emission from any of these microquasars.

3.2 Data Selection

The data selected for analysis were chosen to satisfy three main criteria.

- Firstly the stability of the atmosphere during the data taking run. As the atmosphere is a critical part of the imaging technique, it is vital that variations in sky temperature and opacity are small. This is easily checked. Each telescope is fitted with a radiometer that senses the temperature of the sky. Any passing of cloud or decrease in sky clarity will be sensed as a change in temperature. A run with a such a detection, as discussed in 3.4.1, is rejected.
- Secondly the trigger rate of the telescope is checked. Again any data run that has variations in trigger rate or has a particularly low trigger rate is rejected. Variations may be due to changes in sky clarity, in which case there would be correlation with the radiometer data, or problems with the telescope hardware.
- Lastly the observation log for each run is checked. Any problems with hardware or software encountered during the run will be logged here. Any runs that have data which could be affected by such problems are rejected.

Figures Fig.(3.1) and Fig.(3.2) show the difference between a bad observation run and a good observation run respectively using these criteria.

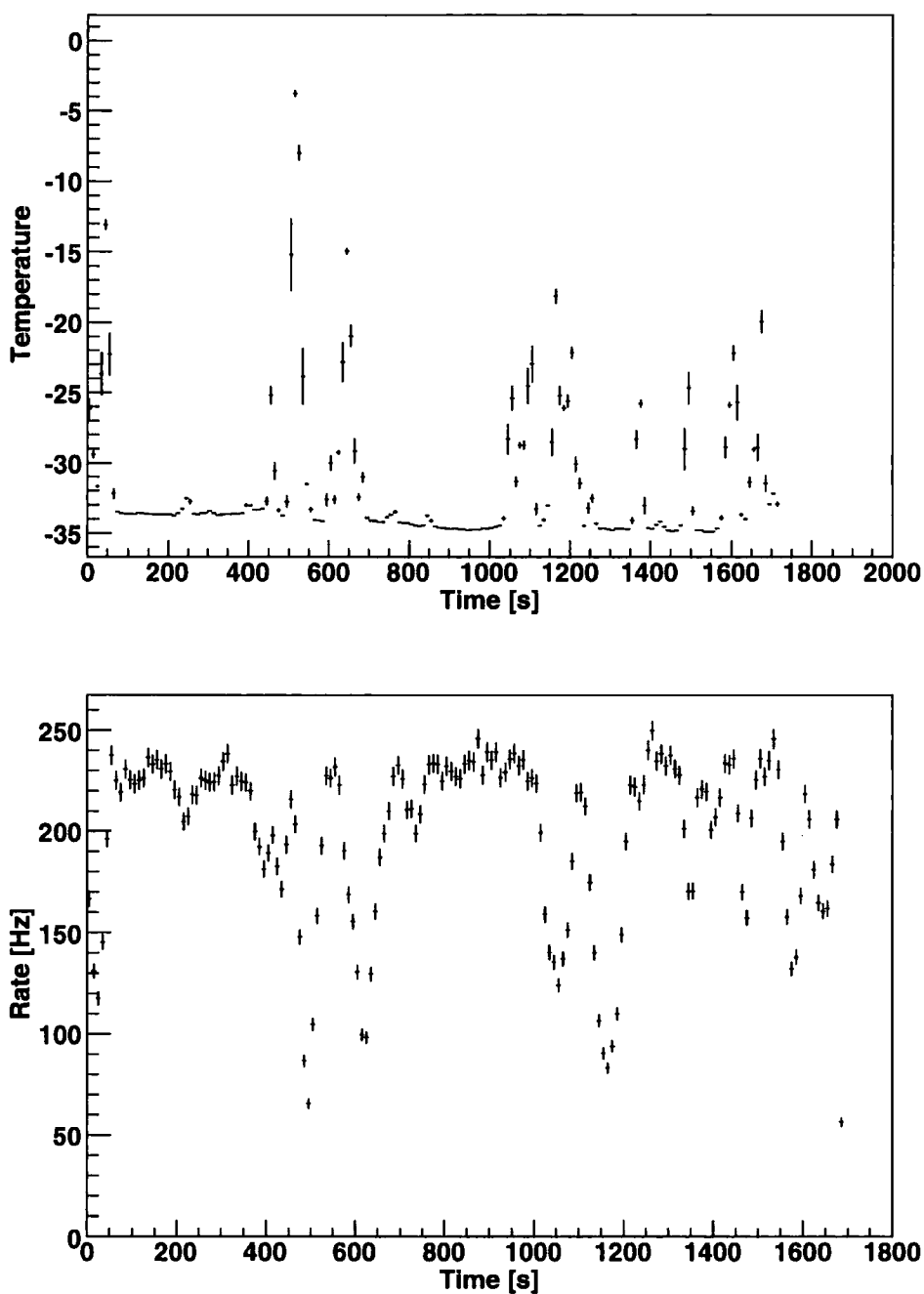


Figure 3.1: Radiometer (top) and central trigger plots from Run 020817 on GRS 1915+105 taken on 16/17 August 2004. The graphs clearly show how interruption by clouds affects the temperature and also show the anticorrelation with the trigger rate. This run is of course rejected for data analysis.

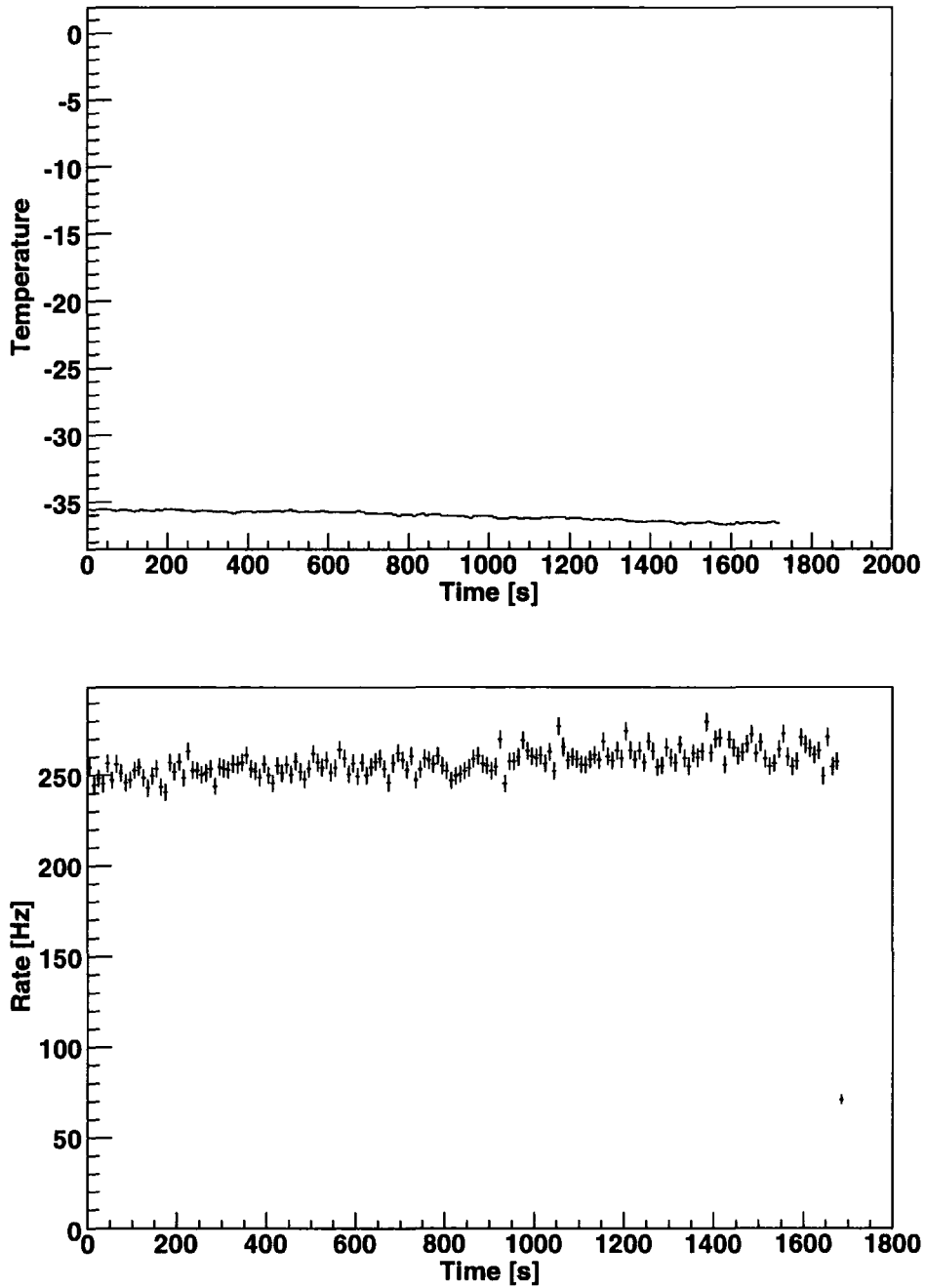


Figure 3.2: Radiometer (top) and central trigger plots from Run 020586 on GRS 1915+105 taken on 27/28 April 2004. This run is accepted for data analysis as it shows good stability throughout the run. The small increase in trigger rate is due to the decreasing zenith angle during the run, which is also indicated by the small drop in temperature.

3.3 H.E.S.S. Analysis Software

3.3.1 Introduction

The details of the analysis are covered in depth in [3] but for completeness and to give some insight into the analysis procedure and the results presented, they are summarised here.

3.3.2 Data Taking

The technique of imaging atmospheric Cherenkov light to detect γ -rays depends on the estimation of an incident photon's energy. This is achieved using the signal recorded at the camera of the subsequent particle air shower. Only those events that pass the trigger criterion, set out earlier, are recorded in a raw data file, a typical file containing several hundred of thousands of events. These events are then calibrated and cleaned to remove non-hadronic and non- γ -ray triggered events. To achieve this means having the best understanding possible of the main characteristics of the technique.

- Firstly the interaction of the particles and photons with the atmosphere. The atmosphere is one of the main components of the detector and is probably the least understood. It is filled with sources of uncertainty such as pressure, temperature, humidity, dust, aerosols and clouds, all of which can vary during observation. Radiometers and lidars are used to take measurements of the atmospheric properties (see for example [7]) and detailed simulations are used to estimate the incident photon's energy.
- Secondly the optical response of the telescopes including the properties of the mirrors, the Winston cones and also how shadows of the structure affect the recorded signal. This is measured using the Cherenkov light from muons that pass close to the telescope.
- Thirdly, how the camera responds to photons. As mentioned earlier, the camera consists of 960 photomultiplier tubes each with slightly different

single photo-electron (p.e.) gains and response characteristics. The single p.e. gain of each tube is measured using an LED mounted at the front of the camera. The response of each tube is calibrated using an LED mounted in the dish (flat-fielding). This allows the variations in quantum efficiency of each tube together with the effect of each Winston cone to be corrected. A detailed description of the camera calibration and uncertainties associated with it can be found in [1].

3.3.3 Gamma-Hadron Separation

Once calibrated, the γ -ray events must be separated from the overwhelming background of events due to hadronic interactions. The first stage is image cleaning. This is performed to ensure that only pixels responding to Cherenkov light are included in an image. All the images in the analysis included in this discussion are cleaned using the '5-10' criteria. This is a two stage filter requiring that a pixel must have a signal level above a threshold of 5 p.e. and additionally have a neighbouring pixel above a threshold of 10 p.e. It is a requirement that the converse is also true. Once the images are cleaned in this fashion, a γ -ray event has an image roughly elliptical in shape whereas a hadronic event will be wider and less well defined in shape. To discriminate between events of γ -ray or hadronic origin, second-order Hillas parameters¹ are calculated. Fig.(3.3) shows the definition of the important parameters for this analysis. The length, width and image amplitude all relate to the shape of the image, whereas the distance, miss, α and θ , relate to the orientation and the direction of the shower.

Mean Scaled Parameters

To obtain a value for the length and width of the events the analysis uses a set of look up tables. These tables, defined for different zenith angle ranges, contain the predicted mean width and mean length for a given image amplitude and impact parameter by means of extended air shower simulations. The image amplitude is the total light from the event that is recorded in the camera. The

¹Appendix B

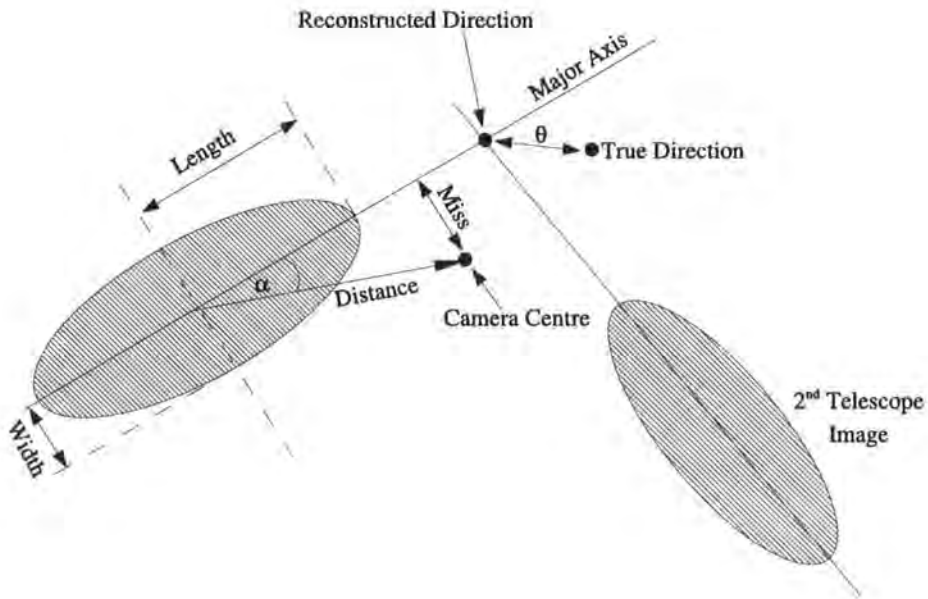


Figure 3.3: Graphical representation of second-order Hillas parameters. the two superimposed images are of the same event as recorded in two telescopes. Also shown is θ , the offset of the reconstructed direction of the shower seen in two cameras or more. The ‘on’ region is defined by a circle around a given point in the sky of radius θ . The α and miss parameters are generally used in single telescope analysis, and are not relevant here.

impact parameter defines the distance of the shower core on the ground from the telescope and can be reconstructed from the stereo images to within $< 5\%$ error for events falling within 200m of the array centre. The actual value of the width or length parameter p of the event is then compared to the expected value $\langle p \rangle$ using the relation,

$$p_{sc} = \frac{(p - \langle p \rangle)}{\sigma_p} \quad (3.1)$$

where σ_p is the deviation from $\langle p \rangle$ also stored in lookup tables and derived from simulations. The mean of the scaled parameters $\langle p_{sc} \rangle$ is then calculated over the telescopes used for the observation forming the mean reduced scale width (MRSW) and mean reduced scale length (MRSL) for each event.

Selection Cuts

Once each event has been parameterised, selection cuts are applied to the mean scaled parameters as well as to image intensity and θ^2 to maximise the detection significance σ , as defined in [105]. The cuts used in this analysis are the optimised cuts, provided for the standard H.E.S.S. analysis software for a point source, and are given in Table(3.1). The θ^2 parameter is an indication of

Min. Image Amplitude	MRSW (min.)	MRSW (max.)	MRSL (min.)	MRSL (max.)	θ^2 (max.)	Distance (max)
80 p.e.	-1.7	0.9	-2.0	1.3	0.02	100

Table 3.1: Optimised γ -ray selection cuts for a point source used for the analysis. In addition to these cuts the events must pass cuts imposed on the image amplitude and distance in at least two telescopes.

the excess of events that are emitted from the source. Events produced by γ -rays emitted from the source will have a small value of θ^2 and thus survive this cut. The width of the distribution defines the accuracy in the arrival direction of the γ -ray events and again, as with MRSW and MRSL, the cut is optimised

² θ is the radial offset of the reconstructed direction of the shower as seen in two cameras or more, see Fig.(3.3)

using detailed simulations to maximise detection significance. The distance cut rejects events that have their image centroid too far from the centre of the field of view, in which case there may be information lost due to truncation at the edge of the camera. The distance is used along with image amplitude to estimate the energy of the primary γ -ray. As with the mean scaled parameters this is achieved through look up tables based on extensive simulations.

3.3.4 Background Estimation

In order to estimate the flux of γ -rays from the source, an estimation of the background level of non γ -ray events, in the same direction as the source, is needed. Once background subtraction has been applied the significance of the excess is calculated using the likelihood formula [105],

$$\begin{aligned}
 S &= \sqrt{-2 \ln \lambda} \\
 &= \sqrt{2} \left\{ N_{on} \ln \left[\frac{1 + \alpha}{\alpha} \left(\frac{N_{on}}{N_{on} + N_{off}} \right) \right] + N_{off} \ln \left[(1 + \alpha) \left(\frac{N_{off}}{N_{on} + N_{off}} \right) \right] \right\}^{\frac{1}{2}}
 \end{aligned}
 \tag{3.2}$$

where λ is the maximum likelihood ratio, N_{on} is the number of events on-source, N_{off} is the number of events off-source, and α is the ratio of the on-source time to the off-source time.

There are different methods for estimating the background. The first is to perform an off-source ('off') run. This is an observation made before or after the on-source ('on') observation run, which tracks the same altitude-azimuth part of the sky as is covered during the 'on' observation. The disadvantages of this are that two runs have to be made for each observation and the background used is usually around 7.5° in right ascension away from the source itself, depending on the duration of the observation runs.

The so called 'wobble' method is the standard for H.E.S.S. This uses the 'on' observation run to provide the background by offsetting the source to one side of centre of the field of view, usually by 0.5° . In its simplest form the background is estimated using the part of the sky with the same offset as the source, but in the opposite direction in the field of view. Two other methods,

which use a larger sample for the background, are the reflected background model and the ring background model.

Reflected Background Model

This model uses several areas of equal size that are equidistant from the centre of the field of view of the camera. The source is at the centre of one of these areas as shown by the cross in Fig.(3.4). A normalisation factor defines the ratio of on-source to off-source areas being tested. This method cannot be used for source positions close to the centre of the field of view as the background positions would overlap with each other and the on-source area. One advantage to this method is that any radial variations in the detector are compensated for by the radial nature of the model, and as such this may be a more suitable model for spectral analysis than the ring background model.

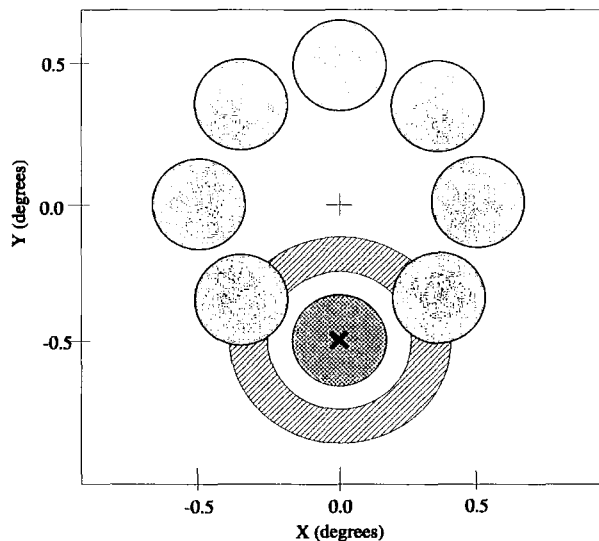


Figure 3.4: Graphical representation of the wobble background methods. The blue hatched area is that defined as on-source. The ring background is shown as the annulus around that area, shaded with diagonal lines. The reflected background areas are shaded in grey.

Ring Background Model

Using this model, the background is estimated from the rate measured in a ring around the source position. The inner and outer ring radii are conventionally chosen so that the ‘off’ area is roughly 7 times the ‘on’ area. A normalisation factor is again defined and this is weighted to account for any radial variations due simply to position in the detector. Any position within the background annulus where there is a known source is omitted, to avoid contamination of the background rate. This method is best suited to point sources since contamination of the background annulus by an extended source may again contaminate the background rate, but it does have the advantage over the reflected background model that the background can be estimated for any source in the field of view, not just the target source. All the analysis that follows has been performed using this background model.

3.3.5 Flux Measurements and Upper Limits

The γ -ray flux is estimated from the number of excess events using the effective area of the telescopes. A spectral form for the source is assumed e.g. a power law with photon index Γ . The integrated flux above the threshold energy is then given by,

$$\delta = I_0 \int_0^{E_c} \int_t \left(\frac{E}{E_0} \right)^{-\Gamma} A_{Etrue}(E, Z(t)) dt dE \quad (3.3)$$

where δ is the number of photons $\text{cm}^{-2} \text{s}^{-1}$, I_0 is calculated by integrating the effective area, $A_{Etrue}(E, Z(t))$, up to a cut-off energy E_c , which is normally above 100 TeV (imposed by the Monte Carlo simulations) and over the range of zenith angles during the observation [3].

The effective area can be defined as the area in which the core of the shower must be positioned for the shower to trigger the telescope array and is a function of the zenith angle of the observations and the energy of the event. It is calculated using simulations of events over a large area and recording the fraction of events that trigger the telescope and pass the selection cuts. The

effective area is then given by,

$$A_{Etrue}(E, Z(t)) = A_{Total} \left(\frac{N_{total}(E, Z(t))}{N_{trigger}(E, Z(t))} \right) \quad (3.4)$$

The effective area has a strong dependence on the zenith angle of the observations. Simulations determine the effective area for a range of zenith angles and energies and then the value for a given zenith angle and energy is interpolated. Upper limits for sources where there is no significant detection are calculated using the unified approach of Feldman and Cousins [30][101], which was developed in the neutrino physics field to deal with very weak or null signals. This provides a figure for the minimum flux required above either the threshold energy or, as is more conventionally used, 1 TeV, which would give a γ -ray detection at the 90% confidence level.

3.3.6 Crab Results

As in [3] the example source used to describe the analysis is the Crab nebula, although the data selected are different to those selected in [3]. Since its first significant discovery as a VHE γ -ray source in 1989 [108], the Crab nebula has become the conventional standard candle for VHE γ -ray astronomers.

Between October 2003 and January 2005, the Crab nebula was observed by H.E.S.S. for a total of 97.194 hours before selection cuts, using various telescope configurations. For the purpose of this section only five runs are used. These data were taken on the nights of 22-11-2004, 5-12-2004 and 3-1-2005 totalling 1.79 hours of observation time and using all four telescopes of Phase 1 of the H.E.S.S. array. All the runs have passed the selection criteria previously discussed. Using the cuts in Table 3.1 the number of events are $N_{on} = 970$, $N_{off} = 711$ with a normalisation factor of 0.147, leading to an excess of 866γ . Fig.(3.5) shows the results of the analysis.

The graphs displayed in Fig.(3.5) give a good example of the graphs produced for a source known to significantly emit γ -rays. These four plots are also produced for each of the microquasars that H.E.S.S. observed.

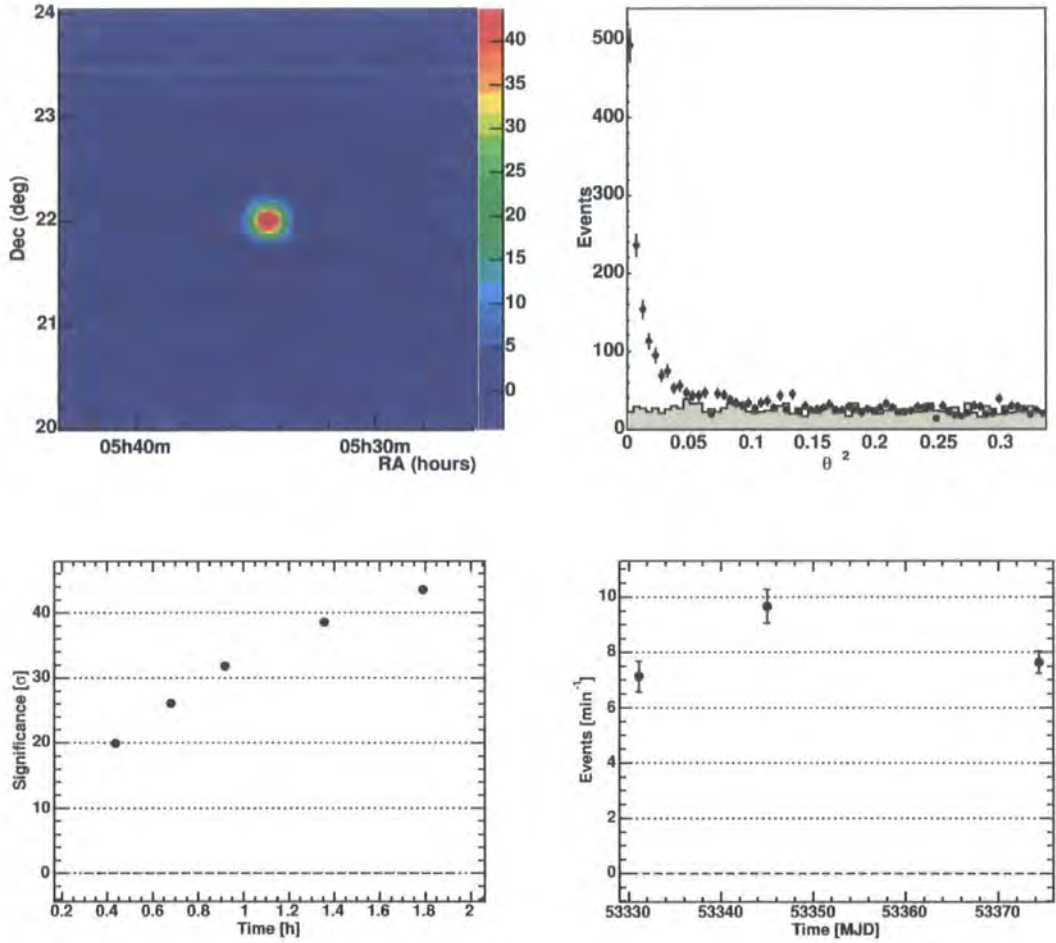


Figure 3.5: Crab Nebula Results. The top left plot shows the 2-d significance sky map showing a strong signal from the Crab Nebula. The right hand scale shows the detection significance of 43.5σ in 1.79hrs, equivalent to a rate of $8.1 \pm 0.2 \gamma \text{ min}^{-1}$ at $32.5\sigma \text{ hr}^{-1}$. The top right plot shows the θ^2 distribution for the normalised ‘off’ region (shaded area) and the ‘on’ region (points). As is expected, close to $\theta^2 = 0$ there is a large excess of events in the ‘on’ region as is expected for a positive detection. The lower two graphs show the cumulative significance as a function of observation time (left) and the γ -ray daily excess rate plotted over the chosen period of observation (right), again showing a high significance detection.

3.4 Microquasar Analysis Results

The full four telescope array of H.E.S.S. Phase I was used to observe the microquasars GRS 1915+105, Circinus X-1, GX 339-4 and V4641 Sgr. For each microquasar considered, a summary of the observation runs used is given, a summary of runs failing the selection criteria, and the results of the analysis from the standard H.E.S.S. analysis software, together with any appropriate discussion, are given. The plots are given in the same format and order as those for the Crab Nebula so that direct comparison can be made. Since no significant emission is detected from any of the microquasars, upper limits at both the average energy threshold of the observations and >1 TeV are also presented.

3.4.1 GRS 1915+105

GRS 1915+105 was observed towards the end of April 2004 and the beginning of May 2004. The motivation for the observations was provided by a private communication from Guy Pooley, who regularly monitors the radio state of this object using the Ryle Telescope ³, complemented by RXTE ASM data. A notification was received to inform us that if GRS 1915+105's behaviour was consistent with previous patterns of activity, then a fifty day plateau state had come to an end, which should result in superluminal ejections within around 24 hours. An observation schedule, summarised in Table 3.2, was prepared for H.E.S.S., which resulted in a total of 8.43 hours after run selection, and an RXTE ToO triggered.

The reason for the extended break between 3/5/04 and 16/5/04 is due to the moonlight period when observations cannot be carried out. Unfortunately after some flares during the moonlight period, which were detected by INTEGRAL's JEM-X monitor at up to more than 3 Crab in JEM X 3-30 keV

³The Ryle Telescope (RT) is an 8-element interferometer operating at 15 GHz (2cm wavelength). The elements are equatorially mounted 13 m Cassegrain antennas, on an (almost) E-W baseline. Four aerials are mounted on a 1.2 km rail track, and the others are fixed at 1.2 km intervals. Baselines between 18 m and 4.8 km are therefore available, in a variety of configurations. For high-resolution imaging, the mobile aerials are arranged along the track, to give uniform baseline coverage to 4.8 km

lightcurve, GRS 1915+105 appeared to return to a plateau state.

Some of the runs, indicated in the table, had no calibration summary files available. To gauge if these files were acceptable for analysis, the telescope trigger rate (MRT) and radiometer sky temperature (MRR), which are monitored throughout the observation run, are examined. In particular, the rms values give an indication of how variable the temperature and trigger rates were during each run. As an example for a bad run such as Run020817 shown in Fig.(3.1), the radiometer rms value is 5.19 compared to 0.35 for a good run like Run02056 shown in Fig.(3.2). Likewise the trigger rate rms value for Run020817 is 32.74, compared to Run020586, which is 5.33.

Results

Using the cuts in Table 3.1 the number of events are $N_{on} = 697$, $N_{off} = 4728$ with a normalisation factor of 0.144 leading to an excess of 16γ and a significance of 0.51σ . Fig.(3.6) top right shows the on source and normalised off source distribution of θ^2 . As can be seen the background is flat, as one would ideally expect, and the on source distribution clearly shows no significant detection in the direction of GRS 1915+105. Table 3.3 summarises the run by run results.

An interesting point to note is the 4σ ‘hot spot’ at around R.A. 19h14m Dec. $9^{\circ}54'$ of the significance sky map, Fig.(3.6) top left. This position is roughly consistent with the HMXB IGR J19140+0951 discovered in 2003 [49] with INTEGRAL, see Fig.(3.7). This is no more than a very tentative connection at this stage; it will be investigated further at a future date.

Run No.	Date	Accepted	MRR (rms)	MRT (rms)	Comments
20585	28/4/2004	Yes	-	6.20869	
20586	28/4/2004	Yes	0.3519581	5.33298	small temp variance on CT2 - no effect on trigger rates
20587	28/4/2004	Yes	0.767407	4.57184	MRR shows possible clouds - trigger rates OK
20588	28/4/2004	Yes	0.189337	4.9818	
20599	29/4/2004	Yes	0.316088	5.01168	no Online Summary. OK by database and logs
20600	29/4/2004	Yes	0.664042	4.64432	no Online Summary. OK by database and logs
20601	29/4/2004	Yes	0.115557	4.43191	no Online Summary. OK by database and logs
20602	29/4/2004	Yes	0.0850611	4.35209	no Online Summary. OK by database and logs
20610	30/4/2004	Yes	0.228036	5.01504	small change in temp. on CT2 - trigger rate OK
20611	30/4/2004	Yes	0.791692	4.71819	high backscatter logged - trigger rates OK
20612	30/4/2004	Yes	0.148947	4.69291	
20613	30/4/2004	No	0.106791	4.37845	run stopped early - not accepted by analysis program
20620	1/5/2004	Yes	0.225394	4.32155	
20621	1/5/2004	No	0.113297	4.85399	corrupt data file (?)
20627	2/5/2004	Yes	0.342643	5.03796	Online Summary file corrupt - database and logs OK.
20628	2/5/2004	Yes	0.239082	4.48884	Online Summary file corrupt - database and logs OK.
20629	2/5/2004	Yes	0.12259	4.54169	Online Summary file corrupt - database and logs OK.
20633	3/5/2004	Yes	0.0683055	6.01358	
20791	16/5/2004	Yes	0.864682	5.22412	some variations in temperature - trigger rate OK
20792	16/5/2004	Yes	0.180714	4.71028	small cloud at end of run - trigger rate OK
20793	16/5/2004	Yes	0.106064	4.77219	
20794	16/5/2004	Yes	0.0799194	4.16294	short run but good
20817	17/5/2004	No	5.19216	32.7438	heavy cloud contamination
20818	17/5/2004	Yes	0.452082	7.40027	small cloud at beginning of run

Table 3.2: Summary of data quality selection for observation runs on GRS 1915+105

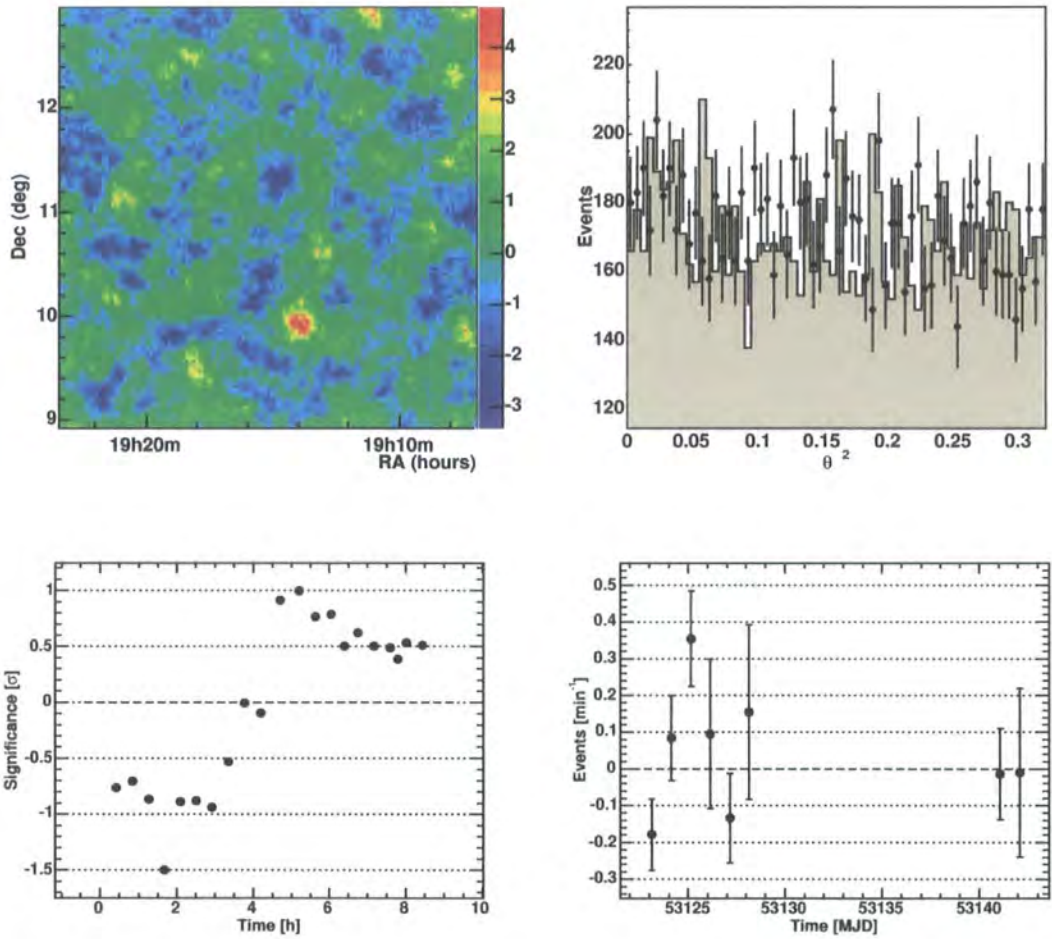


Figure 3.6: GRS 1915+105 Results. The top left plot shows the 2-d significance sky map centred on GRS 1915+105. There is no significant signal present. However the ‘hot spot’, lower and right of centre, is roughly consistent with the HMXB IGR J19140+0951 [49], see Fig.(3.7), and will be investigated at a future date. The ‘on’ source θ^2 distribution is flat, consistent with no signal.

Run No.	Zenith Angle	Events ON	Events OFF	OFF Norm	Significance
20585	38.7664	21	173	0.14452	-0.763839
20586	35.6889	30	218	0.144994	-0.270033
20587	34.2443	30	228	0.144928	-0.503737
20588	38.7798	33	293	0.144432	-1.40013
20599	36.3453	37	214	0.14505	0.966127
20600	33.7779	36	257	0.144536	-0.176733
20601	35.0687	37	271	0.144771	-0.336817
20602	37.3975	47	285	0.144134	0.841719
20610	35.2372	37	190	0.145384	1.57341
20611	34.2401	29	213	0.144717	-0.310697
20612	35.3421	57	251	0.143619	2.97272
20620	34.7178	43	278	0.144428	0.41484
20627	34.2209	29	233	0.143788	-0.746805
20628	35.6461	34	229	0.143562	0.182198
20629	34.5108	28	237	0.144713	-1.04253
20633	37.3101	29	179	0.143777	0.587969
20791	34.2956	29	223	0.141697	-0.439513
20792	34.7907	33	228	0.144844	-0.00397
20793	33.7676	18	141	0.146345	-0.555433
20794	34.3545	21	117	0.143859	0.909854
20818	34.2847	39	270	0.145388	-0.03803
Total	-	697	4728	0.144399	0.509013

Table 3.3: Summary of data collected on observation runs for GRS 1915+105

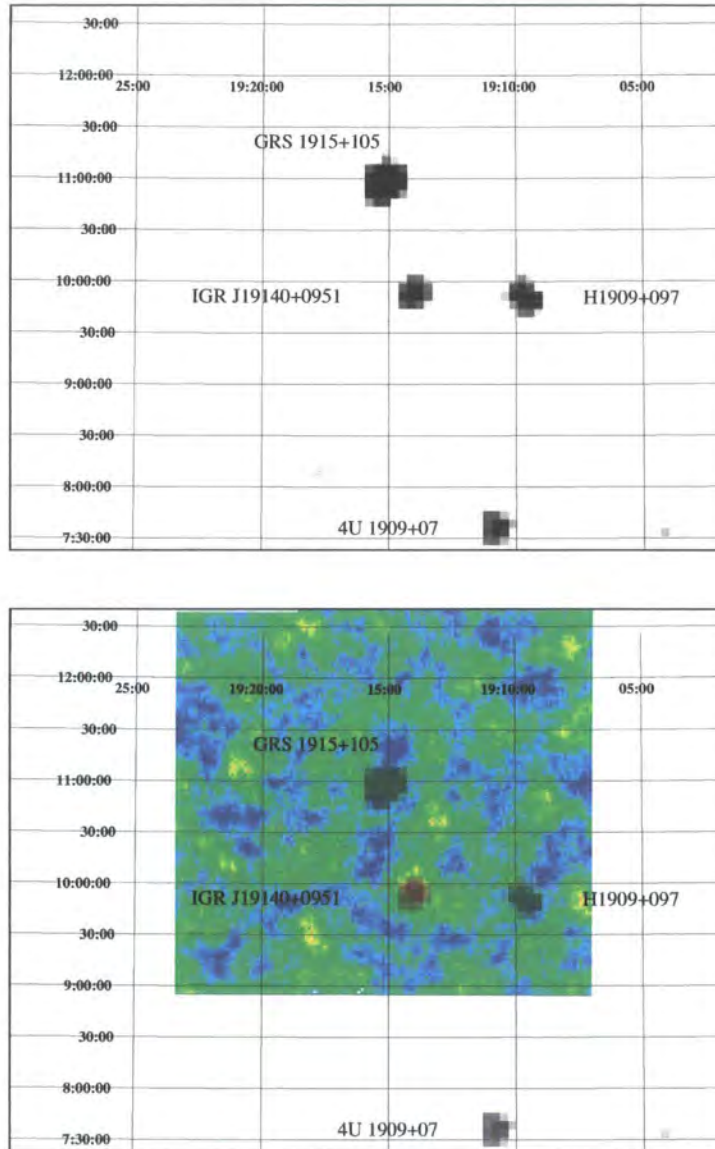


Figure 3.7: The IBIS/ISGRI 20-30keV image from [49] (top) showing the position of GRS 1915+105 and IGR J19140+0951. The bottom image shows the overlay of the significance sky map from the H.E.S.S. analysis from Fig.(3.6)

3.4.2 Circinus X-1

Circinus X-1 was observed on the nights of 18/6/2004, 19/6/2004 and 20/6/2004, summarised in Table 3.4, for a total of 5.35 hours after run selection. This observation was scheduled as part of a multiwavelength observation with RXTE. The three observation periods, separated by around 1 day, were designed to cover the periastron passage of the compact object in its 16.6 day orbital period. All the H.E.S.S. observation runs were used; although two had some hardware problems at the edge of the field of view, they were included to give as much simultaneous coverage as possible.

Results

Using the cuts defined in Table 3.1, the result is $N_{on} = 487$, $N_{off} = 3240$ with a normalisation factor of 0.144 leading to an excess of 20γ and a significance of 0.89σ . Fig.(3.8) shows the results of the H.E.S.S. observations of Circinus X-1, Table 3.5 summarising the run by run results. The θ^2 plot again shows no significant detection in the H.E.S.S. data. There are no significant excess areas in the significance sky map and there is no significant change in the cumulative significance or the daily excess rates for the periastron period.



Run No.	Date	Accepted	MRR (rms)	MRT (rms)	Comments
21285	18/6/2004	Yes	0.314828	3.98778	CT4 drawer C2 off
21286	18/6/2004	Yes	0.177486	4.11387	
21287	18/6/2004	Yes	0.198014	4.13761	CT4 drawerA3 off
21289	18/6/2004	Yes	0.11376	3.78625	
21312	19/6/2004	Yes	0.39027	4.27647	
21313	19/6/2004	Yes	0.309649	4.50413	Long run to cover RXTE window
21314	19/6/2004	Yes	0.154354	4.49504	
21315	19/6/2004	Yes	0.149437	4.30434	
21337	20/6/2004	Yes	0.246875	4.43512	Long run to cover RXTE window
21338	20/6/2004	Yes	0.11814	4.33862	Long run to cover RXTE window
21339	20/6/2004	Yes	0.129369	4.25716	Online Summary file corrupt - database and logs OK.
21340	20/6/2004	Yes	0.197607	4.05752	Online Summary file corrupt - database and logs OK.

Table 3.4: Summary of data quality selection for observation runs on Circinus X-1. Runs 21285 and 21287 included as the camera drawer errors on CT4 are at the edge of the field of view and trigger rates, temperature, MRR and MRT indicate good observation runs.

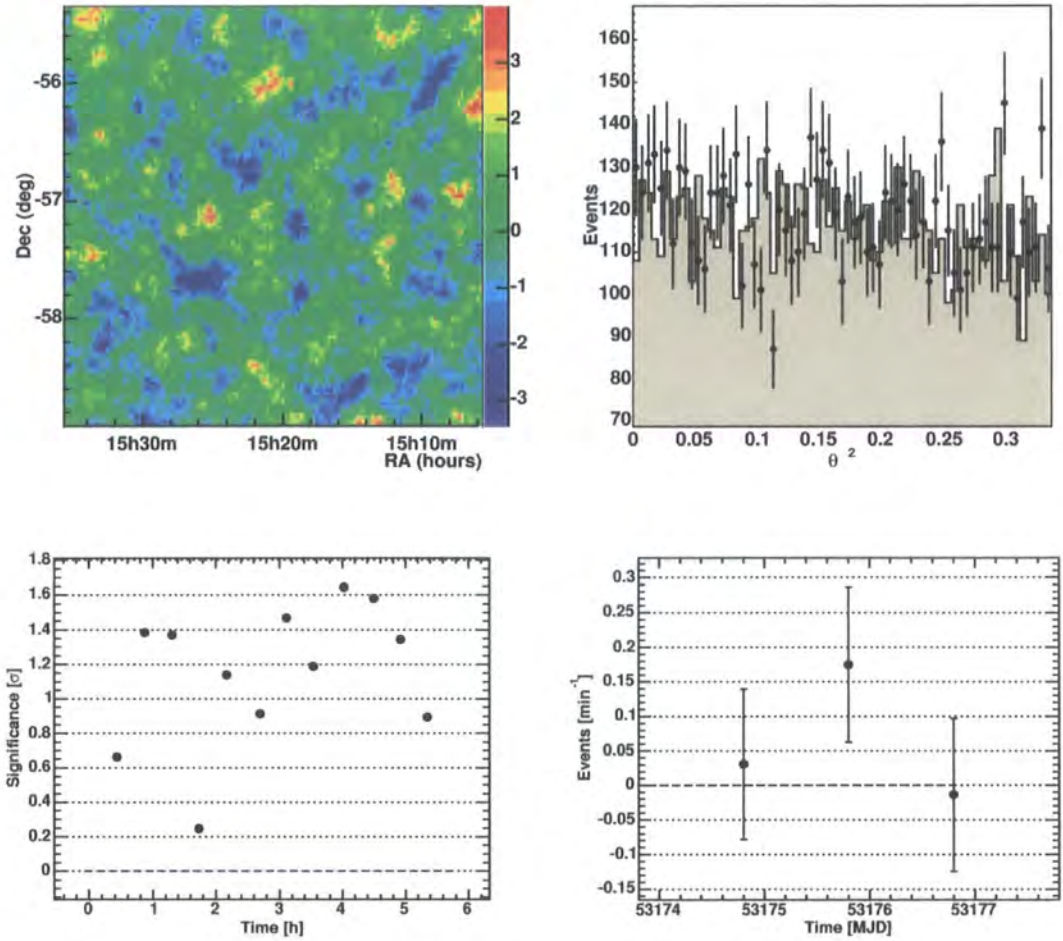


Figure 3.8: Circinus X-1 Results. The top left plot shows the 2-d significance sky map centred on Circinus X-1. There is no significant detection as can be seen from the flat θ^2 for the ‘on’ region. The lower two graphs show no significant change over the periastron period.

Run No.	Zenith Angle	Events ON	Events OFF	OFF Norm	Significance
21285	37.3631	41	256	0.143057	0.662095
21286	35.1726	41	227	0.143745	1.31027
21287	34.7765	36	238	0.14086	0.394872
21289	42.014	30	291	0.144763	-1.85393
21312	37.9384	43	205	0.145326	2.10076
21313	35.8867	41	300	0.142726	-0.26199
21314	34.7532	49	265	0.143489	1.58365
21315	36.8353	37	281	0.143664	-0.503972
21337	34.6239	48	261	0.143588	1.53135
21338	33.485	46	310	0.146219	0.0929941
21339	34.5751	39	297	0.143111	-0.510735
21340	34.4559	36	309	0.146422	-1.3376
Total	-	487	3240	0.143897	0.385676

Table 3.5: Summary of data collected during observations of Circinus X-1.

3.4.3 GX 339-4

GX 339-4 was observed on the nights of 12/8/2004, 13/8/2004 and 14/8/2004 for a total of 5.01 hours after run selection. Although information was received that the object was leaving the low hard state, which could result in a radio flare [57], simultaneous observations with RXTE were not possible as it would have interfered with an existing multi-wavelength observation campaign on the AGN PKS2155-304. Based on the predictions for the behaviour of GX 339-4, it was still observed by H.E.S.S. once the PKS2155-304 window had finished.

Results

Using the cuts defined in Table 3.1 the result is $N_{on} = 373$, $N_{off} = 2474$ with a normalisation factor of 0.143 leading to an excess of 19γ and a significance of 0.93σ . Fig.(3.9) shows the results of the observations and Table 3.5 summarises the run by run results. No significant excess can be seen in the θ^2 plot in the direction of GX 339-4.

Run No.	Date	Accepted	MRR (rms)	MRT (rms)	Comments
19273	2/3/2004	No	0.378638	5.65899	Out of sequence (see text)
19274	2/3/2004	No	0.437529	5.47401	Out of sequence (see text)
21995	12/8/2004	Yes	0.0696208	4.38027	Hazy sky. Trigger rates OK
21996	12/8/2004	Yes	0.113151	3.685	Hazy sky. Trigger rates OK
21997	12/8/2004	Yes	0.0793722	3.86866	Hazy sky. Trigger rates OK
21998	12/8/2004	Yes	0.0689063	4.31545	Hazy sky. Trigger rates OK
22016	13/8/2004	Yes	0.287234	4.60246	
22017	13/8/2004	Yes	0.126021	3.73603	
22019	13/8/2004	Yes	0.172932	4.49693	
22020	13/8/2004	Yes	0.308165	4.26153	
22022	13/8/2004	Yes	0.257057	4.35459	Low but consistent trigger rate
22023	13/8/2004	Yes	0.192116	4.46338	Low but consistent trigger rate
22039	14/8/2004	Yes	0.0753786	3.63035	Low but consistent trigger rate
22040	14/8/2004	Yes	0.120077	4.1824	Low but consistent trigger rate
22042	14/8/2004	Yes	0.443885	3.91413	V.Low but consistent trigger rate. High humidity
22043	14/8/2004	Yes	0.35133	3.84735	V.Low but consistent trigger rate. High humidity

Table 3.6: Summary of data quality selection for observation runs on GX 339-4.

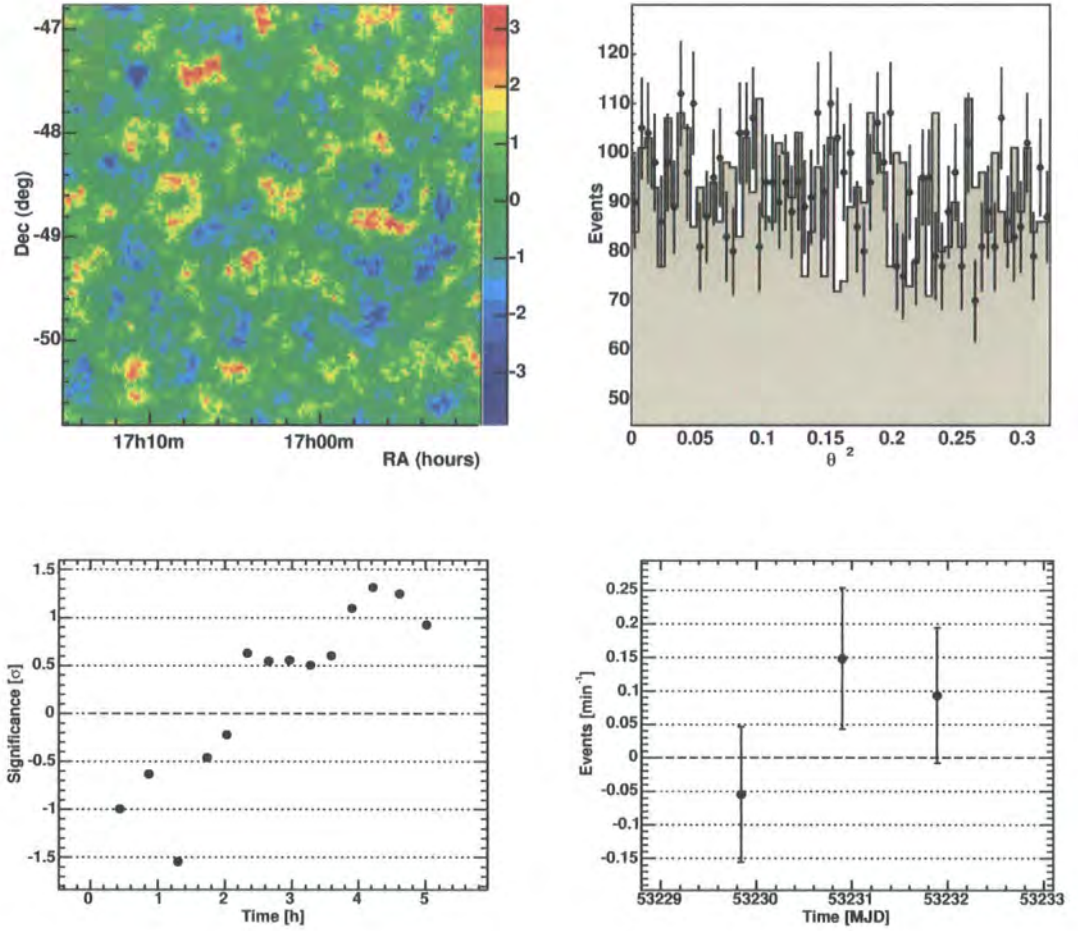


Figure 3.9: GX 339-4 Results. The top left plot shows the 2-d significance sky map centred on GX 339-4. No significant detection is observed, confirmed by a flat θ^2 distribution for the ‘on’ region. The cumulative significance (lower left) and the daily excess (lower right) graphs are inconclusive.

Run No.	Zenith Angle	Events ON	Events OFF	OFF Norm	Significance
21995	25.286	31	262	0.142233	-0.992858
21996	25.753	38	262	0.143031	0.08016
21997	28.6589	22	227	0.14478	-1.89978
21998	30.882	39	197	0.142452	1.80927
22016	35.2854	39	197	0.142452	1.80927
22017	25.0405	42	210	0.140877	1.99296
22019	26.53	26	185	0.144358	-0.128401
22020	31.0343	24	165	0.141541	0.124423
22022	34.4305	19	134	0.145849	-0.115503
22023	44.503	18	111	0.143343	0.478312
22039	48.32	30	141	0.144453	1.8456
22040	29.6823	26	146	0.144011	0.973153
22042	32.9297	18	130	0.143277	-0.136534
22043	42.0884	11	119	0.143388	-1.48103
Total	-	373	2474	0.14318	0.923857

Table 3.7: Summary of data collected on observation runs for GX 339-4.

3.4.4 V4641Sgr

V4641Sgr was observed on the nights of 8/7/2004, 9/7/2004 for a total of 1.735 hours after run selection. It was observed mainly as a response to the report of optical brightening of the object [103]. If it had followed the same pattern as the 1999 outburst [54] the object may have displayed the same massive outburst. On this basis H.E.S.S. observations were scheduled and an RXTE ToO was triggered. No further observations after this date were done due to a combination of full moon and scheduled observation programs.

Results

Using the cuts in Table 3.1 the number of events are $N_{on} = 215$, $N_{off} = 1506$ with a normalisation factor of 0.143 leading to a zero excess and a significance of -0.04σ . Fig.(3.10) show the results of the observations and Table 3.9 summarises the run by run results. No significant excess can be seen in the θ^2 plot in the direction of V4641Sgr.

Run No.	Date	Accepted	MRR (rms)	MRT (rms)	Comments
21509	8/7/2004	Yes	0.0770767	4.1998	Partial sky cover. Target clear
21510	8/7/2004	Yes	0.0793409	4.92799	Partial sky cover. Target clear
21519	9/7/2004	Yes	0.12261	4.45776	Missed RXTE window due to clouds.
21520	9/7/2004	Yes	0.146972	7.51375	Missed RXTE window due to clouds.

Table 3.8: Summary of data quality selection for observation runs on V4641 Sgr.

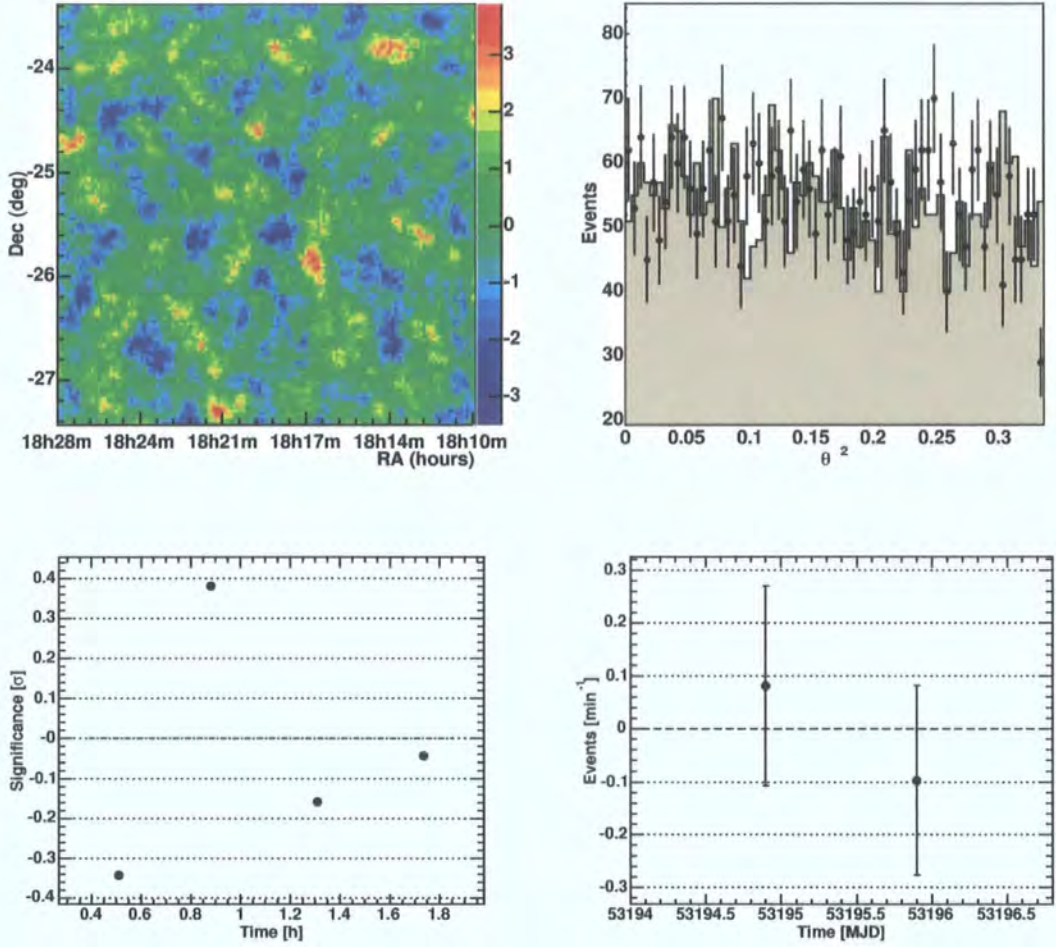


Figure 3.10: V4641 Sgr. Results. The top left plot shows the 2-d significance sky map centred on V4641 Sgr. No significant detection is observed, confirmed by a flat θ^2 distribution for the ‘on’ region

Run No.	Zenith Angle	Events ON	Events OFF	OFF Norm	Significance
21509	8.3734	65	477	0.142552	-0.342905
21510	4.60334	50	297	0.143648	1.01862
21519	3.20962	46	364	0.144127	-0.854419
21520	3.04646	54	368	0.142751	0.188461
Total	-	215	1506	0.143217	-0.0436586

Table 3.9: Summary of data collected on observation runs for V4641 Sgr.

3.5 Results Summary

No significant detection of γ -rays was observed from any of the four microquasars discussed. Upper limits on H.E.S.S. detection are presented in Table 3.10 using an assumed differential photon index of $-3.0 \leq \alpha \leq -1.5$. It was found that the upper limit was relatively insensitive to the spectral slope used. Simultaneous observations with RXTE of GRS 1915+105, V4641 Sgr

Target	Average Energy Threshold (AET) (GeV)	H.E.S.S. Integral Flux Upper Limits (Ergs m ⁻² s ⁻¹)			
		> AET	> 1 TeV		
		$\alpha = -2.0$	$\alpha = -1.5$	$\alpha = -2.0$	$\alpha = -3.0$
GRS 1915+105	250	7.00×10^{-9}	3.00×10^{-10}	5.22×10^{-10}	1.15×10^{-9}
Circinus X-1	280	1.08×10^{-8}	7.10×10^{-10}	1.24×10^{-9}	2.88×10^{-9}
GX 339-4	240	1.03×10^{-8}	5.91×10^{-10}	9.90×10^{-10}	2.16×10^{-9}
V4641 Sgr.	140	3.48×10^{-8}	1.13×10^{-9}	1.69×10^{-9}	2.87×10^{-9}

Table 3.10: Integral flux upper limits for the H.E.S.S. observations on microquasars. Values above the average energy threshold for the observations and above the more conventional 1 TeV are given. The relative insensitivity to the assumed spectral slope is also demonstrated by assuming three different values of α to calculate upper limits 1 TeV.

and Circinus X-1 were undertaken [22]. The results of those RXTE observations, Table 3.11, showed them to be consistent with the high soft state during which jets are expected to be suppressed [31]. Very high energy γ -ray emission would likely be related to the presence of a jet as this would be where the highest energy particles exist, so the non-detection of γ -rays is not unexpected.

Target	Integral X-ray Flux (3.0-10keV) [ph cm ⁻² s ⁻¹]	X-ray Hardness Ratio (6.5-10keV)/(3.0-6.5keV)
GRS 1915+105	0.5195	0.28
Circinus X-1	1.796 x 10 ⁻²	0.19
V4641 Sgr.	1.91 x 10 ⁻³	0.41

Target	RXTE Observations (MJD)	H.E.S.S. Observations (MJD)	Overlap Time (MJD)
GRS 1915+105	53123.090 → 53123.109	53123.066 → 53123.149	53123.090 → 53123.109
	53127.096 → 53127.114	53127.106 → 53127.164	53127.106 → 53127.114
	53128.149 → 53128.164	53128.148 → 53128.164	53128.149 → 53128.164
Circinus X-1	53174.746 → 53174.760	53174.747 → 53174.831	53174.747 → 53174.760
	53175.767 → 53175.780	53175.734 → 53175.821	53175.767 → 53175.780
	53176.781 → 53176.793	53176.771 → 53176.857	53176.781 → 53176.793
GX 339-4	Not Observed	53229.772 → 53229.869	N/A
		53230.756 → 53230.913	N/A
		53231.807 → 53231.904	N/A
V4641 Sgr.	Not Observed	53194.883 → 53194.909	53194.885 → 53194.907
		53195.889 → 53195.906	53195.889 → 53195.892

Table 3.11: **Top:** Model x-ray fluxes and hardness ratios for the RXTE observations of GRS 1915+105, Circinus X-1 and V4641 Sgr. **Bottom:** Summary of RXTE and corresponding H.E.S.S. observation times given in modified julian date.[22]

Chapter 4

Vacuum Formed Aluminium Mirrors

4.1 The H.E.S.S. Phase I Telescope Mirrors

In the early 1990's, the University of Durham Gamma Ray Astronomy Group were building a new gamma ray telescope to be based in the Australian out-back. The design for the new telescope required large mirrors, which would have been prohibitively expensive if made from traditional glass. The vacuum forming technique (VFT), discussed in Section 4.2 was developed for the manufacture of research grade, ground based gamma ray telescope mirrors and was inspired by the need to economise, without compromising on reflectivity. The VFT was based on previously known aerospace technologies of creating lightweight rigid structures. The novelty of this process is in the manner with which the surface is formed by the vacuum.

In 2000 the Durham Group joined an international collaboration, H.E.S.S. (High Energy Stereoscopic System), named after Victor Hess, the discoverer of cosmic rays. H.E.S.S. were building an array of ground based Cherenkov telescopes in Namibia. The first phase of the H.E.S.S. telescope array in Namibia consists of four imaging atmospheric Cherenkov telescopes arranged in a square configuration of side length 120m. Each telescope consists of 382 segmented round mirror facets of diameter 600mm arranged in a Davies-Cotton configu-

ration [27]. These mirrors are produced by the companies Galactika (Armenia) and Compas (Czech Republic). They have a spherical profile and are produced using low expansion glass, which is then aluminised and quartz coated for protection. Each one is mounted on the telescope frame by three supports, two of which are motorised for alignment purposes. The specification for the glass mirrors are given in Table 4.1.

Material	Optical glass
Storage conditions:	$-10^{\circ} - +60^{\circ}$
Working conditions:	$-10^{\circ} - +30^{\circ}$
Diameter	$600\text{mm} \pm 1\text{mm}$
Thickness	15mm
Fixation	Glued on three supports (2 motorised)
Focal length	$15000\text{mm} \pm 250\text{mm}$
Focal spot (ϕ 80% of light)	$< 1 \text{ mrad}$
ϕ Reflecting surface	$600\text{mm} +1\text{mm} -2\text{mm}$
Specular reflectivity	$> 80\%$ for $300\text{nm} < \lambda < 600\text{nm}$

Table 4.1: Specification of H.E.S.S. Glass Mirrors

However, despite being of high optical quality, there are some major drawbacks with these mirrors:

- each mirror is expensive to produce; around U.S.\$1000.00
- the aluminised surface cannot be cleaned and has a limited lifetime . This requires removal of the mirror, shipping to Eastern Europe, realuminising and reshipping - an expensive process every two years (or even less)
- around 29% of Galactika mirrors and 20% of Compas mirrors fail the stringent optical test procedures after they have been passed by the factory [97]
- the mirrors weigh around 13kg each. This has implications for the whole telescope structure e.g. ‘sagging’ over time, slew speed

These disadvantages could affect the further development of the H.E.S.S. array. Phase II involves the commission of a further single-but-much-larger telescope.

This is likely to have a surface area of 600m^2 compared to 108m^2 for a Phase I telescope. Current designs are for 702 individual hexagonal mirror facets of 1m diameter. The significance of reducing the weight of these facets is readily apparent.

It was decided to improve the original VFT mirrors to the higher specification of the H.E.S.S. telescopes.

4.2 Mirror Construction Method

The idea for producing the mirror is quite straight forward (patent pending). A sheet of highly reflective aluminium sheet (Miro 27, henceforth referred to as 'Miro') is vacuum formed to a spherical shape over a suitably shaped mould. The rear surface is then prepared and a supporting structure consisting of aluminium honeycomb and an aluminium ring and backplate is bonded to the back. Once cured the vacuum is switched off and the waste material trimmed. Fig.(4.1). shows the construction method. There are some problems with this method.

Initially the 600mm diameter mirrors were being shaped on a 600mm mould. This has two drawbacks:

- the honeycomb and outer ring have to be placed exactly central with respect to the mould otherwise the spherical shape does not reach the edge of the mirror.
- the Miro does not follow the shape of the mould at the very edges. Fig.(4.1). shows an exploded view of the area affected by this.

To combat both these problems it was decided to make 500mm diameter mirrors on the 600mm mould, scaling accordingly for larger mirrors. This ensures the mirror is not formed at the edge and centralisation is not as critical.

The second problem encountered with this process is that the finished mirror shows a 'print through' of the honeycomb beneath it. This is a very small scale deformity, but is quite noticeable given the focal length of 15m and is enough to cause considerable diffusion of the incident light. This has now been cured

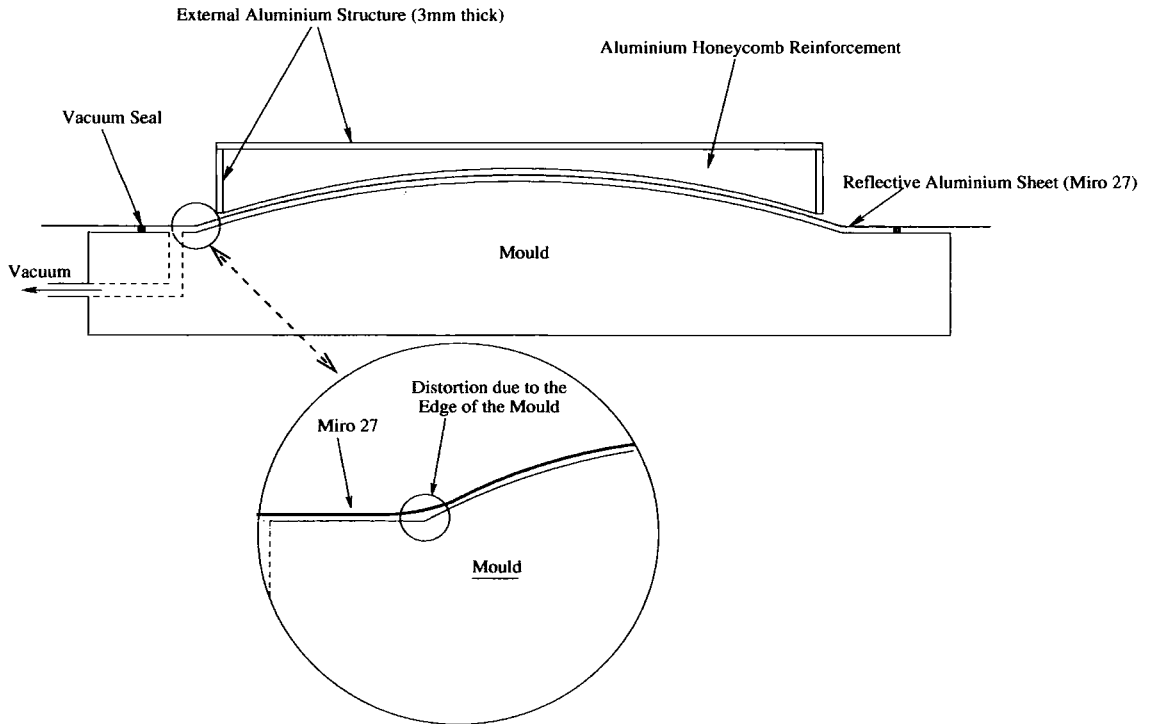


Figure 4.1: Mirror Construction

by using a two stage adhesive process. A first stage has been introduced, which involves a special preparation of the rear surface before construction takes place. This has three advantages

- it effectively increases the thickness of the Miro from the reverse side, making it less prone to print through from the honeycomb
- the preparation is self levelling, giving a stable level surface on which to construct the rest of the mirror.
- no deformation of the honeycomb is required to meet a curved surface

4.3 The Mould

To form the reflective surface into the required spherical shape, the Miro is vacuum formed over a mould. This part of the technique has undergone many evolutions to reach the present stage. The first attempt to produce an accurate

mould was by machining a billet of steel. This was far too inaccurate. Other methods of producing a mould followed and are outlined below.

4.3.1 Fibreglass Resin Moulds

These moulds were constructed by a firm of fibreglass resin specialists, E&F Composites Ltd., who had a vested interest in the technique. E&F have several decades experience of forming specific shapes out of fibreglass resin. The spherical shape of the resin mould was formed by using one of the glass H.E.S.S. mirrors (which has passed all the tests pertaining to shape and radius of curvature). Three moulds were constructed in total to try to achieve a usable shape.

Mould 1 was simply too thin. The mould deformed from sphericity far too easily and this was transferred to the mirror's shape. To combat this, E&F reinforced the underside of the mould using cross bracing but unfortunately this printed through, in much the same way as the honeycomb mentioned previously and was clearly visible on the mirror surface. The surface was also clearly non-spherical as can be seen from Fig.(4.2). Only four mirrors were produced off this mould as they were clearly of very poor quality.

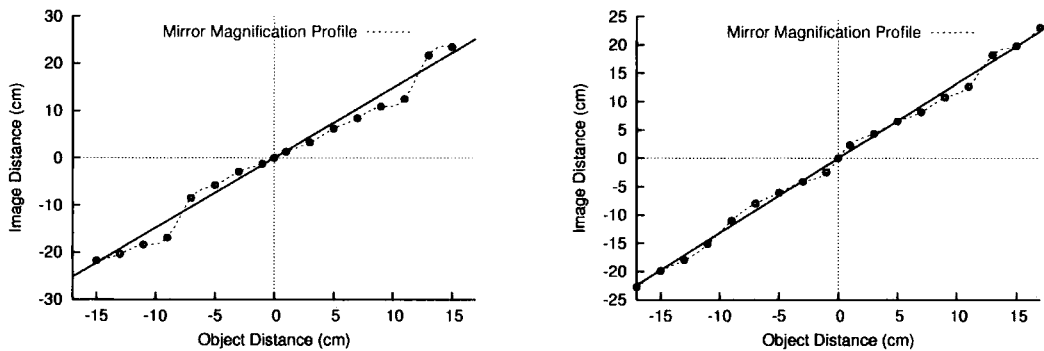


Figure 4.2: Test results for the mirrors on mould 1 in two orthogonal directions. These mirrors should have had a straight line profile, indicating constant magnification across the surface.

Mould 2 was constructed with these problems taken into account; the resin thickness was increased substantially and reinforcing cross bracing added in the mould construction stage, as opposed to an add-on to the finished product. This resulted in a far more stable mould - initially. However this mould too suffered from some critical problems.

The mould showed pitting on its surface after only a few mirrors. This was attributed to dust being trapped between the Miro and mould surface when the vacuum was applied and outgassing of the resin. There was correlation between the pits in the mould and dents on the finished mirror.

The cross bracing still printed through, Fig.(4.3).

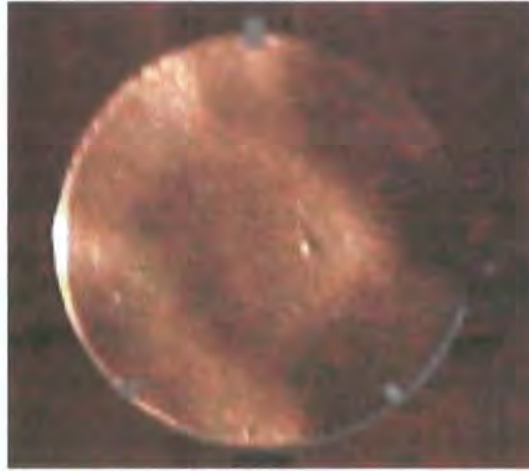


Figure 4.3: Print Through of Cross Bracing from the Mould. (The bright spot just right of centre is a perfect reproduction of a tiny fault in the H.E.S.S. mirror used to form this mould)

The first few mirrors constructed from this mould appeared to have good conformity to the spherical shape, Fig.(4.4). However the radius of curvature (R.O.C.) was 2.25m shorter than that of the H.E.S.S. mirror from which the mould was formed. As more mirrors were constructed it became apparent that the focal length was becoming even shorter. The final mirror had a R.O.C. almost 7m shorter than specification. This relates to a difference in curvature at the edge of $> 100\mu\text{m}$ compared to a H.E.S.S. mirror. To keep within specification this difference can be

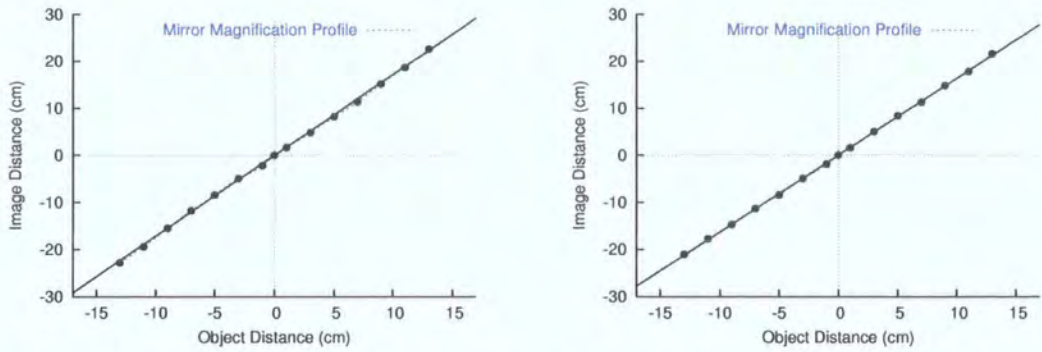


Figure 4.4: Test results for the mirrors on mould 2 in two orthogonal directions. A vast improvement over the mirrors produced from mould 1 is very apparent.

no more than $> 17\mu\text{m}$. E&F attributed this to shrinkage of the mould during the curing phase and during use due to UV damage (the mould was placed in a room that was subject to strong sunshine).

Mould 3 was constructed in a similar manner to Mould 2 using a different resin formula to increase its resistance to pitting damage and UV, and included sand for rigidity rather than cross bracing. A new H.E.S.S. mirror was used as the forming pattern. Again the mirrors produced using

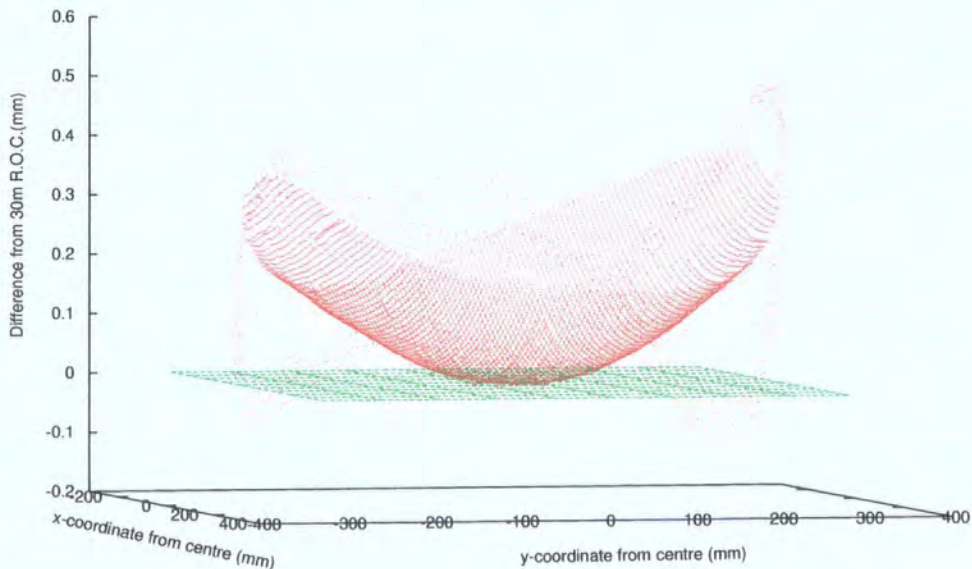


Figure 4.5: Profile difference plot for Mould 3.

this mould were short in focal length. Also apparent was the difference in focal lengths between the inside of the mirror and the outside. To ascertain whether the discrepancies were due to a poorly formed mould, the mould was sent to Mitutoyo who possessed a micron scale accuracy surface profilometer. The profile of the surface was measured and compared to the ideal 30m R.O.C. of 30m (the same as the H.E.S.S. mirror from which the mould was formed). Fig.(4.5) shows the deviation of the mould from the ideal shape (the green plane at $z=0$).

It was decided therefore that the resin moulds would never be accurate or stable enough to achieve the high specification needed and that method for making moulds was rejected.

4.3.2 Aluminium Moulds

After private communication with Dr. David Brooks at the University College London, it was decided to pursue a mould constructed from a solid billet of aluminium alloy. Dr Brooks had several years experience of working with aluminium alloys for astronomical applications, indeed part of his Ph.D. thesis dealt with determining the most suitable alloys. Two contractors were used to try and achieve the accuracy required for the VFT process. Firstly C.A. Models in Stirling, Scotland who could lathe turn the billet and Cranfield Precision, based in the Midlands who had the machinery to diamond turn the billet but at a much greater expense.

C.A.Models is a prototype manufacturing company who have experience in lathe turning precision parts, for example Formula 1 cars. Their method of producing the mould was to lathe turn the aluminium billet to an accuracy of $2\mu\text{m}$ (claimed). A total of 6 mirrors were produced using this mould. Since the tests used to determine the shape of the mirrors taken from previous moulds was no longer sensitive enough to measure these much more precise mirrors, a mirror was sent to H.E.S.S. in Germany for testing. The spot size was also estimated using fairly crude methods and was found to be of the order of 10mm at 30m (2f). However, readily

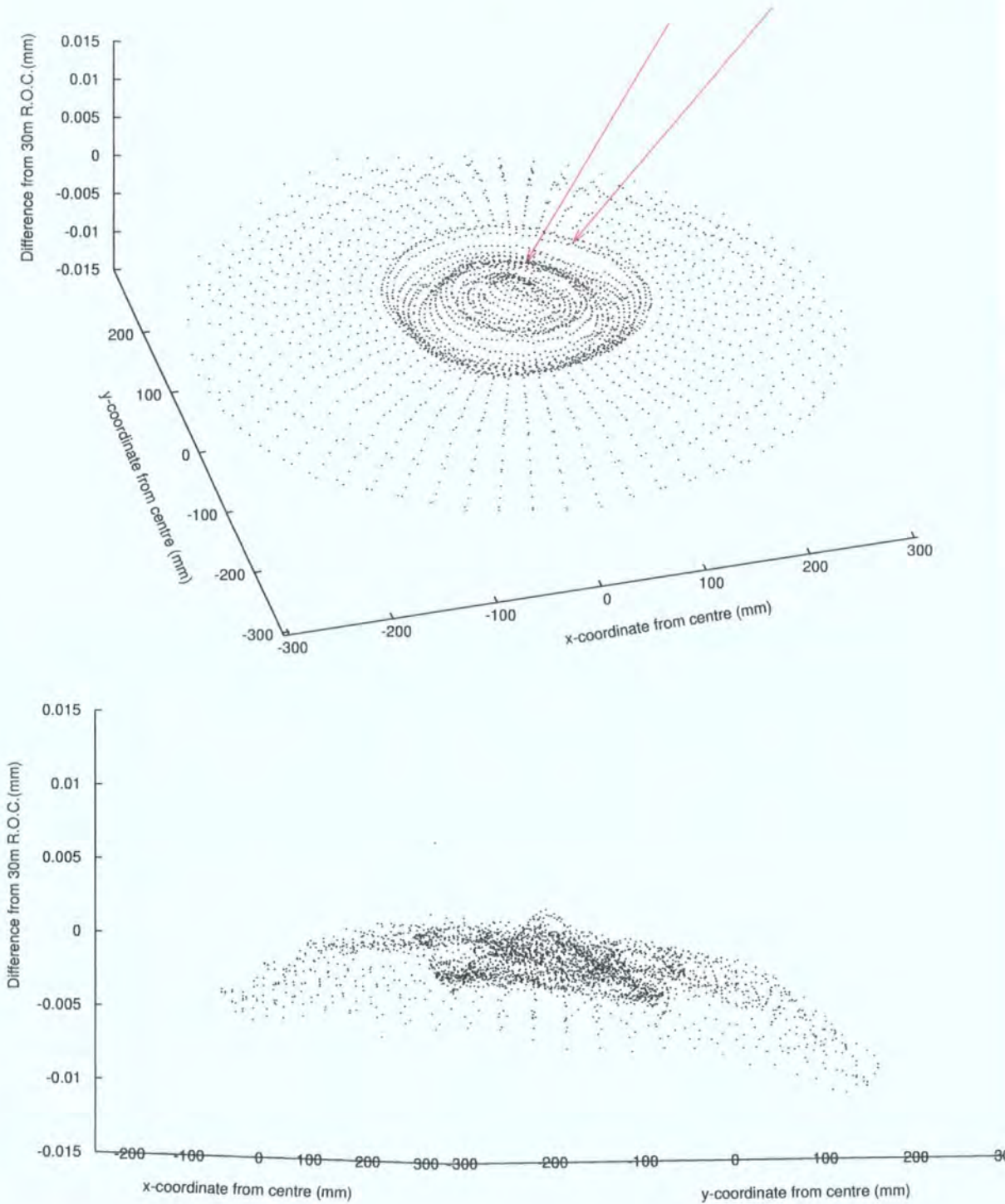


Figure 4.6: Profile difference plot for Mould 3. The two red arrows indicate two, concentric, $5\mu\text{m}$ defects that are apparent on the finished mirrors.

apparent were two concentric circles. Again the mould was measured using a surface profilometer, this time by C.A. Models. The results are shown in Fig.(4.6). The scan clearly shows the defect (indicated by two red arrows), which matches that seen on the mirror. These defects are of the order of $5\mu\text{m}$ indicating a conformity of the mirror to the mould of at least that order. C.A. Models attributed this to having to increase the angular velocity of the lathe to maintain cutting speed as the tool approaches the centre. A 'pip' in the centre is also visible. C.A. Models were unable to improve using the techniques available to them. The tests results from Germany did show a vast improvement over the previous mirrors with a focal length of 13.5m (still outside H.E.S.S. specification) and an 80% light containment of 27mm at 27m. At 30m this increased to 39mm.

Cranfield Precision It was clear from the mirrors produced off the C.A. Models mould that a mould with far smaller surface deviations was required to produce a satisfactory mirror. The only method available to achieve this is diamond milling. Many companies are able to carry out this technique but only Cranfield Precision in the UK have the machinery to do it on such a large scale. The requirements were to produce an aluminium alloy mould with a radius of curvature of 30m, deviating by only $1\mu\text{m}$ over the entire surface, and then nickel plate the surface (we had found that even small specks of dust could leave a pit in the surface of the mould during mirror production). This turned out to be a lengthy process with several attempts being made before an acceptable result was achieved. The mirrors produced from this mould have a consistent focal length and showed no signs of any defects previously seen. Tests at the time of writing are ongoing but preliminary indications are that the mirrors are close to and possibly within specification. All future moulds will be produced by Cranfield Precision using this method.

4.4 Miro 4270 - The Reflective Surface

The mould is responsible for shaping the Miro to the correct sphericity and producing the correct amount of light at a given point with defined dimensions. Meeting the requirements of the H.E.S.S. telescopes as far as reflectivity, diffusivity etc., is totally dependent on the properties of the Miro surface. The criteria for the reflecting surface demands high reflectivity, low diffusivity, good performance in the shorter wavelengths of the spectrum and longevity in outside conditions. Miro is produced by a company called Alanod who have their main headquarters in Ennepetal, Germany. The production of mirrors has concentrated on four variants of Miro - 4270GP, 4270KK, 4270AG and 4270UP, the characteristics of which are given in Table 4.2. Miro's special qualities are

Miro Type	Reflective Surface	Coating	Lacquer
4270GP	Aluminium	SiO ₂ and TiO ₂	No
4270KK	Aluminium	SiO ₂ and TiO ₂	Yes
4270AG	Silver	SiO ₂ and TiO ₂	No
4270UP	Aluminium	SiO ₂ and reduced TiO ₂	No

Table 4.2: Properties of the four variants of Miro 4270

due to a process called Physical Vapour Deposition (PVD). In this process a sheet of aluminium is anodised before a layer of almost pure aluminium (or in the case of 4270AG, silver), is vapour deposited on top. This is covered with a combination layer of SiO₂ and TiO₂ and in the case of 4270KK, a lacquer. Two properties of Miro have to be considered in order to select the best variant, the reflectivity and the longevity.

- Fig.(4.7) [6] shows the differential spectrum of Cherenkov radiation. Since a Cherenkov flash is so fast and faint, it is important to be able to detect the maximum number of photons possible. This means that the reflector needs to operate around the peak of radiation in our atmosphere combined with the response of the camera i.e. the dotted line. This peaks around 340nm. Comparing this with the graph plotted using data supplied by Alanod for the total spectral reflection, Fig.(4.8), it can

be seen that the most suitable Miro surface to use is 4270UP. The others have good performance up to around 400nm after which there is a steep drop off. This is due to absorption in the TiO_2 layer of the top surface.

- The environments in which gamma ray telescopes are generally built are dry, arid and dusty. Miro 4270KK is supplied with a lacquer, which could just as easily be applied to 4270UP. However there are drawbacks to using a lacquered Miro. Firstly there is no doubt that (even on visual inspection) the lacquer causes more diffusion than an unlacquered surface. Secondly the lacquer is about four times less hard than the unlacquered surface (although the lacquer protects against corrosion, it could make it more susceptible to erosion, especially in the Namibian environment). Finally there are some suspicions that tiny air bubbles in the lacquer are outgassing in the vacuum forming process creating small dents in the mirror surface, which are unacceptable.

Without doubt the most suitable surface is the unlacquered Miro 4270UP. For testing the production method 4270GP is used as this is more readily available. A problem that has become apparent with the Miro is the lack of consistency in the quality of the surface between batches. Fig.(4.9) shows the image produced from two mirrors, produced on the same mould and with the same technique but using different batches of 4270GP. There is clearly an elongation and flaring of the spot in the right hand image. This is due to striations in the surface of the Miro produced presumably during the rolling process. It is visibly worse on the second batch used to produce the mirror imaged on the right.

4.5 Mirror Testing

The specification for the H.E.S.S. mirrors as defined in an internal H.E.S.S. document, are

- the angular resolution of each mirror $< 1\text{mrad}$ i.e. diameter of the solid angle that contains 80% of the reflected light

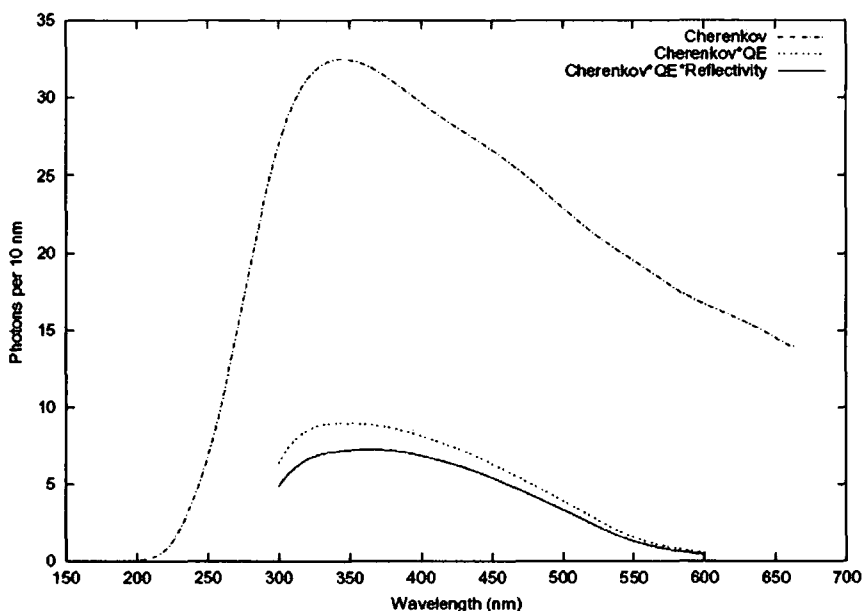


Figure 4.7: The Cherenkov spectrum for a 1TeV gamma-ray entering the atmosphere over the Gamsberg Plateau, Namibia.[6]. The dash-dotted line is produced using MOCCA simulations, the turnover at shorter wavelengths being due to absorption by ozone and Rayleigh and Mie scattering. The dotted line is the Cherenkov spectrum combined with the quantum efficiency of the photomultiplier tubes used in the camera. The solid line also includes the reflectivity of the current H.E.S.S. glass mirrors.

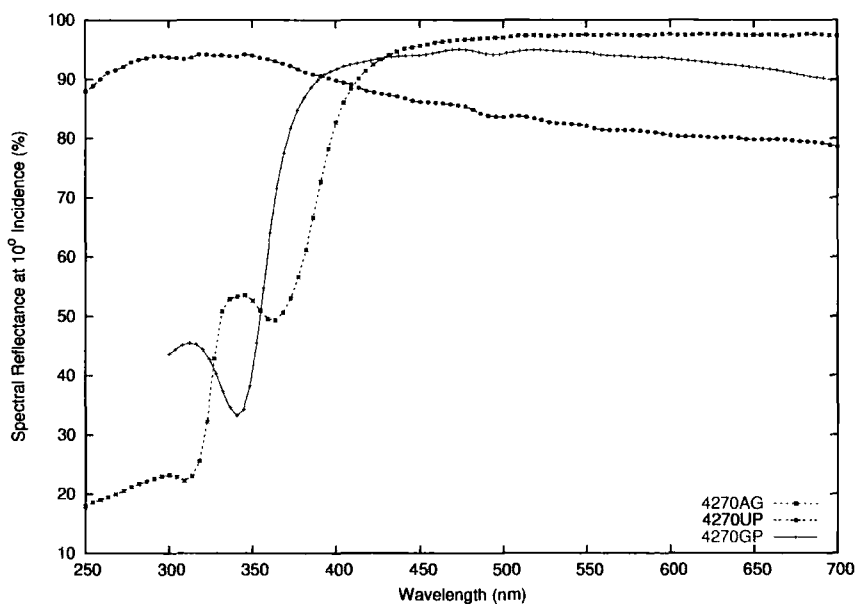


Figure 4.8: Total Spectral Reflectance of Miro 4270. (Data courtesy of Alanod Ltd.)

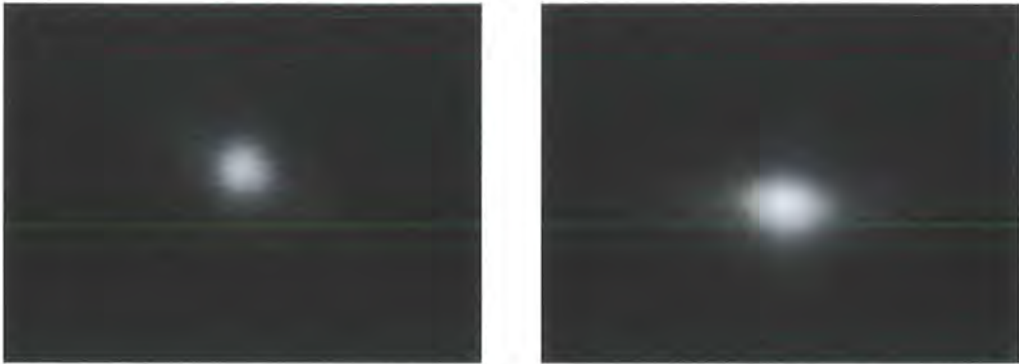


Figure 4.9: Quality difference between two different batches of Miro. The spot size is $\sim 25\text{mm}$ across the minor axis in both cases. The right hand batch clearly shows more flaring in one direction.

- focal length deviation from the mean value (15m) of less than 250mm
- high specular reflectivity $>80\%$ between 300nm and 600nm, although for regions mentioned previously the shorter wavelengths are more important. At present only reflectivity data from Alanod is available and has been presented. Independent measurements will be made in the future.
- the performance of the mirrors should not deteriorate over the lifetime of the experiment. This is already not being satisfied by the current glass mirrors as the first equipped telescope is now at a point where the mirrors need replacing. Several pieces of Miro have been placed at the H.E.S.S. site for over a year. These will shortly undergo reflectivity test for comparison with new Miro.

The first two items ensure that the angular resolution of the telescope is dominated by the Davies Cotton design and mirror adjustment and not by the properties of the individual mirror tiles.

To check the focal length and angular resolution of the mirrors, a small diameter light source needs to be placed at $2f$, the image then being measured at the same point. There are obvious logistical problems with this. At present the only 30m+ optical bench testing equipment is at Max-Planck Institute für Kernphysik. In order to get a general indication of the performance compared

to a glass H.E.S.S. mirror, different methods to check the sphericity and focal length of the mirrors have been used. Methodology has changed as the quality of the mirrors has improved and the sensitivity of the tests becomes too low. It must be stressed that these methods are not optical tests as such but merely indicative of mirror development progression.

The first test was initially used to provide an indication of sphericity. Fig.(4.10) shows a schematic of the method. It was used only on the first fibreglass moulds and the graphs shown in Figs. (4.2) and (4.4) result from this test. A travelling

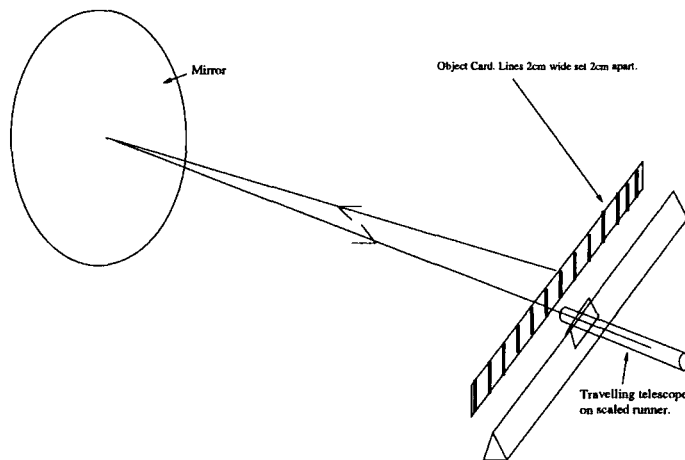


Figure 4.10: Method for Initial Indication of Shape Conformity

telescope is mounted at 90° to its optical rail. Due to space restrictions the mirror mount is placed at a distance of approximately 7m parallel to the rail as in Fig.(4.10). When the mirror is mounted, it is moved laterally, vertically and rotationally until the centre of the mirror is in the centre of the telescope eyepiece and, more importantly, does not move from this point under mirror rotation. This method ensures that the mirror-telescope system is optically aligned. Above the telescope is a stationary object. This consists of a banner which stretches along the length of the rail, on which are 2cm wide vertical lines, set 2cm apart. The principle behind this test is if the mirror is spherical, then as the telescope is moved side to side across the mirror, the reflected image of each line will be a constant distance apart and of a constant width. It basically confirms that the magnification remains constant across the mirror, as expected if the mirror were spherical.

This test was used until the errors were larger than any measurable deformity in the sphericity of the mirror.

The second test was introduced as an interim between the former and a rigorous optical test. To perform this, a 30m+ long, dark area is required. The only place locally which meets this criterion is the armory room of a local castle! This method involved measuring the comparative spotsize of the image of a light source placed at the centre of curvature. Such an object has its image at the same point but inverted. The H.E.S.S. mirror was measured first, acting as the standard. Although there is nothing to measure accurately with this test, it does provide some valuable comparative information. Firstly the focal length of the mirror can be deduced by moving the image screen back and forth to gain the smallest, most focused image. The light source is then moved and the process repeated until the two coincide. This point is then the centre of curvature of the mirror and its focal length half that distance. For the H.E.S.S. mirror this coincided approximately with 30m. However for the aluminium mirrors, it proved to be substantially lower, indicating the wrong sphericity. Secondly by lowering the intensity of the light source, the actual shape of the deformities could be seen visually. This method can be used until it becomes necessary to progress to more stringent tests.

A new test rig is currently being constructed. Since the mirrors being produced off the Cranfield precision mould are now coming close to the H.E.S.S. specification a more rigorous test is required. This will consist of a TAOS TSL1410R linear sensor array, containing 1280 photodiodes. This array, which will give a resolution of 400DPI, will be scanned across the reflected image of a high power, red l.e.d. that illuminates the mirror through a 3mm diaphragm. This will allow accurate measurement of both the focal length and the angular resolution of the mirrors and will be the definitive test.

4.6 Summary

At the time of writing the new test rig has been commissioned, although the associated software is still undergoing refinement. The results clearly show the directional flaring of the spotsize in one axis as described in Section 4.4.

When compared to the spotsizes from a H.E.S.S. glass mirror, the vast difference in quality is immediately apparent, conclusively showing that Alanod is not suitable for H.E.S.S. telescope mirrors. A new material for the reflective surface is currently being sourced. The preferred material will be a sheet of aluminium that will be highly polished to remove the rolling grain seen in the Alanod, which is responsible for the flaring. The individual sheets will then be coated with a highly reflective and protective film before being used to produce a mirror using the same method described in this chapter.

A new 1.2m diameter mould has also been commissioned. This will have a surface figure suitable for the H.E.S.S. Phase II telescope i.e. 73m radius of curvature. Hexagonal mirrors, 900mm point to point with a spherical profile, will be produced from this mould. A prototype is expected to be produced by September 2006. Concurrently the existing mould will be used to perfect the shorter focal length mirrors, required as a replacement for the glass mirrors on the Phase I telescopes.

Chapter 5

Conclusions and Future Work

5.1 Synchrotron Self-Compton Model

In this thesis a code based on a model originally designed for AGN has been produced. The code was tested on the blazar 3C 279 to which this particular model had already been applied [78], and a good fit with data was found. The code was then applied to three black hole microquasars with the hypothesis that microquasar jets are scaled down versions of AGN jets. A method for scaling the jets was described and SEDs produced, including H.E.S.S. observation upper limits. For GRS 1915+105 a comparison with data taken whilst it was in the LS [35] was made, which showed a poor fit.

In order to extend this work in the future there are several paths that can be followed.

- If the analogy between AGN jets and microquasar jets is to be maintained, the scale-invariant jet concept would need closer investigation in order to see what other properties need to be taken into account to make it more robust and achieve a better fit.
- An alternative method is to ignore the scale-invariant hypothesis and use parameters derived purely from observations. If a fit is achieved using SSC only (which may not be possible), then a scaling connection between those parameters and the parameters used for 3C 279 may be observed. The dependency on any free parameters can also be investigated.

5. 5.2. LS5039 - First Microquasar detected at VHE Energies?

- The SSC code is written in a way that the jet can be separated into two smoothly adjoining sections. Parameters such as the magnetic field energy to the particle energy densities can be different in each section. This again allows more degrees of freedom for parameter choice and a more flexible code.
- Microquasars, especially those that are HMXBs may have jets that interact very strongly with an external photon field. External comptonisation may then be the dominant process which may not be the case in some AGN [41]. The code can be further expanded to introduce this photon field.

5.2 LS5039 - First Microquasar detected at VHE Energies?

LS5039 is a high mass X-ray binary, lying close to the Galactic plane, containing an O7V spectral type star and an as yet undetermined compact object, although a recent study suggests a black hole [19]. Previous work shows that it has a highly eccentric, short period orbit [73] and that accretion is likely to be by stellar wind capture as oppose to Roche lobe overflow [74]. Radio frequency studies have indicated that LS5039, which lies within the 95% confidence contour of the EGRET source 3EG J1824-1514, has persistent radio jets rather than the more common transient type [92] [93].

In the summer of 2004 all four telescopes of the H.E.S.S. Phase I array were used to undertake a galactic scan to search for new sources of VHE γ -rays. The result of 112 hours of observations revealed eight previously unknown VHE γ -ray sources at level $> 6\sigma$ [4]. After quality selection of data a total of 10.5 hours of these observations were found to cover the position of the microquasar LS5039.

The results presented [5] were analysed using a semi-analytical shower model [88] as opposed to the Hillas method described in Chapter 3 although the results from both methods are in excellent agreement. The reconstructed γ -ray sky map of the results shows an excess 1° southwest of the new galactic scan

5. 5.2. LS5039 - First Microquasar detected at VHE Energies?

source HESS J1825-137 with significance greater than 7σ . The best position

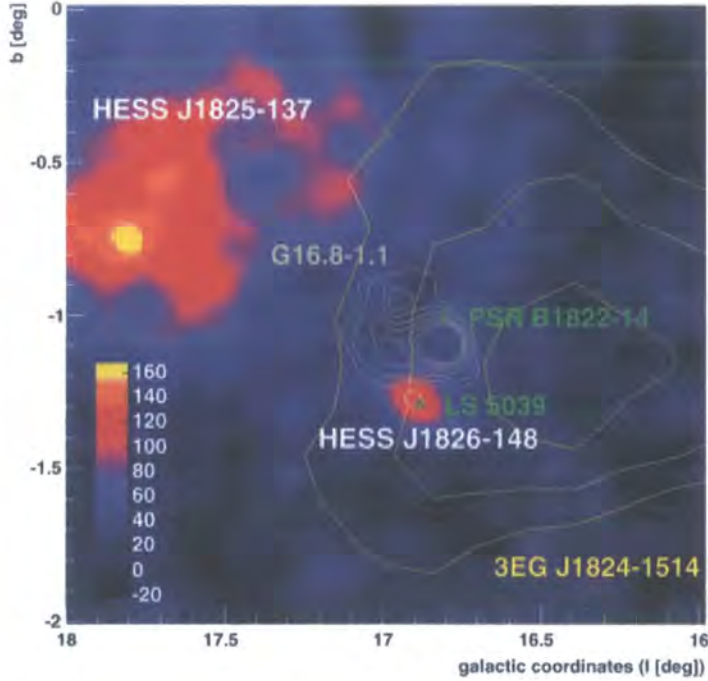


Figure 5.1:

of this source, denoted HESS J1826-148, is R.A. 18h26m15s Dec.-14°49'30" with statistical and systematic uncertainties of ± 32 and ± 30 arc seconds respectively. This will be improved with further on-source observations.

The SSC model described in this thesis is not applicable to LS5039; because of its HMXB (see Section 2.1) nature the optical and UV spectra will be dominated by the O7V star and accretion rather than any synchrotron radiation from a jet. Also the inverse Compton component, will have a significant, if not dominant, contribution from the upscattering of stellar photons. It is possible to fit a spectrum using the SSC model to the EGRET data using some of the parameters derived from radio observations [92] [93] as demonstrated in [67], Fig.(5.3), but this fit produces a high energy cut-off at ~ 25 GeV, and so does not fit the H.E.S.S. data, and provides no fit at lower frequencies.

5. 5.2. LS5039 - First Microquasar detected at VHE Energies?

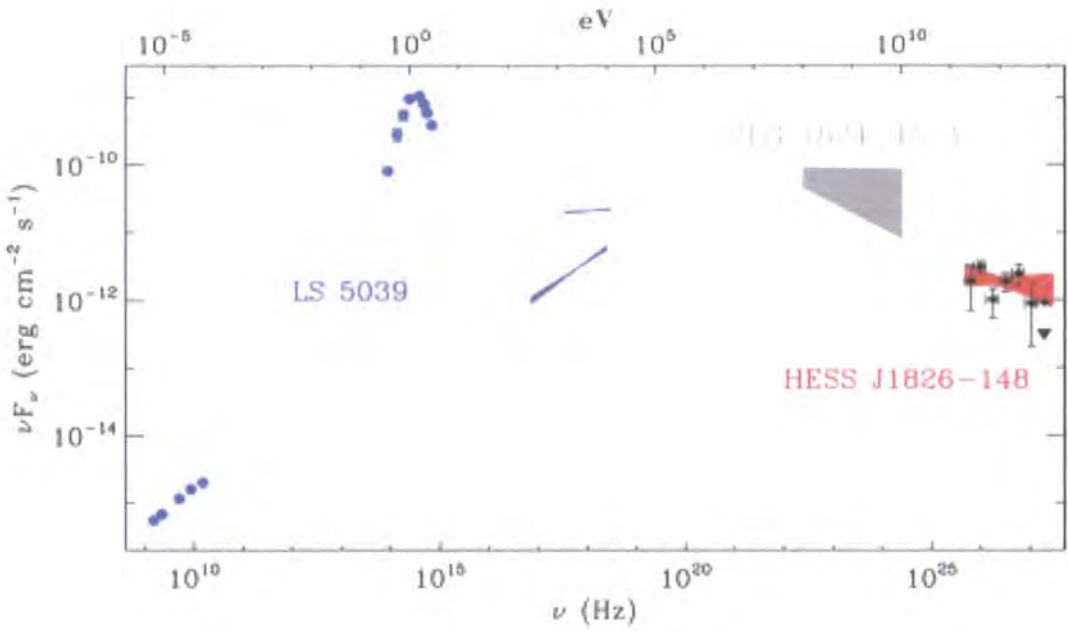


Figure 5.2:

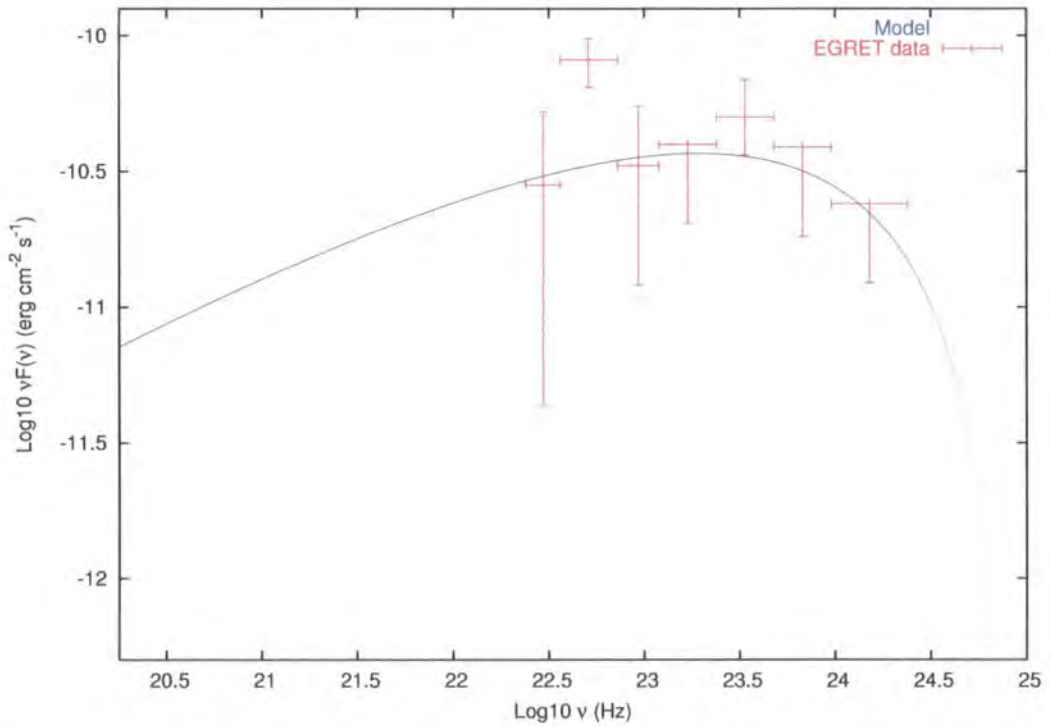


Figure 5.3: Synchrotron self-Compton model applied to fit EGRET data on LS5039 [17].

5.3 Further Observations

5.3.1 IGR J19140+0951

In Chapter 3 H.E.S.S. Phase I data were presented for four microquasars, GRS 1915+105, Circinus X-1, V4641 Sgr and GX 339-4. No signal was detected from any of these microquasars. Consequently upper limits were produced based on these observations.

However, in the field of view of GRS 1915+105 a $\sim 4\sigma$ ‘hot spot’ was detected, which is coincident with the INTEGRAL source IGR J19140+0951, an x-ray binary. The observation runs used in the analysis of GRS 1915+105, have recently been re-analysed with a source offset included for a specific analysis of IGR J19140+0951. Using the cuts defined in Table 3.1, the number of events are $N_{on} = 588$, $N_{off} = 3536$ with a normalisation factor of 0.141 leading to an excess of 91γ and a detection significance of 3.7σ . Fig.(5.4) shows the significance sky plot (left) and the θ^2 plot for these results. The θ^2 plot shows a definite increase in events at small values of θ^2 as would be expected from a γ -ray source. The significance at which IGR J19140+0951 has been detected

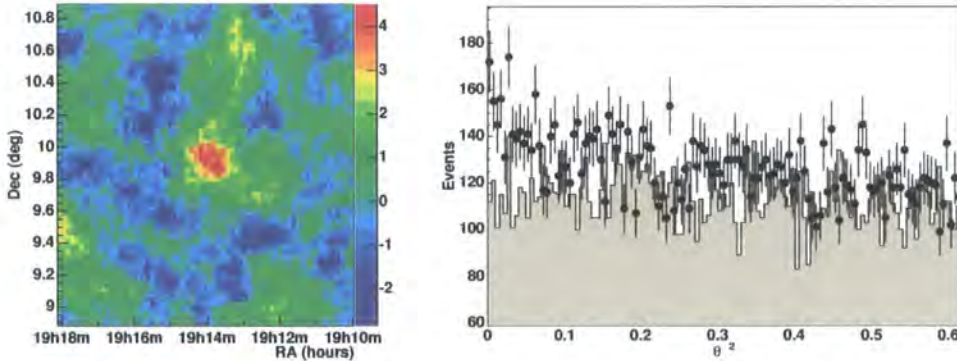


Figure 5.4: Analysis results for IGR J19140+0951. On the left is the 2-d significance sky map centred on IGR J19140+0951. On the right is the θ^2 plot showing an increase in events at small values of θ^2 , which is indicative of a γ -ray source.

with these observations is below the 5σ level, which would define it as a VHE γ -ray source. Consequently, a proposal has been drafted to observe this object for

a further 10 hours with H.E.S.S., which should confirm or refute this detection. The correlation with the INTEGRAL position can also be confirmed.

5.3.2 Microquasars

In addition to the proposal above, a further proposal has been presented to H.E.S.S. to perform an x-ray binary/microquasar survey. This proposal includes the four microquasars that have been investigated in this thesis.

5.4 H.E.S.S. Phase II

5.4.1 Introduction

Since the last of the four telescopes of Phase I was commissioned at the end of 2003, H.E.S.S. has been a great success, detecting around twenty γ -ray sources with a much higher significance than previously attained. Amongst them new galactic sources [4] and the first significant detection of the microquasar LS5039 at VHE γ -rays [5]. As a natural development of this success, two options were available to H.E.S.S.

The first is to expand the array by adding more telescopes, similar to those in Phase I, thus increasing the sensitivity at the current energy threshold of around 100 GeV. Not only would this allow observations of lower flux sources at very high energies, but several objects could be observed simultaneously using different groups of four telescopes, effectively having two or three Phase I arrays.

The second option, and the one adopted for H.E.S.S. Phase II, is to increase the energy range detectable by the array, and in particular lower the energy threshold. This is particularly important as it not only allows detection of sources emitting at lower energies but also closes the missing energy gap between the detection upper limits of current satellite experiments and the lower energy threshold of ground based experiments. This can be achieved by the addition of a single much larger telescope to the existing array, which would also increase the sensitivity of the array in the current energy range. Since

the Northern hemisphere already has a telescope operating at a low energy thresholds i.e. MAGIC, this option would provide a complementary instrument operating in the Southern hemisphere where, at present, H.E.S.S. Phase I has the lowest energy threshold.

There are many scientific reasons why this second option is attractive. The recent discovery of a number of unidentified sources at high energies in the inner regions of the galaxy, have no obvious counterparts at other wavelengths. A wider energy range could help to understand and identify these objects. The lower energy threshold of 20 GeV, which will be provided by the current design will mean the array has access to objects at redshifts of the order of unity, which will allow the study of the cosmological infrared background and also investigate gamma-ray bursts. In addition, the lower energy threshold will provide a wider energy spectrum of those sources already detected at the higher energy threshold such as LS5039, providing a better understanding of the processes involved.

5.4.2 The H.E.S.S. Phase II Design

A single telescope, much larger than the current telescopes, will be situated at the centre of the Phase I array [106].

The dish, which will be parabolic as opposed to the Davies-Cotton design



Figure 5.5: An impression of the H.E.S.S. Phase II telescope placed in the centre of the existing Phase I array (image courtesy of the H.E.S.S. Collaboration).

previously used, will be rectangular in shape, 32 m high and 24 m wide, giving a mirror area of 596 m², which is larger than all four Phase I telescopes combined. The parabolic shape, while having a narrower field of view, will allow far more detailed studies of the time variability of sources. The dish, which will hold 850 hexagonal, 90 cm mirror facets, will be supported by two towers 24 m above the ground. Each mirror facet will be supported by a system that allows alignment of each individual mirror.

The camera will follow the same design principles as the Phase I telescope cameras but will consist of 2048 photomultiplier tubes and have an updated trigger and readout system, designed to cope with the higher trigger rate.

The construction of the Phase II telescope is already underway and is expected to be operational by the end of 2008.

Appendix A

Synchrotron Self-Compton Code

A.1 Synchrotron Self-Compton Code

```
PROGRAM MAIN
IMPLICIT NONE

DOUBLE PRECISION C,EMASS,CHARGE,PI,KO1,B01,KO2,B02,EPSIL,N1,N2,M1,
& M2,E1,E2,NU,G1,G2,THETA,r0,RZERO,LOLOR1,XMAX,DIS,
& ALPHA,DEG,EPS,X1IN,X2IN,X1OUT,X2OUT,XMID,LOLOR2,
& LOWLIM,UPLIM,INTFOR,INTPOS,INTFUL,INTRES,SYNCL,
& EMISS,ETA,NUA01,NUA02,NUMX01,NUMX02,NUMXX1,
& NUMXX2,KSUBM,FIRST,SECOND,BOT,TOP,NUAO,NUMAXO,
& NUMAXX,XMIN,AX,BX,CX,LOWDX,NUTOP1,NUTOP2,GOLDEN,
& ICLUM,IICRES,IICFOR,IICPOS,NUIC,NUAMX1,NUAMX2,
& IICFUL,AICA,TAU,NUABS,NUAMD,NUMXMD,C1,LOCLOR,
& X11,X12,X21,X22,ICUP,ICLO,DIST,SYNCF,NSYNCF,
& ICFL,NICFL,NSYNCL,NICLUM,ETAU1,ETAU2,SIGT,
& TOL,FA,FB,FC,MAXMA1,MAXMA2,STEP,GM,INUA01,INUA02,
& INUMX1,INUMX2,KNO1,DELTA,XKNO1,XKNO2,CUTOFF,NMX21,
& ,NMX22

INTEGER I

EXTERNAL ETA,KSUBM,LOWLIM,UPLIM,EMISS,NUAO,NUMAXO,NUMAXX,CUTOFF,
& AICA,TAU,NUABS,C1,LOCLOR,ICUP,ICLO,LOWDX,GOLDEN,DELTA

CHARACTER STR1*10,STR2*7,STR3*4

-----
c Initialise some of the variables. All are in Cgs units.
-----

C = 2.9979D+10           !Speed of Light
EMASS = 9.1094D-28      !Electron Mass
CHARGE = 4.8032D-10     !Electron Charge
PI = 4.0D0*DATAN(1.0D0) !Pi
KO1 = 1.50D+6           !Electron Density Parameter at R0
B01 = 8.0D0             !Magnetic Field at R0
EPSIL = 0.5D0          !Controls jet geometry-parabola<1,truncated cone=
N1 = 1.5D0             !Power law variable for K0(1st & 2nd stages)
N2 = 1.5D0
M1 = 1.0D0             !Power Law variable for B0.(1st & 2nd stages)
```

A.

A.1. Synchrotron Self-Compton Code

```

M2 = 1.0D0
E1 = 0.5D0                !Power Law variable for LOLOR(1st & 2nd stages)
E2 = 0.5D0
G1 = 0.2D0                !Power Law variable for GM (1st & 2nd stages)
G2 = 0.2D0 !!!Don't make G1 and G2 different if this comment line exists
r0 = 2.0D+15              !Radius of the base of the jet
RZERO = 2.0D+15           !Distance to the base of the jet
LOLOR1 = 1.3365D+4        !Local Lorentz factor at R0
XMIN = 1.001D0           !Base of the jet
XMID = 50.0D0            !2nd stage point of the jet
XMAX = 2.0D+3            !Maximum extent of the jet
GM = 5.5D0               !Bulk Lorentz factor at R0
SIGT = 6.6525D-25        !Thomson scattering cross section
TOL = 1.0D-6             !Tolerance used in functions

```

```

c IMPORTANT NOTE. N1,M1,E1... SHOULD NEVER BE BIGGER THAN N2,M2,E2...
c If this scenario is required extra coding would be needed in the main program

```

```

PRINT *, ''
PRINT *, 'What is the name of the output file (10 char. max.)'
READ *, STR1

PRINT *, ''
PRINT *, '-----'
PRINT *, 'To calculate the Synchrotron and Inverse Compton luminos
&ity and flux, some initial values need to be entered. (Double Prec
&ision format must be used e.g. 1.0D+6, 0.5D0 etc)'
PRINT *, '-----'
PRINT *, ''

PRINT *, 'Enter the distance to the object (in kpc)'
READ *, DIST
PRINT *, ''

PRINT *, 'Enter a value for ALPHA'
READ *, ALPHA
PRINT *, ''

PRINT *, 'Enter the angle of the jet to the observer (1-89 deg.)'
READ *, DEG
PRINT *, ''

PRINT *, 'To what accuracy do you want to integrate e.g. 1.0D-6'
READ *, EPS
PRINT *, ''

```

```

c----- Assign some constants to be used.-----
      THETA = DEG/180.0D0*PI !The angle to the line of sight (radians)

      DIS = DIST*3.085678D+21 !The distance to the object (cm)

```

```

c The electron density parameter and magnetic field at r0 which relates to the
c values for N2,M2 is given by K02 and B02. NUA0*, NUMX0*, NUMXX* are the
c analogous functions for the self absorption frequency at r0, the maximum
c synchrotron frequency at r0 and the maximum synchrotron frequency at xmax.
c These are needed to calculate the upper and lower limits of the integration
c for the the two separate parts of the jet.
c This provides continuity for the solutions at the switch between r0<x<xmid
c and xmid<x<xmax.

```

A.

A.1. Synchrotron Self-Compton Code

```

K02 = K01*XMID**(-1.0D0*EPSIL*(N1-N2))
B02 = B01*XMID**(-1.0D0*EPSIL*(M1-M2))
LOLOR2 = LOLOR1*XMID**(-1.0D0*EPSIL*(E1-E2))
c -----
c This part calculates the electron scattering optical depth used in the
c calculations for the inverse compton luminosity.
    ETAU1 = SIGT*r0*K01
    ETAU2 = SIGT*r0*K02
c -----
c This section calculates the self-absorption frequencies and the maximum
c synchrotron frequencies for the base of the jet, the mid-point of the jet
c and the maximum extension of the jet.
c Self-absorption! Intrinsic
    INUA01 = NUA0(ALPHA,EMASS,CHARGE,C,K01,B01,r0,THETA) ! Intrinsic
    INUA02 = NUA0(ALPHA,EMASS,CHARGE,C,K02,B02,r0,THETA) ! Intrinsic
    NUA01 = NUABS(INUA01,1.0D0,EPSIL,N1,M1,G1,ALPHA,THETA,GM) ! Doppler Boosted
    NUA02 = NUABS(INUA02,1.0D0,EPSIL,N2,M2,G2,ALPHA,THETA,GM) ! Doppler Boosted
    NUAMD = NUABS(INUA01,XMID,EPSIL,N1,M1,G1,ALPHA,THETA,GM) ! Doppler Boosted
    NUAMX1 = NUABS(INUA01,XMAX,EPSIL,N1,M1,G1,ALPHA,THETA,GM) ! Doppler Boosted
    NUAMX2 = NUABS(INUA02,XMAX,EPSIL,N2,M2,G2,ALPHA,THETA,GM) ! Doppler Boosted
c -----
c Maximum synchrotron
    INUMX1 = NUMAX0(C,CHARGE,EMASS,LOLOR1,B01) ! Intrinsic
    INUMX2 = NUMAX0(C,CHARGE,EMASS,LOLOR2,B02) ! Intrinsic
    NUMX01 = NUMAXX(1.0D0,INUMX1,EPSIL,E1,M1,G1,THETA,GM) ! Doppler Boosted
    NUMX02 = NUMAXX(1.0D0,INUMX2,EPSIL,E2,M2,G2,THETA,GM) ! Doppler Boosted
    NUMXMD = NUMAXX(XMID,INUMX1,EPSIL,E1,M1,G1,THETA,GM) ! Doppler Boosted
    NUMXX1 = NUMAXX(XMAX,INUMX1,EPSIL,E1,M1,G1,THETA,GM) ! Doppler Boosted
    NUMXX2 = NUMAXX(XMAX,INUMX2,EPSIL,E2,M2,G2,THETA,GM) ! Doppler Boosted
c ----- Open the output files-----
c The program creates two output files. The named output file (Synchrotron
c luminosity data)and the named output file appended by 'Inverse'(Synchrotron
c Self-Compton luminosity data).
    STR2='Inverse'
    STR3='Data'
    I=INDEX(STR1,' ')
    OPEN (UNIT =8, FILE=STR1(1:I-1), STATUS='NEW')
    OPEN (UNIT =9, FILE=STR1(1:I-1)//STR2, STATUS='NEW')
    OPEN (UNIT=10, FILE=STR1(1:I-1)//STR3, STATUS='NEW')
c -----
c This part prints out to screen and to the 'Data' file, the values of

```

A.

A.1. Synchrotron Self-Compton Code

c the synchrtron self-absorption and maximum synchrotron frequencies at
c different parts of the jet.

```

PRINT *, ''
WRITE (10,*) ''
PRINT *, 'Self-absorption Frequency Values'
WRITE (10,*) 'Self-absorption Frequency Values'
PRINT *, '-----'
WRITE (10,*) '-----'
PRINT *, 'r0 (jet1) - ',NUAO1
WRITE (10,*) 'r0 (jet1) - ',NUAO1
PRINT *, 'r0 (jet2) - ',NUAO2
WRITE (10,*) 'r0 (jet2) - ',NUAO2
PRINT *, 'XMID - ',NUAMD
WRITE (10,*) 'XMID - ',NUAMD
PRINT *, 'XMAX (jet1) - ',NUAMX1
WRITE (10,*) 'XMAX (jet1) - ',NUAMX1
PRINT *, 'XMAX (jet2) - ',NUAMX2
WRITE (10,*) 'XMAX (jet2) - ',NUAMX2
PRINT *, ''
WRITE (10,*) ''
PRINT *, 'Maximum Synchrotron Frequency Values'
WRITE (10,*) 'Maximum Synchrotron Frequency Values'
PRINT *, '-----'
WRITE (10,*) '-----'
PRINT *, 'r0 (jet1) - ',NUMX01
WRITE (10,*) 'r0 (jet1) - ',NUMX01
PRINT *, 'r0 (jet2) - ',NUMX02
WRITE (10,*) 'r0 (jet2) - ',NUMX02
PRINT *, 'XMID - ',NUMXMD
WRITE (10,*) 'XMID - ',NUMXMD
PRINT *, 'XMAX (jet1) - ',NUMXX1
WRITE (10,*) 'XMAX (jet1) - ',NUMXX1
PRINT *, 'XMAX (jet2) - ',NUMXX2
WRITE (10,*) 'XMAX (jet2) - ',NUMXX2
PRINT *, ''
WRITE (10,*) ''
PAUSE

```

C -----
C This part calculates the Klein_nishina cutoff frequency based on a step
c function at $\gamma E/mc^2=1$ (doppler boosted), prints it to screen and
c writes it to the 'Data' file.

```

KN01 = (EMASS*C**2.0D0/(LOLOR1*6.6261D-27))
& *DELTA(1.0d0,G1,THETA,GM)
PRINT *, 'The Klein-Nishina cut of frequency is ',KN01
PRINT *, ''
WRITE (10,*) 'The Klein-Nishina cut of frequency is ',KN01
WRITE (10,*) ''
PAUSE

```

C -----
C -----NEW CODE-----
C -----

c First for LOWLIM need to find the maxima of $x^{**k} \text{subm} \cdot \delta$, if it exists.
c This is done firstly by bracketing the minima using LOW3BK and then using
c these brackets in GOLDEN which returns the max. This x,LOWMAX, is then used to
c calculate the self-absorption frequency at that value. All frequencies

A.

A.1. Synchrotron Self-Compton Code

```

c above that have x1 = XMIN. All frequencies below NUABS0 use function LOWLIM
c to calculate x1. All frequencies in between have two solutions, between
c which there is no emission.
c LOWDX calculates the gradient of x**-ksubm at x= xmin
      IF (LOWDX(XMIN,EPSIL,N1,M1,ALPHA,G1,THETA,GM).GT.0.0D0) THEN
      PRINT *, 'The gradient of x**-k_{m] at x=xmin is',
&      PRINT *, 'LOWDX(XMIN,EPSIL,N1,M1,ALPHA,G1,THETA,GM)
      WRITE (10,*), 'The gradient of x**-k_{m] at x=xmin is',
&      PRINT *, 'LOWDX(XMIN,EPSIL,N1,M1,ALPHA,G1,THETA,GM)
      WRITE (10,*) ''

C WHAT IF LOWDX(XMAX)>0.0D0?
c The minimum of -f(x) is found for both Jet1 and Jet2, as this = max f(x)
c -----
c Jet1
c -----
      AX = XMIN
      BX = XMIN+0.001D0

c This subroutine brackets the minimum with AX, BX, CX
      CALL LOW3BK(AX,BX,CX,FA,FB,FC,EPSIL,INUA01,N1,M1,ALPHA,G1,
&      THETA,GM)

c      PRINT *, AX,BX,CX,FA,FB,FC
c      PRINT *, ''
c      WRITE (10,*) AX,BX,CX,FA,FB,FC
c      WRITE (10,*) ''

c This function calculates the maximum of x**-ksubm*delta and returns
c both the x value, LOWMAX and the function value, GOLDEN
      NUTOP1 = GOLDEN(AX,BX,CX,TOL,MAXMA1,EPSIL,INUA01,N1,M1,ALPHA,G1,
&      THETA,GM)*(-1.0d0)

      PRINT *, NUTOP1,MAXMA1
      PRINT *, ''
      WRITE (10,*) NUTOP1,MAXMA1
      WRITE (10,*) ''

c Jet2
c -----
      AX = XMIN
      BX = XMIN+0.001D0

c This subroutine brackets the minimum with AX, BX, CX
      CALL LOW3BK(AX,BX,CX,FA,FB,FC,EPSIL,INUA02,N2,M2,ALPHA,G2,
&      THETA,GM)

      PRINT *, AX,BX,CX,FA,FB,FC
      PRINT *, ''
      WRITE (10,*) AX,BX,CX,FA,FB,FC
      WRITE (10,*) ''

c This function calculates the maximum of x**-ksubm*delta and returns
c both the x value, LOWMAX and the function value, GOLDEN
      NUTOP2 = GOLDEN(AX,BX,CX,TOL,MAXMA2,EPSIL,INUA02,N2,M2,ALPHA,G2,
&      THETA,GM)*(-1.0d0)

      PRINT *, NUTOP2,MAXMA2

```

A.

A.1. Synchrotron Self-Compton Code

```
      ENDIF
      PAUSE

c -----
c -----END OF NEW CODE-----
c -----

c The first part calculates the Synchrotron Luminosity
c The value of the Integration is first calculated for the case
c where the limits span the entire jet. This prevents having to call the
c integration routine every time NU is changed but the limits stay the same.

      STEP = 1.01D0
      NU = NUMX01/1.01

      CALL RES(XMIN,XMID,EPS,INTRES,EPSIL,N1,M1,G1,THETA,GM,ALPHA)
      INTFOR = INTRES
      CALL RES(XMID,XMAX,EPS,INTRES,EPSIL,N2,M2,G2,THETA,GM,ALPHA)
      INTPOS = INTRES

      DO WHILE (X1IN.LE.XMID)
      X1IN = LOWLIM(XMIN,XMAX,NU,INUA01,NUA01,EPSIL,N1,M1,G1,
&                THETA,GM,ALPHA)
      X1OUT = LOWLIM(XMIN,XMAX,NU,INUA02,NUA02,EPSIL,N2,M2,G2,
&                THETA,GM,ALPHA)
      X2IN = UPLIM(XMIN,XMAX,NU,INUMX1,NUMX01,NUMXX1,EPSIL,E1,M1,G1,
&                THETA,GM)
      X2OUT = UPLIM(XMIN,XMAX,NU,INUMX2,NUMX02,NUMXX2,EPSIL,E2,M2,G2,
&                THETA,GM)
      IF (X1IN.EQ.XMIN.AND.X2OUT.EQ.XMAX) THEN
      SYNCL = 4.0D0*(PI**2.0D0)*(EMISS(K01,B01,ALPHA,NU,EMASS,CHARGE,C)
& *INTFOR+EMISS(K02,B02,ALPHA,NU,EMASS,CHARGE,C)*INTPOS)
& *RZERO*(r0**2.0D0)
      SYNCF = SYNCL/(4.0D0*PI*(DIS**2.0D0))
      NSYNCF = NU*SYNCF
      NSYNCL = NU*SYNCL

      BOT = XMIN
      TOP = XMAX

      ELSE IF ((X1IN.GT.XMID).AND.(X2OUT.LE.XMAX)) THEN
      CALL RES(X1OUT,X2OUT,EPS,INTRES,EPSIL,N2,M2,G2,THETA,GM,ALPHA)
      SYNCL = 4.0D0*(PI**2.0D0)*EMISS(K02,B02,ALPHA,NU,EMASS,CHARGE,C)
& *RZERO*(r0**2.0D0)*INTRES
      SYNCF = SYNCL/(4.0D0*PI*(DIS**2.0D0))
      NSYNCF = NU*SYNCF
      NSYNCL = NU*SYNCL

      BOT = X1OUT
      TOP = X2OUT

      ELSE !IF (X1IN.LT.XMID) THEN
      IF (X1IN.GE.X2IN) THEN
```

```

SYNCL = 0.0D0
SYNCF = 0.0D0
NSYNCF = 0.0D0
NSYNCL = 0.0D0
BOT = 1.0D0
TOP = 1.0D0

ELSE IF (X2IN.LT.XMID) THEN
CALL RES(X1IN,X2IN,EPS,INTRES,EP SIL,N1,M1,G1,THETA,GM,ALPHA)
SYNCL = 4.0D0*(PI**2.0D0)*EMISS(KO1,BO1,ALPHA,NU,EMASS,CHARGE,C)*
& RZERO*(r0**2.0D0)*INTRES
SYNCF = SYNCL/(4.0D0*PI*(DIS**2.0D0))
NSYNCF = NU*SYNCF
NSYNCL = NU*SYNCL

BOT = X1IN
TOP = X2IN

ELSE ! IF (X2IN.GE.XMID.AND.X2OUT.LE.XMAX)
CALL RES(X1IN,XMID,EPS,INTRES,EP SIL,N1,M1,G1,THETA,GM,ALPHA)
INTFOR = INTRES
CALL RES(XMID,X2OUT,EPS,INTRES,EP SIL,N2,M2,G2,THETA,GM,ALPHA)
INTPOS = INTRES
SYNCL = 4.0D0*(PI**2.0D0)*(EMISS(KO1,BO1,ALPHA,NU,EMASS,CHARGE,C)
& *INTFOR+EMISS(KO2,BO2,ALPHA,NU,EMASS,CHARGE,C)*INTPOS)
& *RZERO*(r0**2.0D0)
SYNCF = SYNCL/(4.0D0*PI*(DIS**2.0D0))
NSYNCF = NU*SYNCF
NSYNCL = NU*SYNCL

BOT = X1IN
TOP = X2OUT

END IF
END IF

IF (SYNCL.NE.0.0D0) PRINT *, NU,BOT, TOP
IF (SYNCL.NE.0.0D0)
&WRITE (8,100) NU,SYNCL,SYNCF,NSYNCF,NSYNCL,
&LOG10(NU),LOG10(SYNCL),LOG10(SYNCF),LOG10(NSYNCF),LOG10(NSYNCL)
NU = NU/STEP
END DO

DO WHILE (X1OUT.LT.XMAX.AND.X1OUT.LT.X2OUT.AND.NU.GT.NUAMX2)
X1OUT = LOWLIM(XMIN,XMAX,NU,INUAO2,NUAO2,EP SIL,N2,M2,G2,
& THETA,GM,ALPHA)
X2OUT = UPLIM(XMIN,XMAX,NU,INUMX2,NUMXO2,NUMXX2,EP SIL,E2,M2,G2,
& THETA,GM)
IF (X1OUT.GE.X2OUT) THEN
SYNCL = 0.0D0
SYNCF = 0.0D0
NSYNCF = 0.0D0

```

A.

A.1. Synchrotron Self-Compton Code

```

NSYNCL = 0.0D0
ELSE
CALL RES(X1OUT,X2OUT,EPS,INTRES,EPSIL,N2,M2,G2,THETA,GM,ALPHA)
SYNCL = 4.0D0*(PI**2.0D0)*EMISS(KO2,BO2,ALPHA,NU,EMASS,CHARGE,C)
&      *RZERO*(r0**2.0D0)*INTRES
SYNCF = SYNCL/(4.0D0*PI*(DIS**2.0D0))
NSYNCF = NU*SYNCF
NSYNCL = NU*SYNCL

BOT = X1OUT
TOP = X2OUT

PRINT *, NU,BOT, TOP

WRITE (8,100) NU,SYNCL,SYNCF,NSYNCF,NSYNCL,
&LOG10(NU),LOG10(SYNCL),LOG10(SYNCF),LOG10(NSYNCF),LOG10(NSYNCL)
END IF
NU = NU/STEP
END DO
100 FORMAT (10E16.4)
CLOSE (UNIT=8)
PRINT *, 'SYNCHROTRON CALCULATIONS FINISHED'
PAUSE
c This next part of the main program will calculate the Inverse-Compton
c element using the same distribution of electrons and the relevant
c contribution from the synchrotron emissivity i.e. the synchrotron
c photon field as the incident photons.

NUIC = MIN((NUMX01*(LOLOR1**2.0D0)/1.01),
&          (KN01*(LOLOR1**2.0D0)/1.01))
DO WHILE (NUIC.GT.NUA01)!X1=1
  IF (NUIC/(LOCLOR(XMAX,LOLOR2,EPSIL,E2)**2.0D0).LE.NUMXX2) THEN (1)
c X1=1,X2=xmax
c
c Klein-Nishina bit!
c
  IF (KN01.LT.(NUIC/(LOCLOR(XMAX,LOLOR2,EPSIL,E2)**2.0D0))) THEN !(2)
XKN01 = CUTOFF(KN01,LOLOR1,EPSIL,E1,NUIC)
XKN02 = CUTOFF(KN01,LOLOR2,EPSIL,E2,NUIC)
IF (XKN01.LE.XMID) THEN !(3)
CALL ICRES(XMIN,XKN01,EPS,IICRES,EPSIL,E1,N1,M1,G1,THETA,GM,
&          ALPHA,NUIC,INUA01,INUMX1,LOLOR1,KN01)
ICLUM = 3.0D0/8.0D0*PI*AICA(ALPHA)*C1(ALPHA,EMASS,CHARGE,C)*
&      ETAU1*RZERO*(r0**2.0D0)*
&      (NUIC**(-1.0D0*ALPHA))*IICRES*KO1*(BO1**(1.0D0+ALPHA))
ICFL = ICLUM/(4.0D0*PI*(DIS**2.0D0))
NICFL = NUIC*ICFL

```

A.

A.1. Synchrotron Self-Compton Code

```
NICLUM = NUIC*ICLUM
BOT = XMIN
TOP = XKN01
ELSE !(3)
CALL ICRES(XMIN,XMID,EPS,IICRES,EPSIL,E1,N1,M1,G1,THETA,GM,
& ALPHA,NUIC,INUA01,INUMX1,LOLOR1,KNO1)
IICFOR = ETAU1*KO1*(BO1**(1.ODO+ALPHA))*IICRES
CALL ICRES(XMID,XKN02,EPS,IICRES,EPSIL,E2,N2,M2,G2,THETA,GM,
& ALPHA,NUIC,INUA02,INUMX2,LOLOR2,KNO1)
IICPOS = ETAU2*KO2*(BO2**(1.ODO+ALPHA))*IICRES
IICFUL = IICFOR + IICPOS
ICLUM = 3.ODO/8.ODO*PI*AICA(ALPHA)*C1(ALPHA,EMASS,CHARGE,C)*
& RZERO*(r0**2.ODO)*(NUIC**(-1.ODO*ALPHA))*IICFUL
ICFL = ICLUM/(4.ODO*PI*(DIS**2.ODO))
NICFL = NUIC*ICFL
NICLUM = NUIC*ICLUM
BOT = XMIN
TOP = XKN02
ENDIF !(3)
c
c Back to the original code!
c
ELSE !(2)
CALL ICRES(XMIN,XMID,EPS,IICRES,EPSIL,E1,N1,M1,G1,THETA,GM,
& ALPHA,NUIC,INUA01,INUMX1,LOLOR1,KNO1)
IICFOR = ETAU1*KO1*(BO1**(1.ODO+ALPHA))*IICRES
CALL ICRES(XMID,XMAX,EPS,IICRES,EPSIL,E2,N2,M2,G2,THETA,GM,
& ALPHA,NUIC,INUA02,INUMX2,LOLOR2,KNO1)
IICPOS = ETAU2*KO2*(BO2**(1.ODO+ALPHA))*IICRES
IICFUL = IICFOR + IICPOS
ICLUM = 3.ODO/8.ODO*PI*AICA(ALPHA)*C1(ALPHA,EMASS,CHARGE,C)*
& RZERO*(r0**2.ODO)*(NUIC**(-1.ODO*ALPHA))*IICFUL
ICFL = ICLUM/(4.ODO*PI*(DIS**2.ODO))
NICFL = NUIC*ICFL
NICLUM = NUIC*ICLUM
BOT = XMIN
TOP = XMAX
ENDIF !(2)
ELSE !NUIC/(LOCLOR(XMAX,LOLOR2,EPSIL,E2)**2.ODO).GE.NUMXX2 !(1)
c here x1=XMIN and x2=x where NUIC/lolor(x)**2=NUMXX for NUIC/lolor**2>NUMXX2
c This needs to be calculated for the 1 and 2 jets i.e. for N1,M1..., N2...etc
c NUMXX will depend on NUMX01 and NUMX02 respectively and the solutions will
c match at x=XMID. If NUMX01 solution lies below XMID use that value as x2
c else use the value from the NUMX02 solution (which will be greater than XMID)
c If the latter don't forget two regions to integrate over and then sum
```

A.

A.1. Synchrotron Self-Compton Code

```

      IF (NUIC/(LOCLOR(XMAX,LOLOR1,EP SIL,E1)**2.0D0).LE.NUMXX1) THEN !(4)
      X21 = XMAX
      ELSE !(4)
      X21 = ICUP(XMIN,XMAX,NUIC,LOLOR1,INUMX1,EP SIL,E1,M1,G1,THETA,
&              GM)
      ENDIF !(4)
      X22 = ICUP(XMIN,XMAX,NUIC,LOLOR2,INUMX2,EP SIL,E2,M2,G2,THETA,
&              GM)
      IF (X21.LE.XMID) THEN !(5)
      NMX21 = NUMAXX(X21,INUMX1,EP SIL,E1,M1,G1,THETA,GM)
      C Klein-Nishina bit!!!
      C
      IF (KNO1.LT.NMX21) THEN !(6)
      XKNO1 = CUTOFF(KNO1,LOLOR1,EP SIL,E1,NUIC)
      CALL ICRES(XMIN,XKNO1,EP S,IICRES,EP SIL,E1,N1,M1,G1,THETA,GM,
&              ALPHA,NUIC,INUA01,INUMX1,LOLOR1,KNO1)
      ICLUM = 3.0D0/8.0D0*PI*AICA(ALPHA)*C1(ALPHA,EMASS,CHARGE,C)*
&              ETAU1*RZERO*(r0**2.0D0)*
&              (NUIC**(-1.0D0*ALPHA))*IICRES*KO1*(BO1**(1.0D0+ALPHA))
      ICFL = ICLUM/(4.0D0*PI*(DIS**2.0D0))
      NICFL = NUIC*ICFL
      NICLUM = NUIC*ICLUM
      BOT = XMIN
      TOP = XKNO1

      ELSE !(6)
      C Back to original code
      C
      CALL ICRES(XMIN,X21,EP S,IICRES,EP SIL,E1,N1,M1,G1,THETA,GM,
&              ALPHA,NUIC,INUA01,INUMX1,LOLOR1,KNO1)
      ICLUM = 3.0D0/8.0D0*PI*AICA(ALPHA)*C1(ALPHA,EMASS,CHARGE,C)*
&              ETAU1*RZERO*(r0**2.0D0)*
&              (NUIC**(-1.0D0*ALPHA))*IICRES*KO1*(BO1**(1.0D0+ALPHA))
      ICFL = ICLUM/(4.0D0*PI*(DIS**2.0D0))
      NICFL = NUIC*ICFL
      NICLUM = NUIC*ICLUM
      BOT = XMIN
      TOP = X21
      ENDIF !(6)
      ELSE !(5)
      NMX22 = NUMAXX(X22,INUMX2,EP SIL,E2,M2,G2,THETA,GM)
      C Klein-Nishina bit!
      C
      IF (KNO1.LT.NMX22) THEN !(7)

```

A.

A.1. Synchrotron Self-Compton Code

```
XKNO1 = CUTOFF(KNO1,LOLOR1,EPSIL,E1,NUIC)
XKNO2 = CUTOFF(KNO1,LOLOR2,EPSIL,E2,NUIC)
C
IF (XKNO1.LE.XMID) THEN !(8)
CALL ICRES(XMIN,XKNO1,EPS,IICRES,EPSIL,E1,N1,M1,G1,THETA,GM,
&         ALPHA,NUIC,INUA01,INUMX1,LOLOR1,KNO1)
ICLUM = 3.000/8.000*PI*AICA(ALPHA)*C1(ALPHA,EMASS,CHARGE,C)*
&         ETAU1*RZERO*(r0**2.000)*
&         (NUIC**(-1.000*ALPHA))*IICRES*K01*(B01**(1.000+ALPHA))
ICFL = ICLUM/(4.000*PI*(DIS**2.000))
NICFL = NUIC*ICFL
NICLUM = NUIC*ICLUM
BOT = XMIN
TOP = XKNO1
ELSE !(8)
CALL ICRES(XMIN,XMID,EPS,IICRES,EPSIL,E1,N1,M1,G1,THETA,GM,
&         ALPHA,NUIC,INUA01,INUMX1,LOLOR1,KNO1)
IICFOR = ETAU1*K01*(B01**(1.000+ALPHA))*IICRES
CALL ICRES(XMID,XKNO2,EPS,IICRES,EPSIL,E2,N2,M2,G2,THETA,GM,
&         ALPHA,NUIC,INUA02,INUMX2,LOLOR2,KNO1)
IICPOS = ETAU2*K02*(B02**(1.000+ALPHA))*IICRES
IICFUL = IICFOR + IICPOS
ICLUM = 3.000/8.000*PI*AICA(ALPHA)*C1(ALPHA,EMASS,CHARGE,C)*
&         RZERO*(r0**2.000)*(NUIC**(-1.000*ALPHA))*IICFUL
ICFL = ICLUM/(4.000*PI*(DIS**2.000))
NICFL = NUIC*ICFL
NICLUM = NUIC*ICLUM
BOT = XMIN
TOP = XKNO2
ENDIF !(8)
C
ELSE !(7)
C
C back to original code!
C
&         CALL ICRES(XMIN,XMID,EPS,IICRES,EPSIL,E1,N1,M1,G1,THETA,GM,
&         ALPHA,NUIC,INUA01,INUMX1,LOLOR1,KNO1)
IICFOR = ETAU1*K01*(B01**(1.000+ALPHA))*IICRES
&         CALL ICRES(XMID,X22,EPS,IICRES,EPSIL,E2,N2,M2,G2,THETA,GM,
&         ALPHA,NUIC,INUA02,INUMX2,LOLOR2,KNO1)
IICPOS = ETAU2*K02*(B02**(1.000+ALPHA))*IICRES
IICFUL = IICFOR + IICPOS
&         ICLUM = 3.000/8.000*PI*AICA(ALPHA)*C1(ALPHA,EMASS,CHARGE,C)*
&         RZERO*(r0**2.000)*(NUIC**(-1.000*ALPHA))*IICFUL
ICFL = ICLUM/(4.000*PI*(DIS**2.000))
NICFL = NUIC*ICFL
```

```

      NICLUM = NUIC*ICLUM
      BOT = XMIN
      TOP = X22

      ENDIF !(7)
      END IF !(5)

      ENDIF !(1)

      PRINT *, NUIC,BOT, TOP

      WRITE (9,200) NUIC,ICLUM,ICFL,NICFL,NICLUM,
&LOG10(NUIC),LOG10(ICLUM),LOG10(ICFL),LOG10(NICFL),LOG10(NICLUM)
      NUIC = NUIC/STEP
      END DO

C      ELSE ! while NUAMX2<NUIC<NUA01
c here x2=xmax and x1=x where NUIC=NUAX
c This needs to be calculated for the 1 and 2 jets i.e. for N1,M1..., N2...etc
c NUAX will depend on NUA01 and NUA02 respectively and the solutions will
c match at x=XMID. If NUA01 solution lies below XMID use that value as x1
c else use the value from the NUA02 solution (which will be greater than XMID).
c If the former don't forget two regions to integrate over then sum.

      DO WHILE (NUIC.LE.NUA01.AND.NUIC.GE.NUAMX2)
      IF (NUIC.LT.NUAMX1) THEN
        X11 = XMAX
      ELSE
        X11 = ICLO(XMIN,XMAX,NUIC,INUA01,EPSIL,N1,M1,G1,THETA,GM,ALPHA)
      END IF
      X12 = ICLO(XMIN,XMAX,NUIC,INUA02,EPSIL,N2,M2,G2,THETA,GM,ALPHA)
      IF (X11.LT.XMID) THEN
        CALL ICRES(X11, XMID, EPS, IICRES, EPSIL, E1, N1, M1, G1, THETA, GM,
&                ALPHA, NUIC, INUA01, INUMX1, LOLOR1, KN01)
        IICFOR = ETAU1*K01*(BO1**(1.0DO+ALPHA))*IICRES
        CALL ICRES(XMID, XMAX, EPS, IICRES, EPSIL, E2, N2, M2, G2, THETA, GM,
&                ALPHA, NUIC, INUA02, INUMX2, LOLOR2, KN01)
        IICPOS = ETAU2*K02*(BO2**(1.0DO+ALPHA))*IICRES
        IICFUL = IICFOR + IICPOS
        ICLUM = 3.0DO/8.0DO*PI*AICA(ALPHA)*C1(ALPHA,EMASS,CHARGE,C)*
&            RZERO*(r0**2.0DO)*(NUIC**(-1.0DO*ALPHA))*IICFUL
        ICFL = ICLUM/(4.0DO*PI*(DIS**2.0DO))
        NICFL = NUIC*ICFL
        NICLUM = NUIC*ICLUM
        BOT = X11
        TOP = XMAX
      ELSE

```

A.

A.1. Synchrotron Self-Compton Code

```

CALL ICRES(X12,XMAX,EPS,IICRES,EPSIL,E2,N2,M2,G2,THETA,GM,
&          ALPHA,NUIC,INUAO2,INUMX2,LOLOR2,KN01)
      ICLUM = 3.0D0/8.0D0*PI*AICA(ALPHA)*C1(ALPHA,EMASS,CHARGE,C)*
&          ETAU2*RZERO*(r0**2.0D0)*
&          (NUIC**(-1.0D0*ALPHA))*IICRES*K02*(B02**(1.0D0+ALPHA))
      ICFL = ICLUM/(4.0D0*PI*(DIS**2.0D0))
      NICFL = NUIC*ICFL
      NICLUM = NUIC*ICLUM
      BOT = X12
      TOP = XMAX
END IF
PRINT *, NUIC,BOT, TOP
WRITE (9,200) NUIC,ICLUM,ICFL,NICFL,NICLUM,
&LOG10(NUIC),LOG10(ICLUM),LOG10(ICFL),LOG10(NICFL),LOG10(NICLUM)
      NUIC = NUIC/STEP
END DO
200 FORMAT (10E16.4)
CLOSE (UNIT=9)
STOP
END

```

```

C -----
C -----NEW CODE-----
C -----

```

```

SUBROUTINE LOW3BK(AX,BX,CX,FA,FB,FC,EPSIL,NUAO,N,M,ALPHA,G,
&                THETA,GM)
      IMPLICIT NONE

```

c This program calculates the three abscissa which bracket the minimum
c of a function (EXTERNAL). These are then used in a an external routine
c to calculate the minimum of the function to a given tolerance.
c (Numerical Recipes)

```

      DOUBLE PRECISION AX,BX,CX,FA,FB,FC,DUM,R,Q,U,ULIM,FU,GOLD,GM,
&                GLIMIT,TINY,EPSIL,NUAO,N,M,ALPHA,G,THETA,LOWFN1
      EXTERNAL LOWFN1
      PARAMETER (GOLD=1.618034D0, GLIMIT=100.0D0, TINY=1D-20)
      FA = LOWFN1(AX,EPSIL,NUAO,N,M,ALPHA,G,THETA,GM)
      FB = LOWFN1(BX,EPSIL,NUAO,N,M,ALPHA,G,THETA,GM)
      IF (FB.GT.FA) THEN
        DUM = AX
        AX = BX
        BX = DUM
        DUM = FA
        FA = FB
        FB = DUM
      ENDIF
      CX = BX+GOLD*(BX-AX)
      FC = LOWFN1(CX,EPSIL,NUAO,N,M,ALPHA,G,THETA,GM)

```

```

1  IF (FB.GE.FC) THEN
    R = (BX-AX)*(FB-FC)
    Q = (BX-CX)*(FB-FA)
    U = BX-((BX-CX)*Q-(BX-AX)*R)/
&    (2.ODO*SIGN(MAX(ABS(Q-R),TINY),Q-R))
    ULIM = BX+GLIMIT*(CX-BX)

    IF ((BX-U)*(U-CX).GT.O.ODO) THEN
      FU = LOWFN1(U, EPSIL, NUAO, N, M, ALPHA, G, THETA, GM)

      IF (FU.LT.FC) THEN
        AX = BX
        FA = FB
        BX = U
        FB = FU
        GO TO 1
      ELSE IF (FU.GT.FB) THEN
        CX = U
        FC = FU
        GO TO 1
      END IF
      U = CX+GOLD*(CX-BX)
      FU = LOWFN1(U, EPSIL, NUAO, N, M, ALPHA, G, THETA, GM)
    ELSE IF ((CX-U)*(U-ULIM).GT.O.ODO) THEN
      FU = LOWFN1(U, EPSIL, NUAO, N, M, ALPHA, G, THETA, GM)

      IF (FU.LT.FC) THEN
        BX = CX
        CX = U
        U = CX+GOLD*(CX-BX)
        FB = FC
        FC = FU
        FU = LOWFN1(U, EPSIL, NUAO, N, M, ALPHA, G, THETA, GM)
      END IF

    ELSE IF ((U-ULIM)*(ULIM-CX).GE.O.ODO) THEN
      U = ULIM
      FU = LOWFN1(U, EPSIL, NUAO, N, M, ALPHA, G, THETA, GM)
    ELSE
      U = CX+GOLD*(CX-BX)
      FU = LOWFN1(U, EPSIL, NUAO, N, M, ALPHA, G, THETA, GM)
    END IF

    AX = BX
    BX = CX
    CX = U
    FA = FB
    FB = FC
    FC = FU
    GO TO 1
  END IF

  RETURN

  END

```

```

c -----
c -----END OF NEW CODE-----
c -----

```

```

SUBROUTINE RES(A,B,EPS,ST,EPSIL,N,M,G,THETA,GM,ALPHA)
  IMPLICIT NONE

```

```

c This program is an integration routine to integrate the function
c IGRAND between the limits LOWLIM and UPLIM, PROVIDED that the
c integrand is proper with no nasty singularities either at the upper
c or lower limit, or between the limits i.e. a smooth analytic function.
c The integrand is defined in the external function IGRAND.

```

```

DOUBLE PRECISION IGRAND,A,B,EPS,LIM,X,ST,S,FUNSUM,G,THETA,GM,
&
  ALPHA,EPSIL,N,M,TEST
INTEGER I,IMAX,J
EXTERNAL IGRAND
IMAX = 25
c This calculates the first step i.e. N=1 and initialises S
  S = (B-A)*(IGRAND(A,EPSIL,N,M,G,THETA,GM,ALPHA)/2.0D0+
&IGRAND(B,EPSIL,N,M,G,THETA,GM,ALPHA)/2.0D0)
c This is the main part of the routine. It uses nested DO loop to make
c sequential calls to the extended trapezoidal routine until the
c required accuracy set by EPS is achieved.
  DO I=2,IMAX,1
    LIM = (2.0D0**(I-1.0D0))-1.0D0
    J = 1
    FUNSUM = 0.0D0
      DO WHILE (J.LE.LIM)
        X = A+J*(B-A)/(LIM+1.0D0)
        FUNSUM = FUNSUM + IGRAND(X,EPSIL,N,M,G,THETA,GM,ALPHA)
        J = J+2
      ENDDO
    ST = S/2.0D0+((B-A)/(LIM+1.0D0))*FUNSUM
    TEST = ST-S
    IF(ABS(TEST).GT.EPS) THEN
      IF(I.EQ.IMAX) PRINT*, 'Not enough steps for this accuracy'
      S = ST
    ELSE
c This next step simply removes the leading order error term
c - the surviving error being of the order 1/N**4
      ST = ((4.0D0/3.0D0)*ST)-((1.0D0/3.0D0)*S)
      RETURN
    ENDIF
  ENDDO
END
c -----
SUBROUTINE ICRES(A,B,EPS,ST,EPSIL,E,N,M,G,THETA,GM,ALPHA,NUIC,
&
  INUAO,INUMAX,LOLOR,KNO1)
  IMPLICIT NONE
c This program is an integration routine to integrate the function
c IGRIC between the limits X1 and X2, PROVIDED that the
c integrand is proper with no nasty singularities either at the upper
c or lower limit, or between the limits i.e. a smooth analytic function.
c The integrand is defined in the external function IGRIC.

```

A.

A.1. Synchrotron Self-Compton Code

```
DOUBLE PRECISION IGRIC,A,B,EPS,LIM,X,ST,S,FUNSUM,G,THETA,GM,KNO1,
& ALPHA,EPSIL,N,M,E,NUIC,INUAO,INUMAX,LOLOR,TEST
INTEGER I,IMAX,J
EXTERNAL IGRIC
IMAX = 25
c This calculates the first step i.e. N=1 and initialises S
S = (B-A)*(IGRIC(A,EPSIL,E,N,M,G,THETA,GM,ALPHA,NUIC,INUAO,INUMAX,
& LOLOR,KNO1)/2.0DO+IGRIC(B,EPSIL,E,N,M,G,THETA,GM,ALPHA,NUIC,INUAO
& ,INUMAX,LOLOR,KNO1)/2.0DO)
c This is the main part of the routine. It uses nested DO loop to make
c sequential calls to the extended trapezoidal routine until the
c required accuracy set by EPS is achieved.
DO I=2,IMAX,1
LIM = (2.0DO**(I-1.0DO))-1.0DO
J = 1
FUNSUM = 0.0DO
DO WHILE (J.LE.LIM)
X = A+J*(B-A)/(LIM+1.0DO)
FUNSUM = FUNSUM +
& IGRIC(X,EPSIL,E,N,M,G,THETA,GM,ALPHA,NUIC,INUAO,INUMAX,LOLOR,
& KNO1)
J = J+2
ENDDO
ST = S/2.0DO+((B-A)/(LIM+1.0DO))*FUNSUM
TEST = ST-S
IF(ABS(TEST).GT.EPS) THEN
IF(I.EQ.IMAX) PRINT*, 'Not enough steps for this accuracy'
S = ST
ELSE
c This next step simply removes the leading order error term
c - the surviving error being of the order 1/N**4
ST = ((4.0DO/3.0DO)*ST)-((1.0DO/3.0DO)*S)
RETURN
ENDIF
ENDDO
END
c -----
c -----
DOUBLE PRECISION FUNCTION IGRAND(Y,EPSIL,N,M,G,THETA,GM,ALPHA)
IMPLICIT NONE
c The function to be integrated is entered here (SYNCHROTRON)
DOUBLE PRECISION Y,EPSIL,N,M,G,THETA,GM,ALPHA,XSI,DELTA
```

```

EXTERNAL XSI,DELTA
IGRAND = (Y**(XSI(EPSIL,N,M,ALPHA)-1.0DO))*
&        (DELTA(Y,G,THETA,GM)**(2.0DO+ALPHA))
RETURN
END
c -----
c -----
DOUBLE PRECISION FUNCTION IGRIC(Y, EPSIL, E, N, M, G, THETA, GM, ALPHA,
&                                NUIC, INUAO, INUMAX, LOLOR, KNO1)
IMPLICIT NONE
c The function to be integrated is entered here (INVERSE COMPTON)
DOUBLE PRECISION Y, EPSIL, E, N, M, G, THETA, ALPHA, NUIC, INUAO, INUMAX,
&                                LOLOR, ELL, DELTA, NUABS, NUMAXX, NUABSY, NUMAXY,
&                                NU1, NU2, LOCLOR, GM, KNO1
EXTERNAL ELL, DELTA, NUABS, NUMAXX, LOCLOR
NUABSY = NUABS(INUAO, Y, EPSIL, N, M, G, ALPHA, THETA, GM)
NUMAXY = NUMAXX(Y, INUMAX, EPSIL, E, M, G, THETA, GM)
NU1 = MAX(NUABSY, (NUIC/(LOCLOR(Y, LOLOR, EPSIL, E)**2.0DO)))
NU2 = MIN(NUMAXY, NUIC, KNO1)
IGRIC = (Y**(ELL(EPSIL, N, M, ALPHA)-1.0DO))*
&        (DELTA(Y, G, THETA, GM)**(2.0DO+ALPHA))*LOG(NU2/NU1)
RETURN
END
c -----
c -----
DOUBLE PRECISION FUNCTION
&NUAO(ALPHA, EMASS, CHARGE, C, KO, BO, r0, THETA)
IMPLICIT NONE
c This function calculates the self-absorption frequency at the base of
c the jet using the relevant values for K0 and B0, ensuring continuous
c solutions at XMID in a two stage jet.
DOUBLE PRECISION ALPHA, EMASS, CHARGE, C, KO, BO, r0, THETA, D1, TAU
EXTERNAL D1, TAU
NUAO = ((2.0DO*D1(ALPHA, EMASS, CHARGE, C)*KO*(BO**(1.5DO+ALPHA))*
&        r0)/(DSIN(THETA)*TAU(1.0D-3, 2.0DO, ALPHA)))*
&        (2.0DO/(5.0DO+2.0DO*ALPHA))
RETURN
END
c -----
c -----

```

A.

A.1. Synchrotron Self-Compton Code

```
DOUBLE PRECISION FUNCTION  
&NUABS(NUAO,X,EPSIL,N,M,G,ALPHA,THETA,GM)
```

```
IMPLICIT NONE
```

c This function calculates the synchrotron self-absorbtion frequency at XMAX.

```
DOUBLE PRECISION NUAO,X,EPSIL,N,M,G,ALPHA,THETA,GM,KSUBM,DELTA  
EXTERNAL KSUBM,DELTA
```

```
NUABS = NUAO*(X**(-1.0DO*KSUBM(EPSIL,N,M,ALPHA)))  
& *DELTA(X,G,THETA,GM)
```

```
RETURN
```

```
END
```

```
c -----  
c -----
```

```
DOUBLE PRECISION FUNCTION NUMAXO(C,CHARGE,EMASS,LOLOR,BO)
```

```
IMPLICIT NONE
```

c This function calculates the maximum synchrotron frequency at the base of the
c jet. Again this is needed for continuous solutions at XMID.

```
DOUBLE PRECISION C,CHARGE,EMASS,LOLOR,BO,PI
```

```
PI = 4.0DO*DATAN(1.0DO)
```

```
NUMAXO = (CHARGE/(PI*EMASS*2.0DO*C))*(LOLOR**2.0DO)*BO
```

```
RETURN
```

```
END
```

```
c -----  
c -----
```

```
DOUBLE PRECISION FUNCTION NUMAXX(X,NUMXO,EPSIL,E,M,G,THETA,GM)
```

```
IMPLICIT NONE
```

c This function calculates the maximum synchrotron frequency at XMAX. Again this
c is needed for continuous solutions at XMID.

```
DOUBLE PRECISION X,NUMXO,EPSIL,E,M,G,THETA,GM,ETA,DELTA
```

```
EXTERNAL ETA,DELTA
```

```
NUMAXX = NUMXO*(X**(-1.0DO*ETA(EPSIL,E,M)))*DELTA(X,G,THETA,GM)
```

```
RETURN
```

```
END
```

```
c -----  
c -----
```

```
DOUBLE PRECISION FUNCTION LOCLOR(X,LOLOR,EPSIL,E)
```

```
IMPLICIT NONE
```

c This calculates the maximum local lorentz factor of the electron
c distribution at any point in the jet, x

```
DOUBLE PRECISION X,LOLOR,EPSIL,E
```

```
LOCLOR = LOLOR*(X**(-1.0DO*EPSIL*E))
```

A.

A.1. Synchrotron Self-Compton Code

```
      RETURN
      END
c -----
c -----
      DOUBLE PRECISION FUNCTION ETA(EPSIL,E,M)
      IMPLICIT NONE
c This is calculated externally since E and M can have different values
c along the jet: either E1,E2,M1,M2. This is the power law for the variation
c of the maximum synchrotron frequency along the jet.
      DOUBLE PRECISION EPSIL,E,M
      ETA = EPSIL*(2.000*E+M)
      RETURN
      END
c -----
c -----
      DOUBLE PRECISION FUNCTION XSI(EPSIL,N,M,ALPHA)
      IMPLICIT NONE
c This is calculated externally since E and M can have different values
c along the jet: either N1,N2,M1,M2. This is a combination of various power laws
c used in the luminosity integration.
      DOUBLE PRECISION EPSIL,N,M,ALPHA
      XSI = (EPSIL*(2.000-N-M*(1.000+ALPHA)))+1.000
      RETURN
      END
c -----
c -----
      DOUBLE PRECISION FUNCTION ELL(EPSIL,N,M,ALPHA)
      IMPLICIT NONE
c This is calculated externally since E and M can have different values
c along the jet: either N1,N2,M1,M2. This is a combination of various power laws
c used in the Inverse-Compton luminosity integration.
      DOUBLE PRECISION EPSIL,N,M,ALPHA
      ELL = (EPSIL*(3.000-2.000*N-M*(1.000+ALPHA)))+1.000
      RETURN
      END
c -----
c -----
      DOUBLE PRECISION FUNCTION EMISS(KO,BO,ALPHA,NU,EMASS,CHARGE,C)
      IMPLICIT NONE
c Calculates the value of emissivity for given values of ALPHA,
c electron density parameter (KO), magnetic field (BO) and
```

A.

A.1. Synchrotron Self-Compton Code

c the frequency NU. Note this calculates emiss(nu,1). The X dependance
c is included in the Luminosity integration in the main program.

```
DOUBLE PRECISION PI,C1,KO,BO,ALPHA,NU,EMASS,CHARGE,C
EXTERNAL C1
```

```
PI = 4.0DO*DATAN(1.0DO)
```

```
EMISS = C1(ALPHA,EMASS,CHARGE,C)*KO*(BO**(1.0DO+ALPHA))*
&(NU**(-1.0DO*ALPHA))/(4.0DO*PI)
```

```
RETURN
```

```
END
```

c -----
c -----

```
DOUBLE PRECISION FUNCTION C1(Z,EMASS,CHARGE,C)
```

```
IMPLICIT NONE
```

c Calculates the value of the constant C1 in the equation for the
c emissivity. the dummy variable for alpha is Z. EMASS, CHARGE
c and C are constants passed from the main program.

```
DOUBLE PRECISION AAFP,PI,P,Z,EMASS,CHARGE,C
EXTERNAL AAFP
```

c Define some initial constants - PI and P(the exponent in the power law
c distribution of electrons where alpha=(p-1)/2).

```
PI = 4.0DO*DATAN(1.0DO)
P = 2.0DO*Z+1.0DO
```

```
C1 = ((4.0DO*PI)**(1.0DO-Z))*(3.0DO**Z)*(CHARGE**(3.0DO+Z))*
& AAFP(P)/((EMASS**(1.0DO+Z))*(C**(2.0DO+Z)))
```

```
RETURN
```

```
END
```

c -----
c -----

```
DOUBLE PRECISION FUNCTION AAFP(P)
```

```
IMPLICIT NONE
```

c calculates the value of a(p) needed to calculate c1 (required for the
c value of emissivity. The function GAMMALN is used to calculate the
c various gamma functions.

```
DOUBLE PRECISION GAMMALN,X,PI,P
EXTERNAL GAMMALN
```

```
PI = 4.0DO*DATAN(1.0DO)
```

```
X = ((P-1.0DO)/2.0DO)*DLOG(2.0DO)+DLOG(DSQRT(3.0DO))+
&GAMMALN((3.0DO*P-1.0DO)/12.0DO)+GAMMALN((3.0DO*P+19.0DO)/12.0DO)+
&GAMMALN((P+5.0DO)/4.0DO)-DLOG(8.0DO)-DLOG(PI)/2.0DO-DLOG(P+1.0DO)-
&GAMMALN((P+7.0DO)/4.0DO)
```

```
AAFP = DEXP(X)
```

```
RETURN
```

```
END
```

A.

A.1. Synchrotron Self-Compton Code

```

c -----
c -----
      DOUBLE PRECISION FUNCTION D1(ALPHA,EMASS,CHARGE,C)
      IMPLICIT NONE
c Calculates the value of the constant D1 in the equation for the
c absorption. EMASS, CHARGE and C are constants passed from the main
c program.
      DOUBLE PRECISION GOFP,PI,P,ALPHA,EMASS,CHARGE,C
      EXTERNAL GOFP
c Define some initial constants - PI and P(the exponent in the power law
c distribution of electrons where alpha=(p-1)/2).
      PI = 4.000*DATAN(1.000)
      P = 2.000*ALPHA+1.000
      D1 = GOFP(P)*(((CHARGE**3.000)/(2.000*PI*(EMASS**2.000)*
&(C**2.000)))*(((3.000*CHARGE)/(2.000*PI*EMASS*C))**(P/2.000))
      RETURN
      END
c -----
c -----
      DOUBLE PRECISION FUNCTION GOFP(P)
      IMPLICIT NONE
c calculates the value of g(p) needed to calculate d1 (required for the
c value of absorption. The function GAMMALN is used to calculate the
c various gamma functions.
      DOUBLE PRECISION GAMMALN,X,PI,P
      EXTERNAL GAMMALN
      PI = 4.000*DATAN(1.000)
      X = DLOG(DSQRT(3.000)/4.000)+GAMMALN((3.000*P+2.000)/12.000)+
&GAMMALN((3.000*P+22.000)/12.000)
      GOFP = DEXP(X)
      RETURN
      END
c -----
c -----
      DOUBLE PRECISION FUNCTION GAMMALN(XX)
      IMPLICIT NONE
c returns the value ln[gamma(XX) fo XX>0. Full accuracy is obtained for
c XX>1. For 0< XX<1, the reflection formula is used. Taken from 'Numerical
c Recipes. The Art of Scientific Computing' Cambridge University Press.
      DOUBLE PRECISION COF(6),STP,HALF,ONE,FPF,X,TMP,SER,Y,PI,XX
      INTEGER J
c Internal arithmetic is done in double precision, which can be omitted
c if five-figure accuracy is sufficient

```

A.

A.1. Synchrotron Self-Compton Code

```
DATA COF,STP/76.18009173D0,-86.50532033D0,24.01409822D0,  
&-1.231739516D0,0.120858003D-2,-0.536382D-5,2.50662827465D0/  
DATA HALF,ONE,FPF/0.5D0,1.0D0,5.5D0/
```

c Define pi

```
PI = 4.0D0*DATAN(1.0D0)  
IF (XX.LT.1.0D0) THEN  
  Y = 2.0D0-XX  
ELSE  
  Y = XX  
ENDIF  
  
X = Y-ONE  
TMP = X+FPF  
TMP = (X+HALF)*DLOG(TMP)-TMP  
SER = ONE  
  
DO 11 J = 1,6  
  X = X+ONE  
  SER = SER+COF(J)/X  
11 CONTINUE  
  
GAMMALN = TMP+DLOG(STP*SER)  
IF (XX.LT.1.0D0) THEN  
  GAMMALN = DLOG(PI*(1.0D0-XX))-GAMMALN-  
& DLOG(DSIN(PI*(1.0D0-XX)))  
ENDIF  
RETURN  
END
```

c -----
c -----

```
DOUBLE PRECISION FUNCTION TAU(X1,X2,ALPHA)  
IMPLICIT NONE  
DOUBLE PRECISION X1,X2,XACC,F,FL,FH,DF,DX,XL,XH,SWAP,DXOLD,TEMP,  
& ALPHA  
INTEGER J,MAXIT  
PARAMETER (MAXIT=100)  
XACC = 1.0D-3  
CALL TAUFD(X1,FL,DF,ALPHA)  
CALL TAUFD(X2,FH,DF,ALPHA)  
IF(FL.LT.0.0D0) THEN  
  XL = X1  
  XH = X2  
ELSE  
  XH = X1  
  XL = X2  
  SWAP = FL  
  FL = FH  
  FH = SWAP  
ENDIF  
TAU = 0.5D0*(X1+X2)
```

```

DXOLD = ABS(X2-X1)
DX = DXOLD
CALL TAUFDF(TAU,F,DF,ALPHA)
DO 11 J=1,MAXIT
&   IF(((TAU-XH)*DF-F)*((TAU-XL)*DF-F).GE.O.ODO.OR.
      ABS(2.ODO*F).GT.ABS(DXOLD*DF)) THEN
      DXOLD = DX
      DX = 0.5DO*(XH-XL)
      TAU = XL+DX
      IF (XL.EQ.TAU) RETURN
    ELSE
      DXOLD = DX
      DX = F/DF
      TEMP = TAU
      TAU = TAU-DX
      IF (TEMP.EQ.TAU) RETURN
    END IF
    IF(ABS(DX).LT.XACC) RETURN
    CALL TAUFDF(TAU,F,DF,ALPHA)
    IF (F.LT.O.ODO) THEN
      XL = TAU
      FL = F
    ELSE
      XH = TAU
      FH = F
    ENDIF
11  CONTINUE
    PAUSE 'TAU exceeding maximum iterations'
    RETURN
    END
c -----
SUBROUTINE TAUFDF(X,F,DF,ALPHA)
IMPLICIT NONE
DOUBLE PRECISION X,F,DF,ALPHA
F = EXP(X)-(((2.ODO*ALPHA)+5.ODO)/5.ODO)*X-1.ODO
DF = EXP(X)-((2.ODO*ALPHA)+5.ODO)/5.ODO
RETURN
END
c -----
c -----
DOUBLE PRECISION FUNCTION AICA(Z)
IMPLICIT NONE
c Calculates the value of the coefficient A(alpha) in the equation for the

```

A.

A.1. Synchrotron Self-Compton Code

c inverse compton luminosity. The dummy variable for alpha is Z.

```
DOUBLE PRECISION P,Z
```

c Define some initial constants - P(the exponent in the power law
c distribution of electrons where alpha=(p-1)/2).

```
P = 2.0D0*Z+1.0D0
```

```
AICA = (2.0D0**(P+3.0D0))*((P**2.0D0)+4.0D0*P+11.0D0)/  
&      ((P+1.0D0)*((P+3.0D0)**2.0D0)*(P+5.0D0))
```

```
RETURN
```

```
END
```

c -----
c -----

```
DOUBLE PRECISION FUNCTION DELTA(X,G,THETA,GM)
```

```
IMPLICIT NONE
```

```
DOUBLE PRECISION X,G,THETA,GM
```

```
DELTA = 1.0D0/(GM*(X**G)-DSQRT((GM**2.0D0)*(X**(2.0D0*G))-1.0D0)  
&      *DCOS(THETA))
```

```
RETURN
```

```
END
```

c -----
c -----

```
DOUBLE PRECISION FUNCTION DFDELT(X,G,THETA,GM)
```

```
IMPLICIT NONE
```

```
DOUBLE PRECISION X,G,THETA,NUM,NUM1,NUM2,NUM3,DEN,GM
```

```
NUM1 = GM*G*(X**(G-1.0D0))
```

```
NUM2 = (GM**2.0D0)*G*(X**(2.0D0*G-1.0D0))
```

```
NUM3 = (((GM**2.0D0)*X**(2.0D0*G))-1.0D0)**(-0.5D0)*DCOS(THETA)
```

```
NUM = -1.0D0*(NUM1-NUM2*NUM3)
```

```
DEN = (((GM *X**G)-DSQRT((GM**2.0D0)*X**(2.0D0*G))-1.0D0)  
&      *DCOS(THETA))**2.0D0
```

```
DFDELT = NUM/DEN
```

```
RETURN
```

```
END
```

c -----
c -----

```
DOUBLE PRECISION FUNCTION LOWLIM(X1,X2,NU,INUAO,NUABO,EPSIL,  
&      N,M,G,THETA,GM,ALPHA)
```

```
IMPLICIT NONE
```

```
DOUBLE PRECISION X1,X2,XACC,F,FL,FH,DF,DX,NU,INUAO,NUABO,ALPHA,  
&      EPSIL,N,M,G,THETA,GM,XL,XH,SWAP,DXOLD,TEMP
```

```
INTEGER J,MAXIT
```

```
PARAMETER (MAXIT=100)
```

```

IF (NU.GE.NUABO) THEN
  LOWLIM = X1
  RETURN
ELSE
  XACC = 1.0D-3
  CALL SYNLO(X1,FL,DF,NU,INUAO,EPSIL,N,M,G,THETA,GM,ALPHA)
  CALL SYNLO(X2,FH,DF,NU,INUAO,EPSIL,N,M,G,THETA,GM,ALPHA)
  IF(FL.LT.O.ODO) THEN
    XL = X1
    XH = X2
  ELSE
    XH = X1
    XL = X2
    SWAP = FL
    FL = FH
    FH = SWAP
  ENDIF
  LOWLIM = 0.5D0*(X1+X2)
  DXOLD = ABS(X2-X1)
  DX = DXOLD
  CALL SYNLO(LOWLIM,F,DF,NU,INUAO,EPSIL,N,M,G,THETA,GM,ALPHA)
  DO 11 J=1,MAXIT
    IF(((LOWLIM-XH)*DF-F)*((LOWLIM-XL)*DF-F).GE.O.ODO.OR.
& ABS(2.ODO*F).GT.ABS(DXOLD*DF)) THEN
      DXOLD = DX
      DX = 0.5D0*(XH-XL)
      LOWLIM = XL+DX
      IF (XL.EQ.LOWLIM) RETURN
    ELSE
      DXOLD = DX
      DX = F/DF
      TEMP = LOWLIM
      LOWLIM = LOWLIM-DX
      IF (TEMP.EQ.LOWLIM) RETURN
    END IF
    IF(ABS(DX).LT.XACC) RETURN
  CALL SYNLO(LOWLIM,F,DF,NU,INUAO,EPSIL,N,M,G,THETA,GM,ALPHA)
  IF (F.LT.O.ODO) THEN
    XL = LOWLIM
    FL = F
  ELSE
    XH = LOWLIM
    FH = F
  ENDIF
11 CONTINUE

```

A.

A.1. Synchrotron Self-Compton Code

```
    PAUSE 'LOWLIM exceeding maximum iterations'
    ENDIF
    RETURN
    END
C -----
    SUBROUTINE SYNLO(X,F,DF,NU,NUABO, EPSIL,N,M,G,THETA,GM,ALPHA)
    IMPLICIT NONE
    DOUBLE PRECISION X,F,DF,NU,A,B,DELTA,DFDELTA,KSUBM,NUABO,
    & EPSIL,N,M,ALPHA,G,THETA,GM
    EXTERNAL DELTA,DFDELTA,KSUBM
    A = NU/NUABO
    B = KSUBM(EPSIL,N,M,ALPHA)
    F = A*(X**B)-DELTA(X,G,THETA,GM)
    DF = A*B*(X**(B-1.0D0))+ DFDELTA(X,G,THETA,GM)
    RETURN
    END
C -----
C -----
    DOUBLE PRECISION FUNCTION KSUBM(EPSIL,N,M,ALPHA)
    IMPLICIT NONE
c Calculates the value of KSUBM which defines the frequency cutoff due
c to synchrotron self absorption. Used in the calculation of LOWLIM
    DOUBLE PRECISION EPSIL,N,M,ALPHA
    KSUBM = 2.0D0*EPSIL*(N+M*(1.5D0+ALPHA)-1.0D0)/(5.0D0+2.0D0*ALPHA)
    RETURN
    END
C -----
C -----
    DOUBLE PRECISION FUNCTION UPLIM(X1,X2,NU,INUMXO,NUMXO,NUMXX,
    & EPSIL,E,M,G,THETA,GM)
    IMPLICIT NONE
    DOUBLE PRECISION X1,X2,XACC,F,FL,FH,DF,DX,NU,NUMXO,NUMXX,INUMXO,
    & EPSIL,E,M,G,THETA,GM,XL,XH,SWAP,DXOLD,TEMP
    INTEGER J,MAXIT
    PARAMETER (MAXIT=100)
    IF (NU.GT.NUMXO) THEN
        UPLIM = X1
        RETURN
    ELSE IF (NU.LT.NUMXX) THEN
        UPLIM = X2
```

```

      RETURN
    ELSE
      XACC = 1.0D-3
      CALL SYNHI(X1,FL,DF,NU,INUMXO,EPSIL,E,M,G,THETA,GM)
      CALL SYNHI(X2,FH,DF,NU,INUMXO,EPSIL,E,M,G,THETA,GM)
      IF(FL.LT.0.0D0) THEN
        XL = X1
        XH = X2
      ELSE
        XH = X1
        XL = X2
        SWAP = FL
        FL = FH
        FH = SWAP
      ENDIF
      UPLIM = 0.5D0*(X1+X2)
      DXOLD = ABS(X2-X1)
      DX = DXOLD
      CALL SYNHI(UPLIM,F,DF,NU,INUMXO,EPSIL,E,M,G,THETA,GM)
      DO 11 J=1,MAXIT
        & IF(((UPLIM-XH)*DF-F)*((UPLIM-XL)*DF-F).GE.0.0D0.OR.
          ABS(2.0D0*F).GT.ABS(DXOLD*DF)) THEN
          DXOLD = DX
          DX = 0.5D0*(XH-XL)
          UPLIM = XL+DX
          IF (XL.EQ.UPLIM) RETURN
        ELSE
          DXOLD = DX
          DX = F/DF
          TEMP = UPLIM
          UPLIM = UPLIM-DX
          IF (TEMP.EQ.UPLIM) RETURN
        END IF
        IF(ABS(DX).LT.XACC) RETURN
        CALL SYNHI(UPLIM,F,DF,NU,INUMXO,EPSIL,E,M,G,THETA,GM)
        IF (F.LT.0.0D0) THEN
          XL = UPLIM
          FL = F
        ELSE
          XH = UPLIM
          FH = F
        ENDIF
      11 CONTINUE
      PAUSE 'UPLIM exceeding maximum iterations'
    END IF

```

A.

A.1. Synchrotron Self-Compton Code

```
RETURN
END
C -----
SUBROUTINE SYNHI(X,F,DF,NU,NUMXO, EPSIL,E,M,G,THETA,GM)
  IMPLICIT NONE
  DOUBLE PRECISION X,F,DF,NU,A,B,DELTA,DFDELTA,
& NUMXO, EPSIL,E,M,G,THETA,GM
  EXTERNAL DELTA,DFDELTA
  A = NU/NUMXO
  B = EPSIL*(2.0D0*E+M)
  F = A*(X**B)-DELTA(X,G,THETA,GM)
  DF = A*B*(X**(B-1.0D0))+ DFDELTA(X,G,THETA,GM)
  RETURN
  END
C -----
C -----
DOUBLE PRECISION FUNCTION ICUP(X1,X2,NUIC,LOLOR,NUMXO,
& EPSIL,E,M,G,THETA,GM)
  IMPLICIT NONE
  DOUBLE PRECISION X1,X2,XACC,F,FL,FH,DF,DX,NUIC,LOLOR,NUMXO,
& EPSIL,E,M,G,THETA,GM,XL,XH,SWAP,DXOLD,TEMP
  INTEGER J,MAXIT
  PARAMETER (MAXIT=100)
  XACC = 1.0D-3
  CALL ICUPFD(X1,FL,DF,NUIC,LOLOR,NUMXO, EPSIL,E,M,G,THETA,GM)
  CALL ICUPFD(X2,FH,DF,NUIC,LOLOR,NUMXO, EPSIL,E,M,G,THETA,GM)
  IF(FL.LT.0.0D0) THEN
    XL = X1
    XH = X2
  ELSE
    XH = X1
    XL = X2
    SWAP = FL
    FL = FH
    FH = SWAP
  ENDIF
  ICUP = 0.5D0*(X1+X2)
  DXOLD = ABS(X2-X1)
  DX = DXOLD
  CALL ICUPFD(ICUP,F,DF,NUIC,LOLOR,NUMXO, EPSIL,E,M,G,THETA,GM)
  DO 11 J=1,MAXIT
    IF(((ICUP-XH)*DF-F)*((ICUP-XL)*DF-F).GE.0.0D0.OR.
& ABS(2.0D0*F).GT.ABS(DXOLD*DF)) THEN
```

```

        DXOLD = DX
        DX = 0.5D0*(XH-XL)
        ICUP = XL+DX
        IF (XL.EQ.ICUP) RETURN

    ELSE

        DXOLD = DX
        DX = F/DF
        TEMP = ICUP
        ICUP = ICUP-DX
        IF (TEMP.EQ.ICUP) RETURN

    END IF

    IF (ABS(DX).LT.XACC) RETURN

    CALL ICUPFD(ICUP,F,DF,NUIC,LOLOR,NUMXO,EPSIL,E,M,G,THETA,GM)

    IF (F.LT.O.ODO) THEN

        XL = ICUP
        FL = F

    ELSE

        XH = ICUP
        FH = F

    ENDIF

11  CONTINUE
    PAUSE 'ICUP exceeding maximum iterations'
    RETURN
    END

```

```

c -----
SUBROUTINE ICUPFD(X,F,DF,NUIC,LOLOR,NUMXO,EPSIL,E,M,G,THETA,GM)
    IMPLICIT NONE
    DOUBLE PRECISION X,F,DF,NUIC,A,B,DELTA,DFDELT,LOLOR,
&                    NUMXO,EPSIL,E,M,G,THETA,GM
    EXTERNAL DELTA,DFDELT
    A = NUIC/((LOLOR**2)*NUMXO)
    B = EPSIL*(4.0D0*E+M)
    F = A*(X**B)-DELTA(X,G,THETA,GM)
    DF = A*B*(X**(B-1.0D0))+ DFDELT(X,G,THETA,GM)
    RETURN
    END

```

```

c -----
c -----
DOUBLE PRECISION FUNCTION ICLO(X1,X2,NUIC,NUABO,EPSIL,
&                               N,M,G,THETA,GM,ALPHA)
    IMPLICIT NONE
    DOUBLE PRECISION X1,X2,XACC,F,FL,FH,DF,DX,NUIC,NUABO,ALPHA,
&                    EPSIL,N,M,G,THETA,GM,XL,XH,SWAP,DXOLD,TEMP
    INTEGER J,MAXIT

```

```

PARAMETER (MAXIT=100)
XACC = 1.0D-3
CALL ICLOFD(X1,FL,DF,NUIC,NUABO,EPSIL,N,M,G,THETA,GM,ALPHA)
CALL ICLOFD(X2,FH,DF,NUIC,NUABO,EPSIL,N,M,G,THETA,GM,ALPHA)
IF(FL.LT.0.0D0) THEN
    XL = X1
    XH = X2
ELSE
    XH = X1
    XL = X2
    SWAP = FL
    FL = FH
    FH = SWAP
ENDIF
ICLO = 0.5D0*(X1+X2)
DXOLD = ABS(X2-X1)
DX = DXOLD
CALL ICLOFD(ICLO,F,DF,NUIC,NUABO,EPSIL,N,M,G,THETA,GM,ALPHA)
DO 11 J=1,MAXIT
    IF(((ICLO-XH)*DF-F)*((ICLO-XL)*DF-F).GE.0.0D0.OR.
&    ABS(2.0D0*F).GT.ABS(DXOLD*DF)) THEN
        DXOLD = DX
        DX = 0.5D0*(XH-XL)
        ICLO = XL+DX
        IF (XL.EQ.ICLO) RETURN
    ELSE
        DXOLD = DX
        DX = F/DF
        TEMP = ICLO
        ICLO = ICLO-DX
        IF (TEMP.EQ.ICLO) RETURN
    END IF
    IF(ABS(DX).LT.XACC) RETURN
    CALL ICLOFD(ICLO,F,DF,NUIC,NUABO,EPSIL,N,M,G,THETA,GM,ALPHA)
    IF (F.LT.0.0D0) THEN
        XL = ICLO
        FL = F
    ELSE
        XH = ICLO
        FH = F
    ENDIF
11 CONTINUE
PAUSE 'ICLO exceeding maximum iterations'
RETURN

```

A.

A.1. Synchrotron Self-Compton Code

END

c

SUBROUTINE ICLOFD(X,F,DF,NUIC,NUABO,EPSIL,N,M,G,THETA,GM,ALPHA)

IMPLICIT NONE

DOUBLE PRECISION X,F,DF,NUIC,A,B,DELTA,DFDELTA,KSUBM,NUABO,
& EPSIL,N,M,ALPHA,G,THETA,GM

EXTERNAL DELTA,DFDELTA,KSUBM

A = NUIC/NUABO

B = KSUBM(EPSIL,N,M,ALPHA)

F = A*(X**B)-DELTA(X,G,THETA,GM)

DF = A*B*(X**(B-1.0D0))+ DFDELTA(X,G,THETA,GM)

RETURN

END

c

c

DOUBLE PRECISION FUNCTION LOWDX(X,EPSIL,N,M,ALPHA,G,THETA,GM)

c This function calculates the value of $d/dx(x^{km}\delta(x,\theta))$
c for some value x. This is used in the code to calculate the lower
c limits of the integration contained in the Synchrotron Luminosity
c calculation. Note $x=1$ is NEVER used as this is a point of discontinuity.

IMPLICIT NONE

DOUBLE PRECISION X,EPSIL,N,M,ALPHA,G,THETA,GM,KSUBM,DELTA,
& DFDELTA,KM

EXTERNAL KSUBM,DELTA,DFDELTA

KM = KSUBM(EPSIL,N,M,ALPHA)

LOWDX = -1.0D0*KM*(X**(-1.0D0*(KM+1.0D0)))*DELTA(X,G,THETA,GM)+
& (X**(-1.0D0*KM))*DFDELTA(X,G,THETA,GM)

RETURN

END

c

c

DOUBLE PRECISION FUNCTION GOLDEN(AX,BX,CX,TOL,LOWMAX,EPSIL,NUAO,
& N,M,ALPHA,G,THETA,GM)

c This function takes a function, F, and a bracketing triplet of abscissas
c (such that BX is between AX and CX and F(BX) is less than both F(AX) and
c F(CX), and searches for the minimum, isolating it to a fractional precision
c of about TOL. The abscissa of the minimum is returned as XMIN and the minimum
c function value is returned as GOLDEN.

IMPLICIT NONE

DOUBLE PRECISION AX,BX,CX,TOL,LOWMAX,R,C,X0,X1,X2,X3,F0,F1,F2,F3,
& LOWFN1,EPSIL,NUAO,N,M,ALPHA,G,THETA,GM

EXTERNAL LOWFN1

PARAMETER (R=0.61803399D0,C=1.0D0-R)

X0 = AX

```

X3 =CX
IF (ABS(CX-BX).GT.ABS(BX-AX)) THEN
  X1 = BX
  X2 = BX+C*(CX-BX)
ELSE
  X2 = BX
  X1 = BX-C*(BX-AX)
END IF
F1 = LOWFN1(X1, EPSIL, NUAO, N, M, ALPHA, G, THETA, GM)
F2 = LOWFN1(X2, EPSIL, NUAO, N, M, ALPHA, G, THETA, GM)
1  IF (ABS(X3-X0).GT.TOL*(ABS(X1)+ABS(X2))) THEN
  IF (F2.LT.F1) THEN
    X0 = X1
    X1 = X2
    X2 = R*X1+C*X3
    F0 = F1
    F1 = F2
    F2 = LOWFN1(X2, EPSIL, NUAO, N, M, ALPHA, G, THETA, GM)
  ELSE
    X3 = X2
    X2 = X1
    X1 = R*X2+C*X0
    F3 = F2
    F2 = F1
    F1 = LOWFN1(X1, EPSIL, NUAO, N, M, ALPHA, G, THETA, GM)
  END IF
GO TO 1
END IF
IF (F1.LT.F2) THEN
  GOLDEN = F1
  LOWMAX = X1
ELSE
  GOLDEN = F2
  LOWMAX = X2
END IF
RETURN
END

```

```

C -----
C -----
DOUBLE PRECISION FUNCTION LOWFN1(X, EPSIL, NUAO, N, M, ALPHA, G,
&                                THETA, GM)
  IMPLICIT NONE
  DOUBLE PRECISION X, EPSIL, NUAO, N, M, ALPHA, G, THETA, GM, KSUBM, DELTA
  EXTERNAL KSUBM, DELTA
  LOWFN1 = -1.0DO*NUAO*(X**(-1.0DO*KSUBM(EPSIL, N, M, ALPHA)))
&          *DELTA(X, G, THETA, GM)
  RETURN
END

```

```

C -----
C -----
DOUBLE PRECISION FUNCTION CUTOFF(KN, LOLOR, EPSIL, E, NUIC)
  IMPLICIT NONE
  DOUBLE PRECISION KN, LOLOR, EPSIL, E, NUIC

```

A.

A.1. Synchrotron Self-Compton Code

```
CUTOFF = (KN*(LOLOR**2.0D0)/NUIC)**(1.0D0/(2.0D0*EPSIL*E))
```

```
RETURN
```

```
END
```

```
c -----THE END-----
```

Appendix B

Definition of Hillas Parameters

B.1 Definition of Hillas Parameters

The photo-multiplier tube positions are given coordinates x and y (in degrees). The number of digital counts after calibration for tube i is given by n_i . The summations run over all the tubes in an image. The origin of the coordinate system is the centre of the FoV. An ellipse is fitted to the image and the first and second order Hillas parameters [56][29] are calculated relative to the centre. The various moments are then defined as:

$$\begin{aligned}\langle x \rangle &= \frac{\sum n_i x_i}{\sum n_i} & \langle y \rangle &= \frac{\sum n_i y_i}{\sum n_i} \\ \langle x^2 \rangle &= \frac{\sum n_i x_i^2}{\sum n_i} & \langle y^2 \rangle &= \frac{\sum n_i y_i^2}{\sum n_i} \\ \langle xy \rangle &= \frac{\sum n_i x_i y_i}{\sum n_i}\end{aligned}$$

The spread of the image in different directions are then defined by the following moments:

$$\begin{aligned}\sigma_{x^2} &= \langle x^2 \rangle - \langle x \rangle^2 \\ \sigma_{y^2} &= \langle y^2 \rangle - \langle y \rangle^2 \\ \sigma_{xy} &= \langle xy \rangle - \langle x \rangle \langle y \rangle\end{aligned}$$

Given the following definitions:

$$\begin{aligned}d &= \sigma_{y^2} - \sigma_{x^2} \\ s &= \sqrt{d^2 + 4(\sigma_{xy})^2} \\ w &= \sqrt{((\langle y^2 \rangle - \langle x^2 \rangle)^2 + 4\langle xy \rangle^2)} \\ u &= 1 + \frac{d}{s} \\ v &= 2 - u\end{aligned}$$

the Hillas parameters calculated from:

$$\begin{aligned}
 \text{Size} &= \Sigma n_i \\
 \text{Length} &= \sqrt{\frac{\sigma_x^2 + \sigma_y^2 + s}{2}} \\
 \text{Width} &= \sqrt{\frac{\sigma_x^2 + \sigma_y^2 - s}{2}} \\
 \text{Miss} &= \sqrt{\frac{1}{3}(u\langle x \rangle^2 + v\langle y \rangle^2) - \left(\frac{2\sigma_{xy}\langle x \rangle\langle y \rangle}{s}\right)} \\
 \text{Distance} &= \sqrt{\langle x \rangle^2 + \langle y \rangle^2} \\
 \text{Alpha} &= \sin^{-1}\left(\frac{\text{Miss}}{\text{Distance}}\right) \\
 \text{Azwidth} &= \sqrt{\frac{\langle x \rangle^2 \langle y \rangle^2 - 2\langle x \rangle \langle y \rangle \langle xy \rangle + \langle x^2 \rangle \langle y^2 \rangle}{(\text{Distance})^2}}
 \end{aligned}$$

where, as represented in Fig(B.1),

Size is the total integrated light content of the shower,

Length is the RMS light spread along the major axis of the image,

Width is the RMS light spread across the minor axis of the image,

Miss is the orthogonal distance of the the major axis of the ellipse form the centre of the field of view,

Distance is the distance of the centroid of the image to the centre of the field of view,

Alpha is the angle between the major axis of the image and the line drawn between the centroid of the image and the centre of the field of view,

Azwidth is the RMS spread of light perpendicular to the line drawn between the centroid of the image and the centre of the field of view.

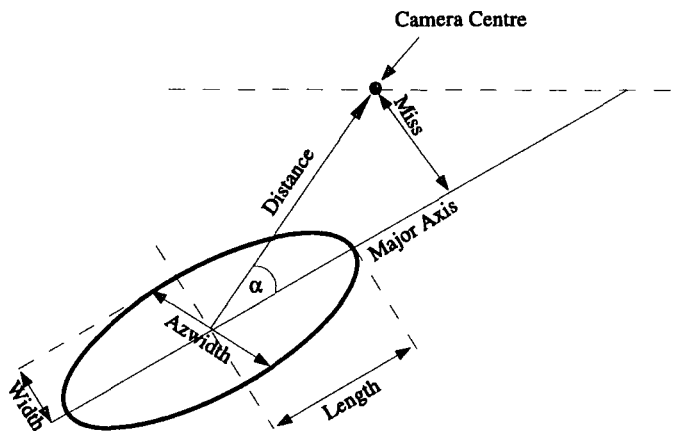


Figure B.1: Graphical representaion of Hillas parameter definitions

Bibliography

- [1] Aharonian, F., et al. 2004a *Astropart. Phys.*, 22, 109-125
- [2] Aharonian, F., et al. 2005 *A&A*, 430, 865-875
- [3] Aharonian, F., et al., submitted to *A&A*
- [4] Aharonian, F., et al. 2005 *Science*, Vol 307, Issue 5717, 1938-1942
- [5] Aharonian, F., et al. 2005 *Science*, Vol 309, Issue 5735, 746-749
- [6] Aye, K.-M., et al. 2003 *The 28th International Cosmic Ray Conference*, Vol. 5, 2975
- [7] Aye, K.-M., et al. 2003 *The 28th International Cosmic Ray Conference*, Vol. 5, 2879
- [8] Bailyn, C., et al. 2003 *ATEL#171*
- [9] Baixeras, C. 2003 *Nucl.Phys.B (Proc.Suppl.)* 114 247-252
- [10] Beilicke, M., et al. 2004 *New Astronomy Reviews*, 48, 407-410
- [11] Belloni, T. 2005 *astro-ph*, 0507556
- [12] Belloni, T. 2005 *A&A*, 440 207
- [13] Belloni, T., et al. 2000 *A&A*, 355 271
- [14] Benbow, W., for the H.E.S.S. Collaboration. 2004 2nd Int. Symp. on High Energy Gamma Ray Astronomy, Heidelberg, APS Conf. Proc. 745, 611
- [15] Bernlöhner, K., et al. 2003 *Astropart. Phys.*, 20, 111-128
- [16] Blumenthal, George R., Gould, Robert J. 1970 *Reviews of Modern Physics*, Volume 42 Number 2, 237-270
- [17] Bosch-Ramon, V., Paredes, J.M. *A&A* 417 1075-1081

- [18] Buxton, M., et al. 2003 ATEL #170
- [19] Casares, J. et al. 2005 MNRAS, 364, 899
- [20] Castro-Tirado, A.J., et al. 1994 ApJS., 92, 469-472
- [21] Cawley, M.F. et al. 1985 ApJ.,296, 185-189
- [22] Chadwick, P.M., et al. 2005 To appear in the contributions of 29th International Cosmic Ray Conference, Pune
- [23] Chadwick, P.M. et al. 1985 Nature, 318, 642
- [24] Charles, P.A. et al. 1999 IAUC 7267
- [25] Chaty, S., et al. 2001 A&A, 366, 1035
- [26] Cornils, R. et al. 2003 Astropart. Phys., 20, 129-143
- [27] Davies, J and Cotton, E. 1957 Journal of Solar Energy, 1, 16
- [28] Dermer, C.D. 1986 A&A, 157, 223-229
- [29] Fegan, D.J. 1997 J. Phys. G: Nucl. Part. Phys., 23, 1013-1060
- [30] Feldman, G.J., Cousins, R.D. 1998 Phys. Rev., D57, 3873
- [31] Fender, R.P., Belloni, T.M., Gallo, E. 2004 Mon. Not. R. Astron. Soc., 355, 1105-1118
- [32] Fender, R.P., et al. 1999 MNRAS, 304, 865
- [33] Fender, R., Belloni, T. 2004 Annu.Rev.Astron.Astrophys.,42, 317
- [34] Frank, I., Tamm,I. 1937 Dokl, Akad, Nauk. 14 109
- [35] Fuchs, Y., et al. 2003 A&A, 409 L35-L39
- [36] Funk, S., et al. 2004 Astropart. Phys., 22, 285
- [37] Galbraith, W., Jelley, J.V. 1953 Nature, 171, 349
- [38] Gallo, E., et al. 2004 MNRAS, 347, L52
- [39] Ghisellini, G., Maraschi, L. 1989 ApJ., 340, 181-189

- [40] Ghisellini, G., Maraschi, L., Treves, A. 1985 *A&A*, 146, 204-212
- [41] Ghisellini, G., et al. 1998 *MNRAS*, 301, 451
- [42] Giacconi, R., et al. 1962 *Phys. Rev. Lett.*, 9, 439
- [43] Ginzburg, V.L., Syrovatskii, S.I. 1965 *Ann. Rev. Astron. Astrophys.*, 3, 297-350
- [44] Goranski, V.P., 1978 *Astronomicheskij Tsirkulyar*, 1024, 3
- [45] Goranski, V.P., 1990 *Informational Bulletin on Variable Stars*, 3464
- [46] Greiner, J., Cuby, J.G., McCaughrean, M.J. 2001 *Nature*, 414, 522
- [47] Greiner, J., et al. 2001 *A&A*, 373, L37-L40
- [48] Hannikainen, D.C., et al. 1998 *A&A*, 337, 460-464
- [49] Hannikainen, D.C., et al. 2004 *A&A*, 423, L17-L20
- [50] Hannikainen, D.C., et al. 2003 *A&A*, 411, L451
- [51] Hartman, R.C., et al. 1992 *ApJ.*, 385, L1-L4
- [52] Heinz, S., Sunyaev, R.A. 2003 *MNRAS*, 343, L59-L64
- [53] Hofmann, W., for the H.E.S.S. Collaboration
- [54] Hjellming, R.M., et al. 2000 *ApJ.*, 544, 977-992
- [55] Hjellming, R.M. 2000 *ATEL #61*
- [56] Hillas, A.M. 1985 *Proc. 19th ICRC, La Jolla*, 3, 445-448
- [57] Homan, J. 2004 *ATEL 318*
- [58] Homan, J., et al. 2005 *ApJ.*, 624, 295
- [59] Hynes, R.I., et al. 2003 *ApJ.*, 583, L95
- [60] Hynes, R.I., et al. 2004 *ApJ.*, 609, 317
- [61] In 't Zand, J.J.M., et al. 1999 *IAUC 7119*

- [62] In 't Zand, J.J.M., et al. 2000 *A&A*, 357, 520-526
- [63] Kembhavi, A.K., Narlikar, J.V. 1999 *Quasars and Active Galactic Nuclei - An Introduction*, Cambridge University Press
- [64] Kitchin, C.R., 1987 *Stars, Nebulae and the Interstellar Medium* IOP Publishing Ltd.
- [65] Klein-Wolt, M., et al. 2002 *MNRAS*, 331, 745
- [66] Kubo, H. et al., 2004 *New Astronomy Reviews*, 48, 323-329
- [67] Latham, I.J., et al. 2005 *AIP Conf. Proc.: High Energy Gamma-Ray Astronomy*, 745, 323L
- [68] Luyten, W.J. 1927 *Harvard Bulletin*, No.852, 1
- [69] Liu, Q.Z., van Paradijs, J., van den Heuvel, E.P.J. 2000 *A&ASS*, 147, 25-49
- [70] Liu, Q.Z., van Paradijs, J., van den Heuvel, E.P.J. 2001 *A&A*, 368, 1021-1054
- [71] Longair, M.S., 1992 *High Energy Astrophysics*, Vol. 1, Cambridge University Press
- [72] McClintock, J.E., Remillard, R.A. 2005 *Compact Stellar X-ray Sources* Cambridge University Press, in press
- [73] McSwain, M.V. et al. 2001 *ApJ.*, 558, L43-L46
- [74] McSwain, M.V., Gies, D.R. 2002 *ApJ.*, 568, L27-L30
- [75] Mahadevan, R., Narayan, R., Krolik, J. 1997 *ApJ.*, 486, 286
- [76] Makishima, K., et al. 2000 *ApJ.*, 535, 632-643
- [77] Makishima, K., et al. 1986 *ApJ.*, 308, 635
- [78] Maraschi, L., Ghisellini, G., Celotti, A. 1992 *ApJ.*, 397, L5-L9
- [79] Markert, T.H., et al. 1973 *ApJ.*, 184, L67
- [80] Markwardt, C.B. et al. 1999 *IAUC* 7257
- [81] Mirabel, I.F., Rodríguez, L.F. 1994 *Nature*, 371, 46-48
- [82] Mirabel, I.F., Rodríguez, L.F. 1998 *Nature*, 392, 673-676

- [83] Mirabel, I.F., Rodríguez, L.F. 1999 *Ann. Rev. Astron. Astrophys.*, 37, 409-443
- [84] Monard, B., Pearce, A. 1999 IAUC 7256
- [85] Morselli, A. <http://people.roma2.infn.it/~aldo/> (viewed on 23/9/05)
- [86] Morrison, P. 1958 *Nuovo Cimento*, 7, 858
- [87] McCollough, M.L. et al. 1999 IAUC 7257
- [88] de Naurois, M. et al. 2003 The 28th International Cosmic Ray Conference, Vol. 5 2907
- [89] Pacholczyk, A.G. 1970 *Radio Astrophysics*, Freeman, San Francisco
- [90] Paredes, J.M., Marti, J. 2003 *Contributions to Science* 2, 303-314
- [91] Paredes, J.M. 2005 *AIP Conference Proceedings*, 745, 93-104
- [92] Paredes, J.M. et al. 2000, *Science*, 288, 2340-2342
- [93] Paredes, J.M. et al. 2002, *A&A*, 393, L99-L102
- [94] Rees M.J. 1966 *Nature*, 486-470
- [95] Revnivtsev, M., et al. 2002 *A&A*, 391, 1013-1022
- [96] Reynolds, Stephen P. 1982 *ApJ.*, 256, 13-27
- [97] Rowell, G., Krawczynski, H., Hofmann, W., Panter, M. 2000 H.E.S.S. Internal note
- [98] Rupen, M.P., et al. 2003 ATEL #172
- [99] Rupen, M.P., et al. 2003 ATEL #175
- [100] Samus, N.N., et al. 1999 IAUC 7277
- [101] Schwanke, U., Lohse, T. Internal H.E.S.S. paper
- [102] Smith, D.A., et al. 1999 IAUC 7253
- [103] Swank, J. 2004 ATEL 295
- [104] Stubbings, R., et al. 1999 IAUC 7253

- [105] Ti-pei Li, Yu-quan Ma, 1983 ApJ., 272, 317-324
- [106] Vincent P., for the H.E.S.S. Collaboration 2005 To appear in the contributions of 29th International Cosmic Ray Conference, Pune
- [107] Vladimírsky, B.M., Stepanian, A.A., Fomin, V.P. 1973 Proc. 13th International Cosmic Ray Conference, Denver, 1, 456
- [108] Weekes, T.C., Cawley, M.F.,paredes Fegan, D.J. et al. 1989 ApJ., 342, 379
- [109] Weekes, T.C. 2003 *Very High Energy Gamma-Ray Astronomy* IOP Publishing Ltd.
- [110] Weekes, T. C. et al. 2002 Astropart. Phys., 17, 221
- [111] Whitney, A.R. et al. 1971 Science, 173, 225
- [112] Zdziarski, A.A., et al. 2004 MNRAS, 351, 791-807
- [113] Zhong-Hui Fan, Xinwu Cao 2004 ApJ, 602, 103-110

